Global CH$_4$ Fluxes Derived from JAXA/GOSAT Lower Tropospheric Partial Column Data and the CTE-CH$_4$ Atmospheric Inverse Model

Aki Tsuruta[1], Akihiko Kuze[2,a], Kei Shiomi[2], Fumie Kataoka[3], Nobuhiro Kikuchi[2], Tuula Aalto[1], Leif Backman[1], Ella Kivimäki[1], Maria K. Tenkanen[1], Kathryn McKain[4], Omaira E. García[5], Frank Hase[6], Rigel Kivi[1], Isamu Morino[7], Hirofumi Ohyama[7], David F. Pollard[8], Mahesh K. Sha[9], Kimberly Strong[10], Ralf Sussmann[11], Yao Te[12], Voltaire A. Velazco[13], Mihalis Vrekoussis[14,15], Thorsten Warneke[15], Minqiang Zhou[16], and Hiroshi Suto[2]

[1]Finnish Meteorological Institute, Helsinki, Finland
[2]Japan Aerospace Exploration Agency, Tsukuba-city, Ibaraki, Japan
[3]Remote Sensing Technology Center of Japan, Minato-ku, Tokyo, Japan
[4]National Oceanic and Atmospheric Administration, Global Monitoring Laboratory, Boulder, Colorado USA
[5]Izaña Atmospheric Research Center (IARC), State Meteorological Agency of Spain (AEMET), Santa Cruz de Tenerife, Spain
[6]Institute of Meteorology and Climate Research (IMK-ASF), Karlsruhe Institute of Technology (KIT), Karlsruhe, Germany
[7]Earth System Division, National Institute for Environmental Studies (NIES), Tsukuba, Ibaraki, Japan
[8]National Institute of Water & Atmospheric Research Ltd (NIWA), Lauder, New Zealand
[9]Royal Belgian Institute for Space Aeronomy (BIRA-IASB), Brussels, Belgium
[10]Department of Physics, University of Toronto, Toronto, ON, Canada
[11]Karlsruhe Institute of Technology (KIT), IMK-IFU, Garmisch-Partenkirchen, Germany
[12]Sorbonne Université, CNRS, MONARIS, UMR8233, F-75005 Paris, France
[13]Deutscher Wetterdienst (DWD), Meteorological Observatory Hohenpeissenberg, 82383 Hohenpeissenberg, Germany
[14]Climate and Atmosphere Research Center (CARE-C), The Cyprus Institute, Nicosia, Cyprus
[15]Institute of Environmental Physics, University of Bremen, Bremen, Germany
[16]Institute of Atmospheric Physics, Chinese Academy of Sciences, Beijing, China
[a]now at: GORadS, Inc. Setagaya-ku, Tokyo, Japan

Correspondence: Aki Tsuruta (aki.tsuruta@fmi.fi)

Abstract. Satellite-driven inversions provide valuable information about methane (CH$_4$) fluxes, but the assimilation of total column-averaged dry-air mole fractions of CH$_4$ (XCH$_4$) has been challenging. This study explores, for the first time, the potential of the new lower tropospheric partial column (pXCH$_4$_LT) GOSAT data, retrieved by the Japan Aerospace Exploration Agency (JAXA), to constrain global and regional CH$_4$ fluxes. Using the CarbonTracker Europe-CH$_4$ atmospheric inverse

5   model, we estimated CH$_4$ fluxes between 2016–2019 by assimilating the JAXA/GOSAT pXCH$_4$_LT and XCH$_4$ data and surface CH$_4$ observations independently of each other. The Northern Hemisphere CH$_4$ fluxes derived from the pXCH$_4$_LT data were similar to the estimates derived from the surface observations, but was underestimated by about 35 Tg CH$_4$ year^{-1} ($\sim$6% of the global total) using the XCH$_4$ data. For the Southern Hemisphere, the estimates from the both GOSAT inversions were about 15–30 Tg CH$_4$ year^{-1} higher than those derived from surface data. The evaluations against independent data from the

10 Atmospheric Tomography Mission aircraft campaign showed good agreement in the lower tropospheric CH$_4$ from the inver-

sions using the pXCH$_4$_LT and surface data. However, from these inversions, the modelled North-South gradients showed significant overestimation in the upper troposphere and stratosphere, possibly due to relatively uniform inter-hemispheric OH distributions that control CH$_4$ sinks. Overall, we found that the use of the JAXA/GOSAT pXCH$_4$_LT data shows considerable potential in constraining global and regional CH$_4$ fluxes, advancing our understanding of the CH$_4$ budget.

1 Introduction

Methane (CH$_4$) is the second most important greenhouse gas (GHG) after carbon dioxide (CO$_2$) with a radiative forcing of 0.565 W m^{-2} (for 2023; https://www.esrl.noaa.gov/gmd/aggi/aggi.html, last access: 15 April 2025). Global and regional CH$_4$ budgets have been estimated using various data sources and methods, with recent estimates of global total emissions at 575 (553–586) Tg CH$_4$ yr^{-1} over the past decade based on top-down estimates (Saunois et al., 2024). While top-down inverse models provide well-constrained global total emissions using atmospheric measurements of surface CH$_4$ and satellite total columns, regional estimates still vary significantly depending on model setups and assimilated data (Deng et al., 2024; Stavert et al., 2021).

One important factor controlling inverse model estimates is the type of data assimilated in the inverse models. Broad categories of assimilable data are 1) high-precision in-situ observations from ground-based stations, shipboard and aircraft, and 2) column-averaged dry-air mole fractions of GHGs retrieved from satellites and ground-based stations. Over the years, the column-averaged dry-air mole fractions of CH$_4$ (XCH$_4$) from various satellites, such as SCanning Imaging Absorption spectroMeter for Atmospheric CartograpHY (SCIAMACHY) on board ENVIronmental SATellite (ENVISAT) (Bovensmann et al., 1999), Thermal And Near infrared Sensor for carbon Observations–Fourier Transform Spectrometer (TANSO–FTS) on board the Greenhouse Gases Observing Satellite (GOSAT) (Kuze et al., 2009), TANSO-FTS-2 on board GOSAT-2 (Suto et al., 2021), TROPOspheric Monitoring Instrument (TROPOMI) on board the Sentinel 5 Precursor (Hu et al., 2018), have been available and used in estimation of global and regional CH$_4$ fluxes (e.g. Alexe et al., 2015; Baray et al., 2021; Chen et al., 2022; Houweling et al., 2014; Lu et al., 2021; Miller et al., 2013; Lunt et al., 2019; Pandey et al., 2016; Wang et al., 2022; Tsuruta et al., 2023; Qu et al., 2021).

Due to their spatial coverage, satellite retrievals have shown high potential in estimating GHG budgets for regions with sparse surface observations, such as the tropics (Alexe et al., 2015; Houweling et al., 2014; Qu et al., 2021), central Africa (Lunt et al., 2019; Pandey et al., 2021) and China (Chen et al., 2022; Lu et al., 2021; Wang et al., 2022). However, it has been challenging to accurately model and retrieve vertical profiles of CH$_4$ concentrations, resulting in discrepancies between XCH$_4$ estimates from transport models and satellite retrievals. For transport models, key factors influencing the estimation of XCH$_4$ include model resolution (both horizontal and vertical), estimates of tropopause height and the representation of atmospheric chemical reactions with oxidants. The latter is significant since CH$_4$ is mostly oxidized by OH (Zhao et al., 2020). For satellite retrievals, prior profiles, clouds and aerosols, surface albedo and retrieval methods contribute to the uncertainty of retrieved XCH$_4$ values (Lindqvist et al., 2024; Sha et al., 2021). These factors contribute to large-scale latitudinal and

seasonal discrepancies between the satellite retrievals and transport model estimates using prior or posterior emissions derived by inversion estimates assimilating surface data.

45   Without addressing this issue, it could lead to unrealistic emission estimates from the inversions using satellite data that are significantly different from the estimates using surface observations. Previously in Tsuruta et al. (2023), we showed that the inversion using TROPOMI data without large-scale corrections could lead to smaller CH_4 emission estimates over the high northern latitudes compared to the inversion estimates based on surface observations. Various approaches have been developed to manipulate the large-scale discrepancies, which include: adjusting large-scale discrepancies before performing

50   satellite-based inversions (Houweling et al., 2017; Wang et al., 2022; Zhang et al., 2021), using the so-called proxy method that optimizes the CO_2:CH_4 ratios based on GOSAT data that provide both XCO_2 and XCH_4 retrievals (Feng et al., 2017; Palmer et al., 2021; Pandey et al., 2016), or discarding high-latitude data, where the problem appears most severe (Alexe et al., 2015; Baray et al., 2021; Lu et al., 2022). Apart from the proxy method, these adjustments have been somewhat arbitrary, with the degree of adjustments varying between studies. With appropriate manipulations, results from inversions using surface and

55   satellite data seem to agree in general, while satellite data can also provide additional regional information about magnitude and seasonality of CH_4 emissions (e.g. Wang et al., 2022; Lu et al., 2021; Pandey et al., 2021; Lunt et al., 2019; Feng et al., 2017).

The TANSO-FTS has measured reflected sunlight with two orthogonal components of polarization in the short wave infrared (SWIR) and emissions in the thermal infrared (TIR) simultaneously at the local time of 13:00. SWIR data constrain the total

60   column density and TIR data provide vertical profile information. Recently, the Japan Aerospace Exploration Agency (JAXA) has developed a new retrieval product of the partial column CO_2 and CH_4 densities of the lower troposphere (LT, typically 0–4 km), upper troposphere (UT, typically 4–12 km) and stratosphere from the SWIR and TIR by minimizing contamination by highly-polarized radiation scattered by aerosols and thin clouds (Kikuchi et al., 2016; Kuze et al., 2022). Compared to total column retrievals, this method offers the advantage that lower and upper tropospheric products contain more information

65   about surface fluxes, making them particularly useful for detecting local CH_4 (Kuze et al., 2020) and CO_2 (Kuze et al., 2022) fluxes. Atmospheric transport models generally perform well representing the in lower troposphere and combined with inverse models, they can reproduce atmospheric CH_4 surface observations reasonably well. Therefore, the use of tropospheric partial column data may provide better constrains for global and regional CH_4 flux estimates than using total column data.

In this study, we present for the fist time a way to assimilate JAXA/GOSAT lower tropospheric partial column CH_4

70   (pXCH$_4$_LT) data into the atmospheric inverse model CarbonTracker Europe-CH_4 (CTE-CH_4; Tsuruta et al., 2017). We examined the global CH_4 fluxes for 2016–2019 derived from the pXCH$_4$_LT data and compare those to the flux estimates derived from JAXA/GOSAT XCH$_4$ data and surface CH_4 observations. We evaluated annual budgets, seasonal cycles and spatial distributions of the total and subcategory emissions (anthropogenic and wetlands). Additionally, we compared optimized atmospheric CH_4 to independent (i.e. not assimilated) data from the Atmospheric Tomography Mission (ATom) aircraft cam-

75   paign and total and lower tropospheric partial column data from Total Carbon Column Observing Network (TCCON). The study highlights the potential of JAXA/GOSAT pXCH$_4$_LT data to improve the constraints on global and regional CH_4 fluxes compared to total column data.

2 Method

2.1 CTE-CH$_4$

CarbonTracker Europe-CH$_4$ (CTE-CH$_4$; Tsuruta et al., 2017) is a modular atmospheric inverse modelling system (van der Laan-Luijkx et al., 2017) based on the ensemble Kalman filter (EnKF) (Peters et al., 2005). It minimizes the cost function J,

$$J = (\mathbf{x} - \mathbf{x^b})\mathbf{P^{-1}}(\mathbf{x} - \mathbf{x^b}) + (\mathbf{y} - \mathcal{H}(\mathbf{x}))\mathbf{R^{-1}}(\mathbf{y} - \mathcal{H}(\mathbf{x})), \tag{1}$$

where $\mathbf{x}$ is the state vector, $\mathbf{x^b}$ is the prior state vector, $\mathbf{P}$ is the state covariance matrix, $\mathbf{y}$ is the observation of atmospheric concentrations (see Section 2.3), $\mathcal{H}$ is the observation operator, and $\mathbf{R}$ is the observation covariance matrix. In this study, the state vector $\mathbf{x}$ included the flux multiplication factors for anthropogenic and wetland fluxes (see Section 2.2). Fluxes were optimized at $1° \times 1°$ (latitude $\times$ longitude) resolution for land areas in northern Eurasia, $2° \times 3°$ grid for other land areas, and region-wise over the ocean (Fig. A1). Note that we do not optimize natural ocean fluxes, but do optimize anthropogenic emissions over the oceans, such as shipping and flight tracks that were included in the prior fluxes (EDGAR v8.0, Section 2.2). The prior covariance P was a block diagonal matrix, assuming that $1° \times 1°$ optimization regions were uncorrelated with $2° \times 3°$ optimization regions, land and ocean regions were uncorrelated and wetland fluxes were uncorrelated with anthropogenic fluxes. The prior uncertainty (diagonal values) were defined as ratio to prior fluxes (Section 2.2): 80% over land and 20% over the ocean. Off-diagonals were defined based on distances between the grids and regions with spatial correlation lengths of 100 km for $1° \times 1°$ optimization regions, 300 km over $2° \times 3°$ optimization regions and 900 km over the ocean. Localization schemes as in Peters et al. (2007) were applied. Regarding the EnKF setups, we used an ensemble size of 500 members and optimization window of 7-days with lag of 5 following Tsuruta et al. (2017).

For the observation operator $\mathcal{H}$, the atmospheric transport model TM5 (Krol et al., 2005) was used. TM5 was run at $1° \times 1°$ over Europe and $6° \times 4°$ globally, following e.g. Thompson et al. (2021) and Tenkanen et al. (2025). The resolution is coarser than the flux optimization resolution outside Europe. We acknowledge that using different resolutions can be questionable because the atmospheric states may not be resolved in detail enough. However, this could be justified as the study mostly focus on large-scale fluxes. TM5 was constrained by 3-hourly European Centre for Medium-Range Weather Forecasts (ECMWF) ERA5 meteorology (Hersbach et al., 2020). Atmospheric chemistry included OH, Cl and O(^{1}D). The OH concentrations were same as in Houweling et al. (2014), which is based on Spivakovsky et al. (2000) distribution but scaled globally by 0.92. For reactions with Cl and O(^{1}D), the reaction rates pre-calculated from the ECHAM/MESSy1 model (Jöckel et al., 2006) were used. The initial CH$_4$ concentration fields were taken from Tenkanen et al. (2025).

2.2 Prior fluxes

For anthropogenic emissions, prior estimates were taken from the Emissions Database for Global Atmospheric Research (EDGAR) v8.0 (Crippa et al., 2023). For fluxes from wetlands and dry mineral soils (hereafter wetlands), the estimates from the LPX-Bern v1.4 process based ecosystem model (Lienert and Joos, 2018) were used with 2019 values replicated from 2018. Other sources include biomass burning, microbial (termites) and ocean emissions, and the estimates from Global Fire Emis-
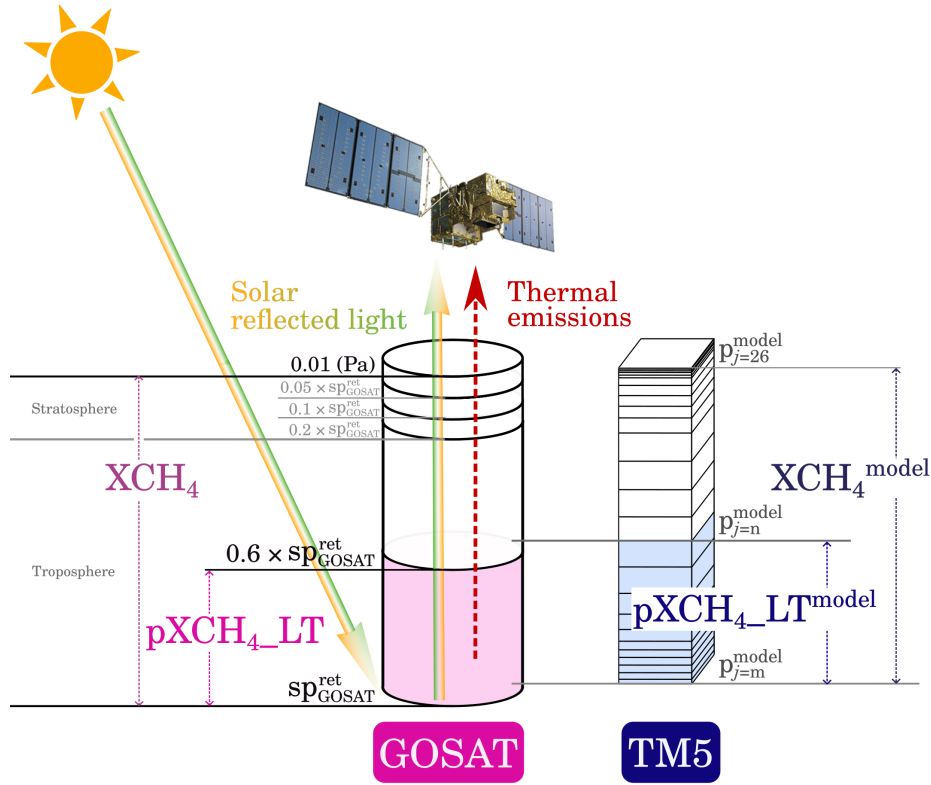
Figure 1. A schematic figure illustrating how total column (XCH_4) and lower tropospheric partial column ($pXCH_4\_LT$) are calculated in the JAXA/GOSAT data and from TM5. JAXA/GOSAT retrieval algorithm uses information from both solar reflected light and thermal emissions to retrieve partial column CH_4 mole fractions. In JAXA/GOSAT there are five layers between the retrieved pressure (sp_{GOSAT}^{ret}) and 0.01 Pa, with two tropospheric and three stratospheric layers. The lower troposphere (LT) is defined as pressure levels between sp_{GOSAT}^{ret} and $0.6 \times sp_{GOSAT}^{ret}$. In TM5, there are 25 model layers and XCH_4^{model} is calculated using all layers, i.e. the pressure levels between $p_{j=0}^{model}$ and $p_{j=26}^{model}$. For calculation of $pXCH_4\_LT^{model}$, the minimum level (m) and maximum level (n) vary depending on sp_{GOSAT}^{ret}. $m = 0$ if $sp_{GOSAT}^{ret} > p_{j=0}^{model}$ and otherwise the maximum level at which p_j^{model} exceeds sp_{GOSAT}^{ret}. n is the level at which p_j^{model} reaches $0.6 \times sp_{GOSAT}^{ret}$.

110 sions Database (GFED) v4.1s (van der Werf et al., 2017), the Vegetation Integrative SImulator for Trace gases (VISIT; Ito and Inatomi, 2012) and Saunois et al. (2020) were used, respectively. Among those, the fluxes from anthropogenic, wetlands and biomass burning were monthly and inter-annually varying. The emissions from termites were annual estimates, and ocean fluxes were climatological.

2.3 Atmospheric observations

 #### 2.3.1 JAXA/GOSAT partial column data

The JAXA/GOSAT retrieval algorithm is based on the Full Physics algorithm and is extended to use both the 2-orthogonal SWIR and TIR signals simultaneously (Kikuchi et al., 2017). JAXA's forward calculation constructs the vector radiance and uses the 2-orthogonal polarized SWIR observation in four windows with bi-directional reflection. For TIR, the scalar radiance is handled in the forward model for three windows. The empirical orthogonal function (EOF) fitting is taken account in the retrieval process, where XCO_2, XCH_4 and XH_2O are simultaneously retrieved with solar-induced chlorophyll fluorescence (SIF) information. CO_2 and CH_4 partial column-averaged concentrations are derived for two layers in the troposphere and three layers in the stratosphere. The H_2O concentrations are derived on 11 vertical layers.

The five CO_2 and CH_4 layers are defined by the pressure levels based on the retrieved surface pressure, denoted as sp_{GOSAT}^{ret} (see also Fig. 1). The two tropospheric layers, lower troposphere (LT) and upper troposphere, are defined as the pressure levels between sp_{GOSAT}^{ret} and $0.6 \times sp_{GOSAT}^{ret}$, and between $0.6 \times sp_{GOSAT}^{ret}$ and $0.2 \times sp_{GOSAT}^{ret}$, respectively. The three stratospheric layers are defined as the pressure levels between $0.2 \times sp_{GOSAT}^{ret}$ and $0.1 \times sp_{GOSAT}^{ret}$, between $0.1 \times sp_{GOSAT}^{ret}$ and $0.05 \times sp_{GOSAT}^{ret}$, and between $0.05 \times sp_{GOSAT}^{ret}$ and $0.01 \, Pa$, respectively. In this study, all the GOSAT data is based on JAXA/GOSAT product v2.0 (https://www.eorc.jaxa.jp/GOSAT/Global_GHGs_Map/index.html, last access: 4 June 2024).

During the study period, the TANSO-FTS and the Cloud and Aerosol Imager (CAI) were shut down and the observation had been suspended during 17–24 May 2018 due to the Command and Data Management System (CDMS) incident, and from 24 November 2018 until 28 December 2018 due to the rotation anomaly of the second solar-paddle.

For comparison to model estimates, the XCH_4 values from model results were calculated as:

$$XCH_4{}^{model} = \frac{\sum_i (CH_{4_i} \times dp_i)}{\sum_i dp_i}, \quad i = 1, ..., 25 \tag{2}$$

where CH_{4_i} is the dry air mixing ratio of CH_4 at TM5 model layer i, temporally and horizontally interpolated to time and location of the JAXA/GOSAT data, and dp_i is the pressure thickness at the layer i.

For calculating modelled lower tropospheric partial columns of methane, $pXCH_4\_LT^{model}$, the layers were selected based on sp_{GOSAT}^{ret} (see also Fig. 1). The minimum layer is $i = 0$ if the surface pressure in TM5 model is smaller than sp_{GOSAT}^{ret} and otherwise the maximum layer at which TM5 model pressure exceeds the GOSAT-retrieved surface pressure. The maximum layer corresponded to the point where TM5 pressure reached $0.6 \times sp_{GOSAT}^{ret}$. Vertical interpolation was not applied for simplicity, and therefore, modelled mixing ratio was calculated using thinner (in case $sp_{GOSAT}^{ret} > sp^{model}$) or thicker (in case $sp_{GOSAT}^{ret} < sp^{model}$) air mass from the lowest layer. For the uppermost layer, due to the selection method, the model nearly always contained thicker air mass than the retrievals. These likely lead to potential biases (see also Section 4.1).

Averaging kernels were not applied to XCH_4^{model} and $pXCH_4\_LT^{model}$, as they were unavailable for the v2.0 product. However, we are aware of a newer version, v3.0 data, where averaging kernels are now available. We did not apply any preprocessing of the JAXA/GOSAT data, such as averaging or removing large-scale differences that may have been raised in comparison to inversion estimates assimilating surface data. This way, we could examine the effect of observations directly. In the assimila-

tion, we assumed observational uncertainty (retrieval error + transport model error) to be 1) 30 ppb globally with a rejection threshold of 60 ppb for both of the XCH$_4$ or pXCH$_4$_LT assimilations, and 2) 50 ppb with a rejection threshold of 100 ppb in the case that assimilated only pXCH$_4$_LT data over land (see also 2.4). The rejection thresholds discriminates the observations if differences between observed and prior-modelled mole fractions exceed the threshold, i.e. the observations are rejected and would not be used to constrain the fluxes. These values are somewhat arbitrary, but they follow other inversion experiments that use the GOSAT data (e.g. Janardanan et al., 2020; Lu et al., 2021; Maasakkers et al., 2021; McNorton et al., 2018). The larger uncertainty is justified as retrieval errors in the lower tropospheric partial column data are probably higher compared to the total column data.

2.3.2 Surface CH$_4$ mole fractions

Surface CH$_4$ mole fraction observations mainly from ObsPack v4.0 (Schuldt et al., 2021) were assimilated in the inversion, as well as used for evaluation (see Fig. A1 for site locations and Table A1 for details). The data include ICOS ATC CH$_4$ Release and ICOS ATC NRT CH$_4$ growing time series data, which were downloaded among with other NOAA ObsPack data and the ICOS Carbon portal (Table A2). The data consisted of discrete and continuous observations from in-situ stations and ships. Similar to our previous studies (Tsuruta et al., 2017, 2019; Tenkanen et al., 2025), all data were filtered by taking observations at well-mixed conditions based on quality flags given by the data providers. Continuous data were processed into daily means by averaging observations during local time afternoon (12–16) or night (0–4). Observational uncertainties (observational error + transport model error) ranged between 4.5–75 ppb, depending on each site (Table A1).

In addition, we used aircraft measurements from the Atmospheric Tomography Mission (ATom; Thompson et al., 2022), obtained from the ObsPack v6.0 (Schuldt et al., 2023) for independent evaluation. During 2016–2019, there were ATom observations from four campaigns: 2016 July–August, 2017 January–February, September–October and 2018 April–May. Prior and posterior mole fractions were estimated at each sampling location and time, linearly interpolated within the TM5 model grid cells. ATom data were not assimilated in the inversions and therefore can be used as independent observations for validation.

2.3.3 TCCON

The Total Carbon Column Observing Network (TCCON) is a global network providing XCH$_4$ measurements retrieved from the spectrum of near-infrared radiation of direct sunlight using ground-based Fourier Transform Spectrometers (FTS) (Wunch et al., 2011). We used the GGG2020 data (Laughner et al., 2023, 2024) from 25 sites globally (Table A3) for evaluation of inversion results. The sites were selected as those that provided GGG2020 data, and have at least one year of measurements between 2016–2019. The data were not assimilated in the inversions and so can also be used as independent observations for validation.

For comparison, hourly average mixing ratio interpolated horizontally to the TCCON locations were used. Temporal colocations were done by selecting the TCCON observations that were closest to the model time step (hourly) and set the time limit of half an hour; if there was a TCCON observation made within $\pm$ half an hour of the model time step, the TCCON and modelled values were taken into account.

For comparison to total column (XCH$_4$), the model estimates were calculated by applying TCCON averaging kernels (Rodgers and Connor, 2003):

$$\hat{c} = c_a + (\mathbf{h} \circ \mathbf{a})^{\mathbf{T}}(\mathbf{x} - \mathbf{x_a}) \tag{3}$$

where $\hat{c}$ is the averaging kernel corrected XCH$_4$ value from the model, c_a is the TCCON prior XCH$_4$, $\mathbf{h}$ is the TCCON pressure weighting function, $\mathbf{a}$ is the TCCON averaging kernel, $\mathbf{x}$ is the model profile and $\mathbf{x_a}$ is the TCCON prior profile. After applying the averaging kernel, daily means were calculated for evaluation.

In addition, the tropospheric partial column were calculated from TCCON total columns of CH$_4$ and hydrogen fluoride (HF). Practically all of the HF exists in the stratosphere, where HF is produced from photodissociation of chlorofluorocarbons (CFCs). The concentrations of long lived tracers, such as CH$_4$ and HF, are strongly correlated in the stratosphere (e.g. Plumb, 2007). Airmasses containing both CH$_4$ and CFCs enter through the topical stratosphere, where CH$_4$ is oxidized and HF is produced. In the stratosphere, CH$_4$ shows a nearly linear inverse relationship with HF. By assuming a linear relationship in the stratosphere (Washenfelder et al., 2003; Saad et al., 2014) the tropospheric partial column of XCH$_4{}_{\text{TCCON}}^{\text{tropo}}$ is given as

$$\text{XCH}_4{}_{\text{TCCON}}^{\text{tropo}} = \text{XCH}_4 - \beta \times \text{XHF} \tag{4}$$

where β is the stratospheric CH$_4$:HF slope. As the tracer to tracer correlations typically exhibit distinct correlations in the tropics, extratropics and polar stratospheric vortices (Plumb, 2007), we derived slopes for the tropics (30° S–30° N), SH (90° S–30° S), NH (30° N–90° N), as well as for the polar stratospheric vortices. Profile data of CH$_4$ and HF from the Atmospheric Chemistry Experiment - Fourier Transform Spectrometer (ACE-FTS) version 4.1 data products (Boone et al., 2020) were used to calculate the slopes. The polar vortices were identified from potential vorticity data from the ERA5 reanalysis (Hersbach et al., 2020). The vortex edge was assumed to be represented by the $|36|$ PVU isoline. The interference of water can increase the error in the column averaged HF (XHF) (Saad et al., 2014), especially at high airmasses. Therefore, observations with column averaged H$_2$O (xH$_2$O) above 2000 ppm and zenith angle larger than $90 - 0.0075 \times$ xH$_2$O degrees were discarded.

For comparison to the tropospheric partial column, Eq. 2 was applied similarly to calculate pXCH$_4$_LT$^{\text{model}}$, but for the lowest and uppermost layer, vertical interpolation was applied to TCCON retrieval surface pressure sp$_{\text{TCCON}}^{\text{ret}}$ and tropopause height, respectively. The pressure at dynamic tropopause was calculated based on ERA5 reanalysis data, defined by the $|2|$ PVU isoline. Constant extrapolation was applied in case sp$_{\text{TCCON}}^{\text{ret}}$ >sp$^{\text{model}}$.

2.4 Simulation setups

In this study, we present the results from four inversions that differed in the observations assimilated:

      InvSURF: surface CH$_4$ data only

      InvGLT: JAXA/GOSAT partial column data (pXCH$_4$_LT) only

      InvGLT_land: JAXA/GOSAT partial column data (pXCH$_4$_LT) over land only

      InvGTOT: JAXA/GOSAT total column data (XCH$_4$) only

In all of the GOSAT inversions, only the JAXA/GOSAT data were assimilated to examine the effect of the data in constraining fluxes independent of other datasets. The inversion without ocean data were tested in consideration of assimilating other satellite
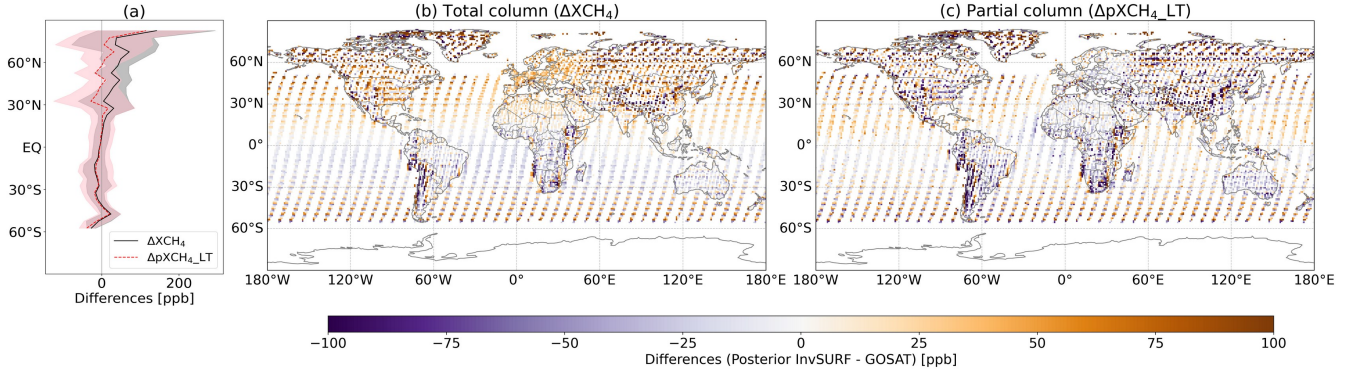
Figure 2. Mean differences between posterior InvSURF and JAXA/GOSAT retrievals, averaged over 2016–2019. (a) five degree latitudinal means (solid line) with standard deviation (shaded area), and (b) and (c) $1° \times 1°$ grid means. Positive values indicate posterior InvSURF mole fractions being higher than the JAXA/GOSAT retrievals.

data, such as TROPOMI, which do not necessary provide ocean data from all retrieval products. Additionally, considering relatively small contribution of ocean fluxes to global total, compared to that of e.g. CO_2, we examine if land fluxes would be
215 constrained equally well without ocean data.

For InvGLT and InvGTOT, observational uncertainty and rejection threshold was set to be 30 and 60 ppb, respectively, and for InvGLT_land they were set as 50 and 100 ppb, respectively. All inversions were run for 2015–2019, but 2015 was considered as a spin-up, and not included in the analysis. The analysis on regional fluxes was done based on $30°$ latitudinal bands. Throughout the following sections, the prior and posterior mole fractions refer to those derived using prior and posterior
220 fluxes, respectively.

3 Results

3.1 Comparison of CH$_4$ mole fractions from InvSURF and JAXA/GOSAT

In this section, we analyse the differences between posterior estimates from the surface-based inversion (InvSURF) and JAXA/GOSAT retrievals for total and partial columns, i.e.

$$\Delta XCH_4 = XCH_{4\,InvSURF}^{post} - XCH_{4\,GOSAT}^{ret}$$
225 $$\Delta pXCH_4\_LT = pXCH_4\_LT_{InvSURF}^{post} - pXCH_4\_LT_{GOSAT}^{ret} \qquad (5)$$

In the comparison of total column, latitudinal biases were found with positive ΔXCH_4 values in the extratropics and negative values in the tropics, especially in the SH tropics (Fig. 2 (b)). This feature was systematic in time, such that similar biases were found regardless of years and seasons, although the absolute value of the biases varied. In the comparison of lower tropospheric partial columns, such latitudinal biases were less prominent (Fig. 2 (c)), especially over land, indicating better agreement over
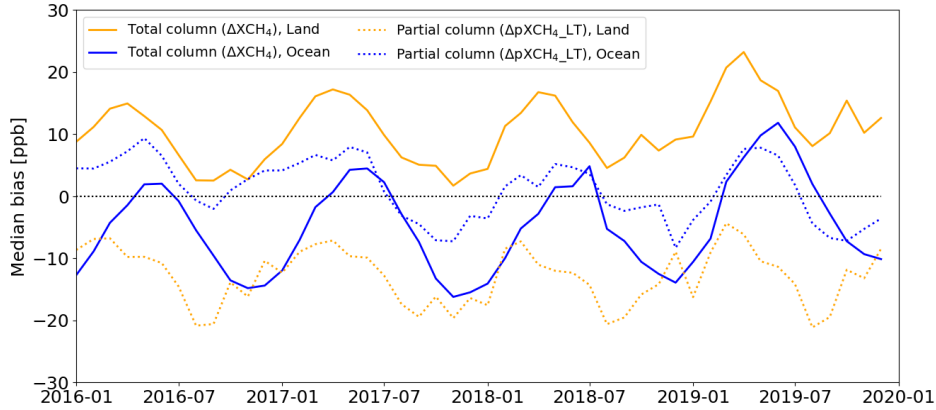
Figure 3. Global monthly median differences between posterior InvSURF and JAXA/GOSAT retrievals. Positive values indicate posterior InvSURF mole fractions being higher than the JAXA/GOSAT retrievals.

230   NH extratropics (Fig. 2 (a)). This indicates the potential role of upper atmosphere in the total column biases, where posterior estimates and retrievals had difficulty agreeing.

Large biases were observed in regions such as Greenland, western South America, southernmost South Africa, eastern China and northern Russia in both comparisons (Fig. 2 (b) and (c)). Because of the challenges in retrieving data over ice-covered land, we assume that biases in Greenland were mostly associated with retrieval errors. Biases in other regions could be

235   due to unresolved fluxes by surface observations, i.e. the inversion error in estimating fluxes, retrieval errors due to cloud cover and difficulties in retrieving surface pressure in regions with highly elevated surface. The horizontal resolutions of the transport model also contribute to the biases in highly elevated areas. The additional simulation with TM5 showed that increasing resolution from $4° \times 6°$ (latitude $\times$ longitude) to $2° \times 3°$ decreased biases in mountain regions in Africa and Tibetan plateau, although the biases in regions such as Andes mountains in South America and edges of Tibetan plateau still remain (Fig. A2).

240   We also acknowledge that the vertical interpolation and averaging kernel (AK) contribute to the biases in highly elevated areas, especially for XCH_4 (Fig. A3) (see also Section 4.1).

Europe showed the smallest $\Delta pXCH_4\_LT$, which is encouraging considering that InvSURF probably had constrained the emission in Europe the best compared to other regions globally, and modelled tropospheric CH_4 from InvSURF is well in line with ground-based observations (Section 3.2). Both the transport model and optimization resolutions were the smallest

245   and number of observations were relatively large in Europe (Section 2.1). There was a notable shift between better agreement in Europe and a worse agreement in Russia and Africa, attributed to the CTE-CH_4 setup: TM5 was run with highest spatial resolution over Europe and an extended area (Tsuruta et al., 2015), with a coarser resolution elsewhere. This resulted to creating an artifact of a border between the zoom grid and the global grid that caused the shift. An additional simulation with TM5 with global $2° \times 3°$ (latitude $\times$ longitude) resolution and without zoom, eliminated these boundaries (Fig. A2).

250   Both lower tropospheric partial and total column comparisons showed seasonal and land-sea biases (Fig. 3). The global average of ΔXCH_4 and $\Delta pXCH_4\_LT$ were smaller during NH autumn-winter than spring-summer. The amplitude of the seasonal biases was larger in the total column, especially over the oceans. The comparison of the land and sea biases showed that the biases in the total column were larger over land than ocean, whereas an opposite behaviour was observed for the lower tropospheric partial columns. In other words, the ΔXCH_4 and $\Delta pXCH_4\_LT$ were closer over the ocean than land on average,

255   with absolute median monthly differences of 5 ppb over the ocean and 23 ppb over land, indicating the possible influence of land fluxes to upper atmosphere. Overall, the average bias during 2016–2019 was smallest in $\Delta pXCH_4\_LT$ over the ocean.

3.2   Evaluation against surface and aircraft data

Comparison of posterior atmospheric CH_4 to the surface ground-based observations showed the smallest overall bias, root mean squared error (RMSE) and strongest correlation for InvSURF (Table 1) as expected, since these observations were

260   assimilated in the inversion. Among the GOSAT inversions, those using the lower tropospheric partial column data (InvGLT and InvGLT_land) showed the best agreement to the surface ground-based observations, while the total column inversion (InvGTOT) showed large negative biases following the prior (Table 1). RMSE and correlation of the GOSAT inversions were not significantly different. The latitudinal gradient was best captured by InvSURF, InvGLT and InvGLT_land compared to the surface stations (Fig. 4a). The inversions mostly underestimated the surface observations with the underestimation being the

265   smallest in the Southern Hemisphere (SH) for InvGLT and InvGLT_land and in the Northern Hemisphere (NH) for InvSURF. InvGTOT showed better agreement than InvSURF in the SH, but considerable underestimation in the NH (Fig. 4a), which was the reason for strong negative bias in the overall agreement (Table 1).

In the mid- and high northern latitudes (above 30° N) the seasonal cycle amplitude (SCA) was generally overestimated by model estimates in prior, which was worsened by inversion (SCA of posterior estimates were larger than prior) (Fig. A4). In

270   addition, seasonal minima in the NH occurred one to two months later than observations, although the results in InvSURF were slightly better than in the prior and GOSAT inversions (Fig. A4). This indicates either possible errors in seasonal cycles of posterior emission, or atmospheric chemical sinks.

Comparison to ATom aircraft data also showed that on average, InvSURF, InvGLT and InvGLT_land resulted in the best statistics (Table 1), and the latitudinal gradient agreed better with the observations compared to InvGTOT at the altitude

275   bands 0–2000 and 2000–4000 meters above sea level (masl) (Fig. 4b, A5 and A6). In these altitude zones, the mean bias was significantly larger in InvGTOT, which was in line with the results compared to surface ground-based stations (Table 1). This height corresponds approximately to the height where most of the surface ground-based stations were situated and from which JAXA/GOSAT XCH_4_LT data were calculated. Between 4000–8000 masl, the latitudinal gradients from InvGTOT were better captured whereas the other inversions overestimated these gradients (Fig. A6). Considering that the tropopause height

280   is around 9000 masl or above, these results indicate that the transport model has problems in representing upper tropospheric concentrations. This is consistent with the finding that all model estimates worsened at high altitudes (> 8000 masl). All model estimates, both prior and posterior, failed to capture low mole fractions observed in high latitude (> 50° N/S) regions (Fig. A5). Such low CH_4 mole fractions were observed especially in the winter of 2017 and the spring of 2018 when the tropopause
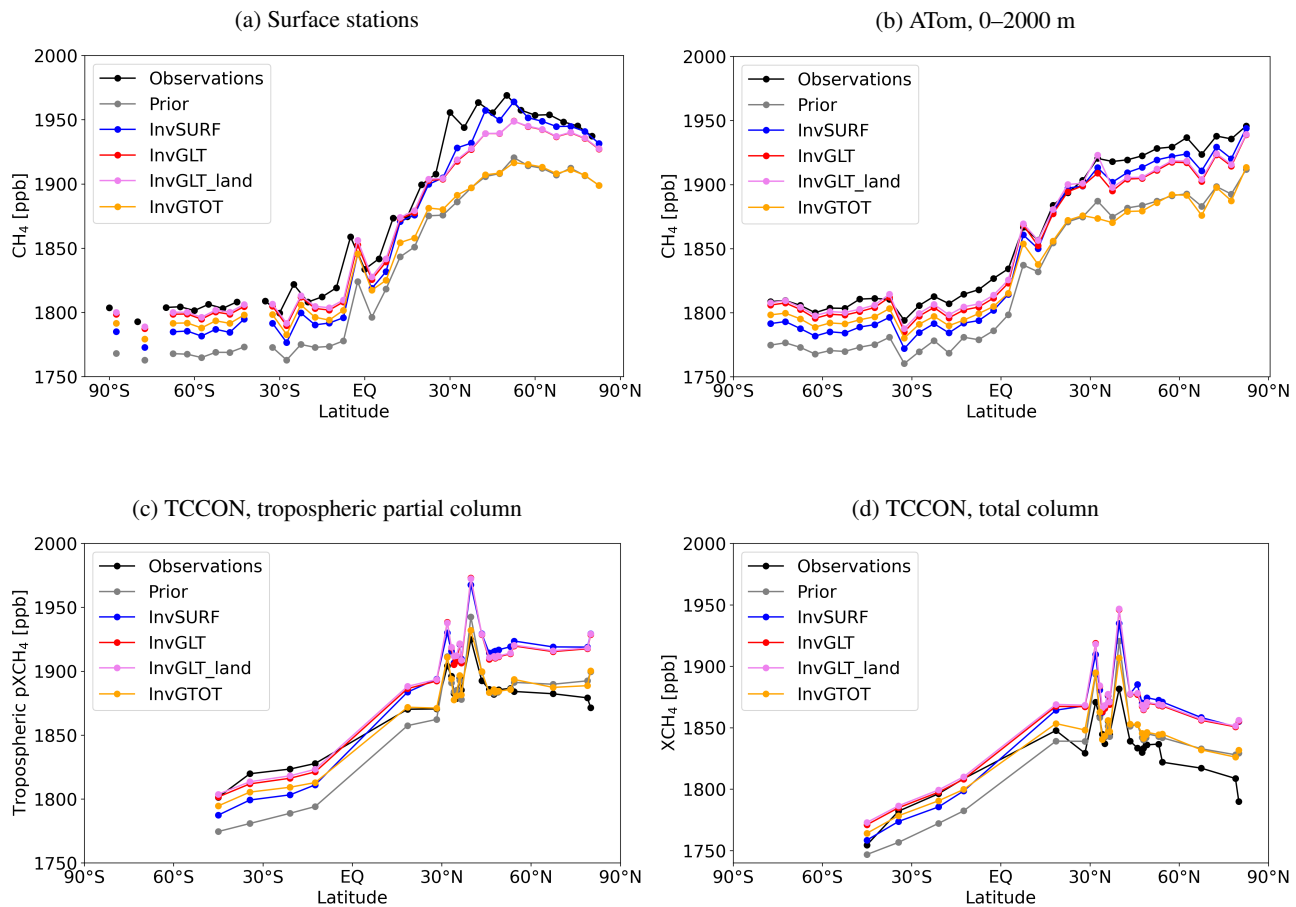
Figure 4. Mean atmospheric CH$_4$, averaged over 2016–2019 at (a) surface ground-based and shipboard stations, (b) ATom observation locations, and (c) and (d) TCCON sites. For (a), the data that were assimilated in InvSURF were used. For (a) and (b), mean over five-degree latitude bands are shown. For (c) and (d), no spatial averaging is applied. The coloured lines are the posterior estimates from each inversion, which is estimated by running TM5 forward using posterior fluxes of the corresponding inversion simulation.

height was lower and the ATom aircraft operated in the stratosphere (Fig. A7). This is when the disagreement was strongest,
285 possibly indicating the improper modelling of vertical profiles in polar vortex conditions.

Table 1. Bias, root mean squared error (RSME) and Pearson's correlation against observations at surface ground-based stations assimilated in InvSURF, ATom aircraft measurements, and TCCON data. The statistics were calculated for each ground-based and TCCON station over 2016–2019 and four ATom campaigns separately, and the mean of all stations or campaigns are shown. The value followed by ± sign is the standard deviation (std) of statistics from all stations. For ATom, the minima and maxima of the statistics are shown in square brackets instead of std due to the limited number of campaigns (four) to calculate std from. Biases were calculated as modelled values subtracted by observed values, and therefore, positive values indicate model overestimation. The simulation with the best statistics are highlighted in bold.

Observations/Inversions	Bias [ppb]	RMSE [ppb]	Correlation
Surface ground-based			
Prior	-42.2 ± 15.6	20.3 ± 11.1	0.69 ± 0.15
InvSURF	**-9.2 ± 10.7**	**18.1 ± 10.5**	**0.80 ± 0.12**
InvGLT	-12.3 ± 13.6	20.8 ± 13.2	0.74 ± 0.15
InvGLT_land	-11.7 ± 13.8	20.6 ± 13.1	0.74 ± 0.15
InvGTOT	-36.9 ± 18.8	20.0 ± 12.1	0.74 ± 0.16
ATom, < 2000 m			
Prior	-35.2 [-40.6, -31.1]	16.0 [11.0, 22.2]	0.97 [0.93, 0.98]
InvSURF	-13.4 [-20.8, -8.7]	**15.8** [12.2, 18.0]	**0.97 [0.95, 0.98]**
InvGLT	-11.1 [-19.0, -5.1]	18.3 [14.3, 25.9]	0.95 [0.91, 0.97]
InvGLT_land	**-8.5** [-15.9, -4.0]	19.9 [15.4, 26.3]	0.94 [0.90, 0.97]
InvGTOT	-28.6 [-37.4, -21.9]	22.0 [15.9, 34.9]	0.94 [0.87, 0.98]
ATom, all			
Prior	-22.8 [-34.3, -15.6]	**34.6** [17.3, 48.9]	0.77 [0.63, 0.92]
InvSURF	3.3 [-11.2, 8.1]	35.2 [18.1, 49.9]	0.77 [0.63, 0.92]
InvGLT	**1.2** [-8.3, 13.6]	34.7 [17.5, 48.1]	0.76 [0.64, 0.92]
InvGLT_land	3.5 [-5.4, 16.0]	**34.6** [18.8, 47.7]	0.76 [0.65, 0.90]
InvGTOT	-13.8 [-26.0, -0.7]	34.9 [19.2, 45.8]	**0.76 [0.66, 0.92]**
TCCON, partial column			
Prior	-3.3 ± 16	15.4 ± 4.0	0.38 ± 0.20
InvSURF	23.4 ± 20.3	**13.6 ± 4.2**	**0.68 ± 0.15**
InvGLT	24.2 ± 15.8	15.8 ± 5.5	0.56 ± 0.21
InvGLT_land	25.4 ± 15.4	15.7 ± 5.4	0.56 ± 0.20
InvGTOT	**0.7 ± 9.0**	14.7 ± 4.5	0.59 ± 0.19
TCCON, total column			
Prior	**3.2 ± 15.3**	12.4 ± 7.9	0.39 ± 0.23
InvSURF	23.8 ± 20.4	**10.1 ± 6.4**	**0.59 ± 0.28**
InvGLT	25.2 ± 18.4	11.9 ± 8.8	0.50 ± 0.28
InvGLT_land	26.3 ± 18.3	11.8 ± 8.7	0.50 ± 0.27
InvGTOT	8.1 ± 10.8	11.2 ± 7.4	0.52 ± 0.28

3.3 Evaluation against TCCON

The latitudinal gradient was generally weaker in TCCON tropospheric partial and total columns (Fig. 4) compared to the surface observations, indicating a smaller influence of surface fluxes. Therefore, the evaluation against the TCCON data provides limited information about how well the inversions constrained the surface fluxes but focuses more on the model performance regarding long-range transport, tropopause mixing and atmospheric chemistry, which are important to take into account when assimilating total column satellite data. In the northern high latitudes, the extracted TCCON partial columns successfully separated the stratospheric component, showing no significant low biases under polar vortex conditions (Fig. A8).

Compared to the surface data comparison, the TCCON comparison showed better overall agreement and improved representation of the latitudinal gradient in InvGTOT compared to other inversions for both total and tropospheric partial columns (Table 1, Fig. 4c and 4d). In the NH, all model estimates exhibited overestimation, driven by larger latitudinal gradients, with InvSURF, InvGLT and InvGLT_land performing worse than InvGTOT. Considering also that InvGTOT showed the best agreement with the comparison to Atom data between 4000–8000 masl on latitudinal gradients, this indicates the importance of the upper troposphere in the estimation of XCH_4. This finding also denotes that model biases in the estimation of XCH_4 are not solely caused by errors in resolving stratospheric concentrations, but also the errors in upper troposphere contribute to total column biases.

3.4 CH_4 fluxes
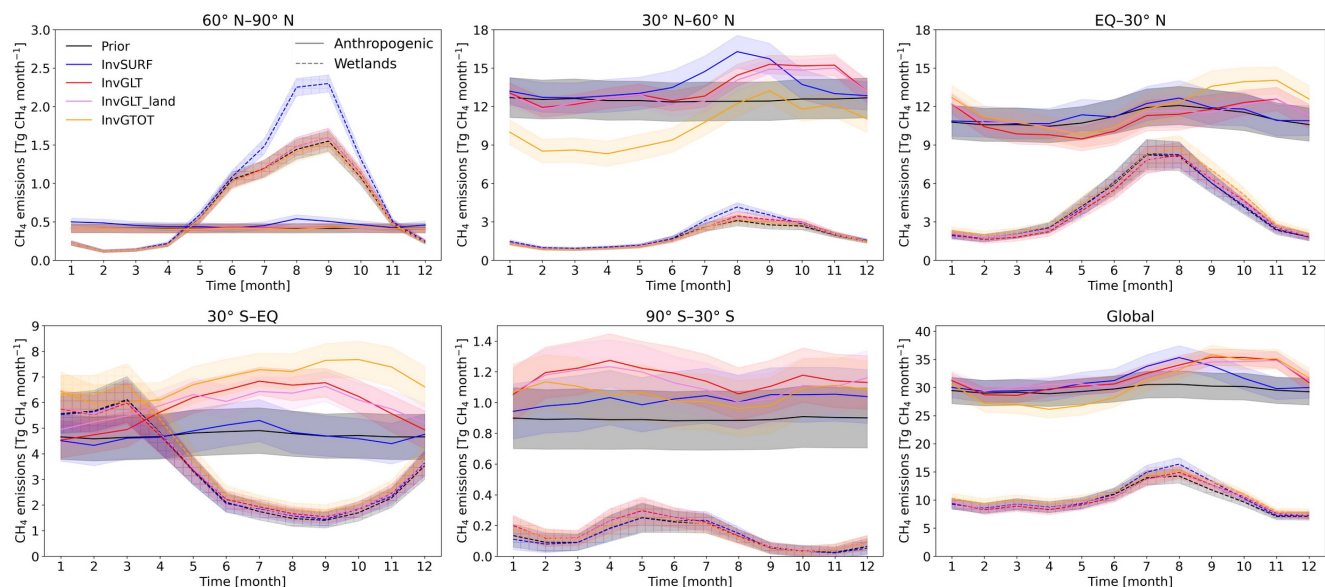
Figure 5. Monthly mean anthropogenic and wetland CH_4 emissions at 30° latitudinal bands and global totals. The means are taken from 2016–2019. Shaded areas illustrate uncertainty as standard deviations of 500 ensemble members.

Table 2. Global and regional CH_4 emissions (Tg CH_4 yr^{-1}), averaged over 2016–2019. Uncertainty presented in numbers after $\pm$ sign is the standard deviation of 500 ensemble members in CTE-CH_4.

Category / Region	Prior	InvSURF	InvGLT	InvGLT_land	InvGTOT
Total					
Global	523 ± 30	547 ± 26	550 ± 20	552 ± 21	544 ± 23
60° N–90° N	17 ± 1	20 ± 1	18 ± 1	17 ± 1	17 ± 1
30° N–60° N	179 ± 19	196 ± 14	191 ± 10	189 ± 10	154 ± 12
EQ–30° N	197 ± 18	200 ± 17	195 ± 13	199 ± 14	211 ± 15
30° S–EQ	115 ± 13	115 ± 12	129 ± 10	130 ± 10	146 ± 11
90° S–30° S	14 ± 2	15 ± 2	17 ± 2	17 ± 2	16 ± 2
Anthropogenic					
Global	356 ± 28	373 ± 67	382 ± 17	383 ± 18	368 ± 20
60° N–90° N	5 ± 1	6 ± 1	5 ± 1	5 ± 1	5 ± 1
30° N–60° N	150 ± 18	164 ± 14	161 ± 10	159 ± 10	125 ± 12
EQ–30° N	133 ± 16	136 ± 15	132 ± 11	135 ± 12	143 ± 13
30° S–EQ	57 ± 11	57 ± 10	70 ± 8	70 ± 8	82 ± 9
90° S–30° S	11 ± 2	12 ± 2	14 ± 2	14 ± 2	13 ± 2
Wetlands					
Global	120 ± 12	126 ± 11	121 ± 10	122 ± 10	130 ± 11
60° N–90° N	8 ± 1	10 ± 1	8 ± 1	8 ± 1	8 ± 1
30° N–60° N	21 ± 3	24 ± 2	22 ± 2	22 ± 2	22 ± 2
EQ–30° N	49 ± 7	49 ± 7	48 ± 6	49 ± 6	53 ± 7
30° S–EQ	40 ± 6	40 ± 6	41 ± 6	41 ± 6	45 ± 6
90° S–30° S	1 ± 1	1 ± 1	2 ± 1	2 ± 1	2 ± 1
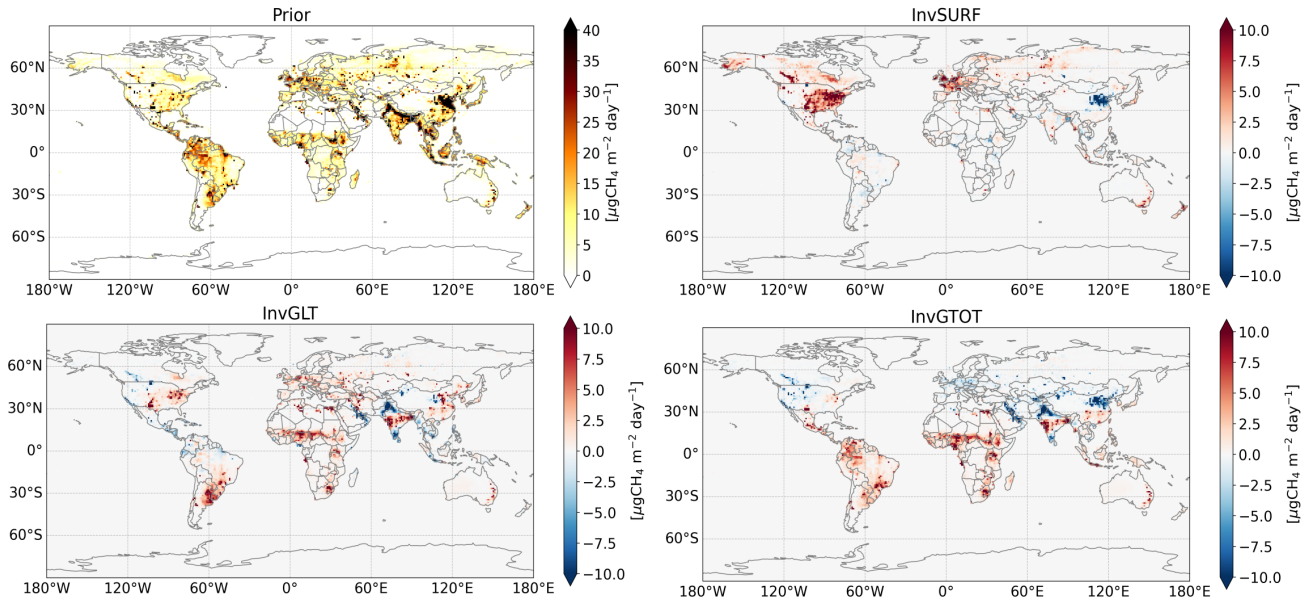
Figure 6. Prior total CH_4 emissions (left top) and emission increments (posterior - prior), averaged over 2016–2019. Positive values indicate posterior emissions being higher than the prior.

The 2016–2019 average global total and regional (30° latitudinal band) emissions are presented in Table 2. The posterior global total emissions were similar in all inversions (544–552 $\pm$ 20–26 Tg CH_4 yr^{-1}) and showed increases from the prior with reduction in uncertainty (523 $\pm$ 30 Tg CH_4 yr^{-1}). Most of the increase from the prior was attributed to anthropogenic emissions (c.a. 57–96%). The sectorial emissions showed that anthropogenic emissions were higher and wetland emissions lower in InvGLT and InvGLT_land compared to InvSURF and InvGTOT. The anthropogenic emissions in the SH in InvGLT and InvGLT_land were higher compared to InvSURF but comparable in magnitude to InvSURF in the NH. InvGTOT also showed higher anthropogenic emissions in the SH compared to InvSURF, especially in the tropics (30° S–EQ), but lower anthropogenic emissions in 30° N–60° N.

Between the tropics and SH (90° S–30° N), the posterior anthropogenic emissions in the GOSAT inversions deviated more from the prior compared to InvSURF (Table 2, Fig. 5). This difference was primarily associated with emissions over South America, Africa and India (Fig. 6). The monthly variations of anthropogenic emissions deviated largely from the prior in the GOSAT inversions (Fig. 5). All GOSAT inversion showed an emission peak in November in the region from the equator to 30° N, which was three months later than prior and InvSURF. In 30° S–EQ, all GOSAT inversions showed a clear seasonal cycle with emissions peaking during April–November. In contrast, the prior had no clear seasonal cycle, and InvSURF showed a small seasonal cycle with a peak in July. In 90° S–30° S, InvGLT and InvGLT_land showed two emission peaks, one around April and another in October. InvGTOT did not show the April peak, but it aligned with InvGLT and InvGLT_land in presenting an emission reduction in August and peak in October. InvSURF showed a less distinct seasonal cycle with emissions constantly

increasing from the prior in all months, except January. In the tropics, there are only a few surface stations (Fig. A1), which are often far from emission sources, measuring background mixing air. As a result, the JAXA/GOSAT data likely contained more valuable information to constrain the fluxes in these regions compared to the sparse surface data.

In 30° N–60° N, posterior anthropogenic emissions in InvGTOT were about 35 Tg CH_4 year^{-1} lower than those in the other inversions (Table 2), representing about 6% of the global total. These differences were not associated specifically with a specific region, but InvGTOT showed mostly negative emission increments indicating that posterior emissions were lower than the prior in this region (Fig. 6). Unlike the tropics, there are relatively large number of surface stations in Europe and the best optimization setup in terms of model spatial resolution, and thus, we suspect that the results from InvGTOT in Europe may have been too low. The comparison to ground-based observations in Europe also showed strong underestimation in InvGTOT (-44 ppb on average compared to stations within [12° W–37° E, 34° N–73° N] domain). For other regions, considering that the regions such as USA and China are large CH_4 emitters (Petrescu et al., 2024), we also suspect that the results in InvGTOT were underestimated, possibly due to the ability of the transport model representation of XCH_4 (see also Section 4.2).

In 60° N–90° N, posterior wetland emissions in the GOSAT inversions stayed close to the prior compared to InvSURF (Table 2). While InvSURF showed an increase in summer wetland emissions, such change was not found in the GOSAT inversions Therefore, the seasonal cycle amplitude of wetland emissions was smaller in the GOSAT inversions (Fig. 5). It is known that the GOSAT data has sampling limitation during winter due to polar nights and very low solar zenith angles. However, JAXA/-GOSAT data were available above 60° N during summer (Fig. 2). Further, as we found from the comparison of JAXA/GOSAT retrievals to InvSURF (see Section 3.1), posterior mole fractions in InvSURF were higher than the JAXA/GOSAT retrievals, indicating that emissions from the GOSAT inversions would likely be lower than those from InvSURF. Therefore, we argue that the lower emissions from the GOSAT inversions were not due to limited number of data, but rather reflected the agreement between the inversion and the prior. However, the inversion setups, such as the observation and transport model biases and uncertainties, rejection threshold and prior emission uncertainty, may need to be investigate further to better constrain the fluxes using the satellite data.

3.5 Uncertainty estimates

Despite a rather arbitrary choice of prior observational uncertainty (diagonals of **R** in Eq. 1, see Section 2.1 and 2.3), the posterior emission uncertainties were generally lower in the GOSAT inversions compared to InvSURF, and lowest in InvGLT. These differences were most pronounced in the NH tropics (EQ–30° N) (Table 2). The differences between InvSURF and GOSAT inversions were probably driven by the number of available observations, since GOSAT had much more data in the tropics. This could also explain in part the latitudinal bias found in Section 3.1. Within the GOSAT inversions, the number of assimilated data were higher in InvGTOT than InvGLT (Fig. A9), even though the observational uncertainty and rejection thresholds were the same in both inversions. This indicates that the lower uncertainty in InvGLT was not simply due to number of assimilated observations but also related to sensitivity of the data to surface fluxes. Due to the nature of the retrieved quantity, total columns have less sensitivity to surface fluxes than ground-based data or lower tropospheric partial column data, i.e. the total column data would have less power to constraint on surface fluxes. Therefore, the larger number of assimilated
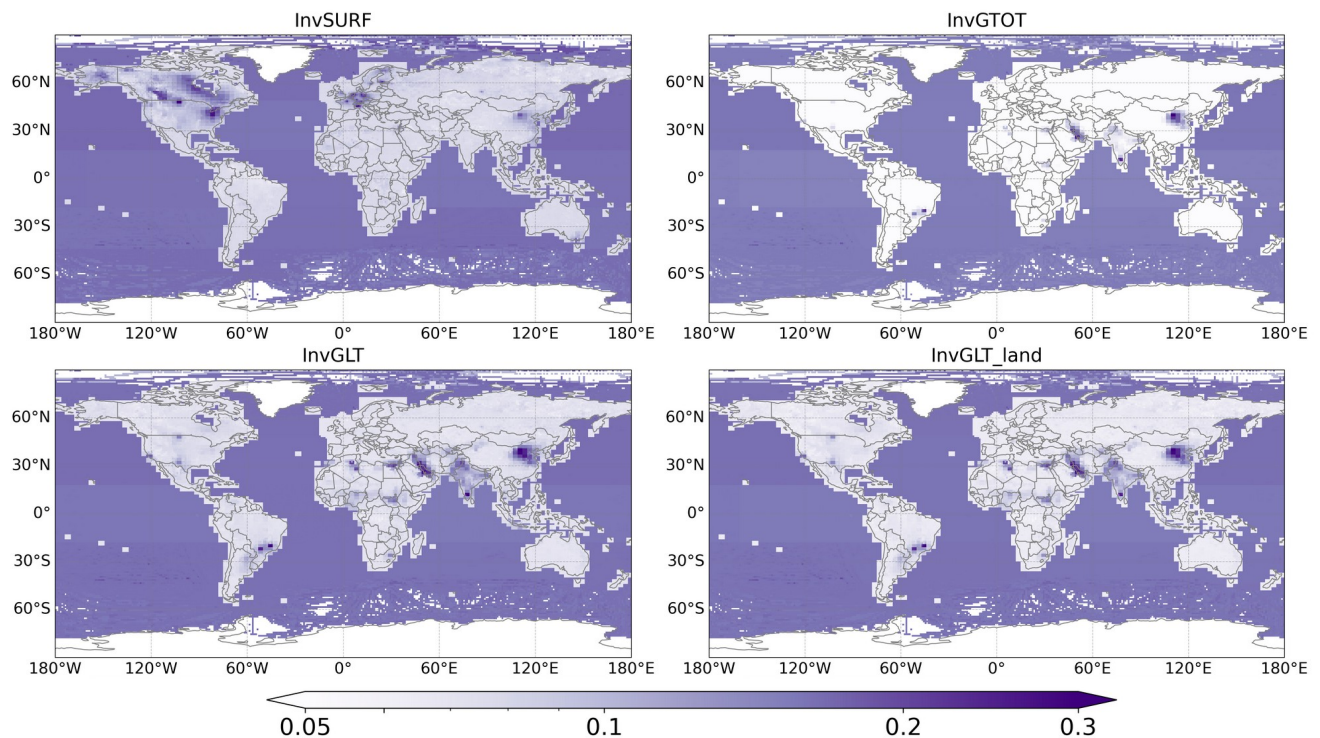
Figure 7. Annual mean uncertainty reduction rate $(\sigma_{\mathrm{prior}} - \sigma_{\mathrm{posterior}})/\sigma_{\mathrm{prior}}$ of total fluxes, averaged over 2016–2019. σ were calculated as standard deviation from 500 ensemble members. Note the colour is in logarithmic scale.

observations in InvGTOT did not necessary lead to higher uncertainty reduction rates than in InvGLT. However, it is possible that the prior observational uncertainty prescribed in InvGLT may have been underestimated, considering that retrieval errors

355 are probably higher for lower tropospheric partial columns compared to total columns. Consequently, the posterior uncertainty of the fluxes may have been also underestimated. On the other hand, the transport model error may be lower for the lower tropospheric partial column data, considering that the transport model performs better in representing tropospheric concentrations than stratospheric, so the total observational uncertainty could have been reasonable. The global total flux uncertainty of InvGLT_land was slightly higher compared to InvGLT. The posterior uncertainty was higher in the region with the largest

360 uncertainty (EQ–30° N). Since the flux horizontal and seasonal distributions in InvGLT_land did not change significantly from InvGLT overall, we could argue that the effect of ocean data as a constraint was minor.

The spatial distribution of uncertainty reduction rates is shown in Fig. 7. This figure indicates that the GOSAT inversions constrained fluxes mostly in tropical regions and northeast China, while InvSURF showed strongest reductions in the USA, Canada and Europe. InvSURF also showed a reduction hot-spot areas in northeast China, but the signal was much weaker

365 compared to the GOSAT inversions. The uncertainty reduction rates over land in InvGTOT was weak in general, with fewer reduction in hot-spots compared to InvGLT and InvGLT_land, indicating that the use of the lower tropospheric partial column

data was more effective in constraining fluxes compared to total column data. The inversions with lower tropospheric partial column data showed stronger uncertainty reduction rates in Africa and India, which were not as prominent in other inversions. The weaker uncertainty reduction rates from the GOSAT inversions in North America and Europe were probably due to 1) larger uncertainty in the observations, where many surface observations in these regions had less than 30 ppb observation uncertainty (Table A1), and 2) lack of observations in high latitudes over winter.

The uncertainty reduction rates over the ocean were relatively large compared to those over land (Fig. 7). This is mainly due to the assigned prior uncertainty, which was significantly smaller over the ocean; the emissions were low (Fig. 6) and prior uncertainty was set to 20% over the ocean (see Section 2.1). This has led to prior uncertainty of $\sim 10^{-22}$ mol m^{-2} s^{-1} over the ocean, which is approximately 10^{12} smaller than those over land. The uncertainty reduction rates are sensitive to small changes when the prior uncertainties are small, and therefore, they became larger over the ocean, although the absolute changes in the uncertainties were small.

4 Discussion

4.1 Effect of vertical interpolation and averaging kernels

In this study, we did not apply vertical interpolation for simplicity or averaging kernels (AK) as JAXA/GOSAT v2.0 did not provide the information. However, we acknowledge that these are important to take into account when possible. With test simulations with TM5, we found that the latitudinal biases improved in ΔXCH$_4$ when compared to JAXA/GOSAT v3.0 data when vertical interpolation and AK were applied (Fig. A3). In the NH temperate regions, the biases in ΔXCH$_4$ turned from positive to negative and became similar to the biases in the tropics. Therefore, using v3.0 would possibly increase the CH$_4$ flux estimates from the NH temperate regions in InvGTOT, aligning better with the inversions using surface and lower tropospheric partial column data. There are still positive biases in the high latitudes, although they are smaller than these compared to v2.0 data without interpolation and AK.

For lower tropospheric partial column, ΔpXCH$_4$_LT, the overall latitudinal biases did not change significantly by applying vertical interpolation and AK (Fig. A3). However, the large positive biases in highly elevated regions (e.g. Andean region in South America and Tibetan plateau in China and surroundings) and northeastern part of China, where CH$_4$ emissions are large, turned to large negative biases. Nevertheless, large biases, both in positive and negative, means that the observations are likely to be rejected during assimilation and would not affect flux estimates. The ΔpXCH$_4$_LT over the ocean showed less latitudinal biases – the negative biases in the SH tropics turned positive. Overall, the robustness of modelling lower tropospheric partial column could be considered as an advantage over total column, having potential to provide more robust estimates regardless of differences in how transport models represent long-range transport, tropopause mixing, and atmospheric chemistry.

4.2 Role of upper atmosphere and OH in the estimation of XCH$_4$ values

Latitudinal differences between posterior from the surface inversion and satellite total column retrievals have been seen in earlier studies using TM5 and other global Eulerian atmospheric chemistry transport models (Alexe et al., 2015; Qu et al., 2021; Tsuruta et al., 2017; Turner et al., 2015; Zhang et al., 2021). Such discrepancies were reported regardless of the satellites' retrieval products, prior fluxes, years or seasons. Part of the misrepresentation of CH$_4$ mole fractions in the upper troposphere could be due to convection schemes in the transport models (Saito et al., 2013), but the exact effect on the representation of total column values are to be examined. In high northern latitudes, the stratospheric profile is one of the challenges especially in polar vortex conditions (Tsuruta et al., 2023). However, polar vortex occurs only occasionally in spring, and our comparison to GOSAT, TROPOMI and TCCON XCH$_4$ values in this and previous studies showed biases even during the periods without polar vortex conditions (Tsuruta et al., 2017, 2023). As shown in this study, latitudinal biases occur already in the upper troposphere (Fig. A6), which confirms the findings from Lindqvist et al. (2024) who argued that the role of the stratosphere in the estimation of XCH$_4$ was minor.

In addition, we found that using higher horizontal resolution in TM5 improves agreement in the lower tropospheric partial and total columns (Fig. A2), indicating the importance of the transport model resolution. The latitudinal biases indeed seem to be slightly lower using higher spatial resolution (Stanevich et al., 2021), although exact effect is to be examined. This study was limited in its exploration of the impact of the horizontal resolution, but increasing model resolution in the vertical dimension could also improve the representation of upper atmospheric CH$_4$.

The discrepancies in the latitudinal gradient could also be caused by the choice of chemistry schemes in the transport models. The distribution of OH, the largest sink of CH$_4$ (Saunois et al., 2024), plays an important role in regulating ambient methane levels. The OH concentration fields by Spivakovsky et al. (2000) used in this study and several others (Patra et al., 2011; Saunois et al., 2024) have relatively uniform inter-hemispheric distributions, possibly underestimating the OH concentration in the NH and overestimating them in the SH (Zhao et al., 2019). This leads to higher atmospheric CH$_4$ in the NH and lower in the SH, as shown by this and previous studies (Tsuruta et al., 2017, 2023). Zhao et al. (2020) showed that the differences in the inter-hemispheric distribution of OH could lead to about 25–50 Tg CH$_4$ yr^{-1} differences in the inter-hemispheric distribution of CH$_4$ emissions, where Spivakovsky et al. (2000) based inversion lead to lower emissions in the NH and higher in the SH. This outcome is in line with the conclusion that the emission distributions in InvGTOT, which estimated the lowest CH$_4$ emissions in the NH, could be unreliable. The vertical OH profiles used in this study that have distinct peaks at around 500–600 hPa (Zhao et al., 2019) may also partially explain why ATom profiles and GOSAT total columns were not accurately reproduced.

4.3 Land-sea discrepancies

In CH$_4$ inversions using the GOSAT data, it has not been common to correct land-sea biases in the retrievals or exclude data over the ocean. CH$_4$ fluxes over the ocean are minor compared to those over land (Saunois et al., 2024). Consequently, the effect of land-seas biases in the JAXA/GOSAT retrieval data is expected to be small in estimation of CH$_4$ fluxes. This study showed that the emission estimates and posterior mole fractions from InvGLT and InvGLT_land were very similar, despite the

different systematic and seasonal biases over land and sea compared to InvSURF (Fig. 3), confirming that the effect of ocean data as constraints has minimum influence to the outcome of inversions. Therefore, to significantly decrease the amount of data in the inversions and increase the computational efficiency.

4.4 Global and regional emissions

The global total estimates from InvSURF were slightly lower than from the inversions using JAXA/GOSAT_LT data, and on the lower edge of the range of the top-down (TD) estimates from the latest Global Methane Budgets (553–586 Tg CH_4 yr^{-1}, 2010–2019 average; Saunois et al., 2024). The breakdown of anthropogenic and wetlands sources showed that anthropogenic emissions from this study were slightly higher compared to Saunois et al. (2024) (350–391 Tg CH_4 yr^{-1} vs 145–214 Tg CH_4 yr^{-1}, 2010–2019 TD averages). These differences occur probably because of smaller wetland prior emissions (120 Tg CH_4 yr^{-1}), which are on the lower boundary of bottom-up estimates from Saunois et al. (2024) (119–203 Tg CH_4 yr^{-1}, 2010–2019 bottom-up averages). This indicates that the prior uncertainty may need to be revised, and for example, spatially and seasonally varying uncertainty ratios Tenkanen et al. (2025) could provide better freedom in the inversion. It is worth pointing out that we did not use a separate prior for freshwater emissions, and, thus, the freshwater emissions could be wrongly attributed to anthropogenic emissions, if there is a spatial overlap with the anthropogenic emissions.

The total emissions in the eastern part of North America agree well with previous studies (Alexe et al., 2015; Baray et al., 2021; Lu et al., 2022). Higher emissions in the northeastern part of the US compared to EDGAR (Fig. 6) point to underestimation of emissions from oil and gas. It should be noted that although we used the newer version of EDGAR (v8.0) in this study, the underestimation still seems to remain. The seasonal variability of anthropogenic CH_4 emissions in southern North America (including the contiguous United States and Mexico) from the GOSAT inversions (Fig. A10a) showed opposite patterns compared to InvSURF. The seasonal cycle in this region is likely to be associated with natural gas consumption (Zeng et al., 2023) and agriculture (Maasakkers et al., 2023). In contrast to results from Maasakkers et al. (2023) who argue that the seasonal pattern of natural gas consumption has strong interannual variations and is spatially inhomogeneous, our results from the GOSAT inversions were similar to those from Miller et al. (2013) which showed larger emissions during autumn and winter compared to summer.

In China, InvSURF and InvGTOT showed strong negative emission increments (i.e. posterior emissions were lower then prior) around Beijing (Fig. 6), which is consistent with studies such as Lu et al. (2021) and Wang et al. (2022) who assimilated both surface and the GOSAT XCH_4 data. This seems to be a common feature found in other studies despite different GOSAT retrieval products, prior, transport and inverse models were used (Lu et al., 2021, and references therein). On the other hand, InvGLT and InvGLT_land showed positive emission increments in eastern and southern China. This is closer to the findings from Chen et al. (2022) who assimilated the TROPOMI XCH_4 data. However, these results again contradict with Qu et al. (2021) who assimilated both GOSAT and TROPOMI XCH_4 data and argued that an inversion using only TROPOMI XCH_4 may be unreliable over China because the TROPOMI XCH_4 is strongly affected by cloud cover.

In central Africa and South Sudan wetland regions, our GOSAT inversions showed a large increase in total emissions (Fig. 6), which were primarily associated with wetland emissions. This is in line with findings from Lunt et al. (2019), who used the

GOSAT XCH$_4$, and Pandey et al. (2021), who used the TROPOMI XCH$_4$ in their inversions, although our posterior estimates were considerably lower. For instance, we found monthly maxima below 1 Tg CH$_4$ month^{-1} around South Sudan, compared to Lunt et al. (2019) estimates of 7 Tg CH$_4$ month^{-1} and Pandey et al. (2021) estimates of seasonal cycle amplitude of about 2–3 Tg CH$_4$ month^{-1}. Nevertheless, the seasonal cycle in this region from the GOSAT inversions (Fig. A10b) showed significantly lower emissions in June–July and later maxima in August–September compared to prior and InvSURF. This corresponds slightly better to dry and wet seasons and is in line with Lunt et al. (2019) and Pandey et al. (2021), although we could not reproduce high emissions in late months.

The magnitude of high northern latitude (NHL) wetlands remained uncertain. Previous studies showed that in some cases, NHL emissions from the inversion based on the GOSAT data were lower compared to those based on surface data (Pandey et al., 2016; Feng et al., 2017), while others showed the opposite (Alexe et al., 2015; Baray et al., 2021). Our analysis showed that the wetland emissions for 60° N–90° N were lower in the GOSAT inversions regardless of the assimilated data type (total or lower tropospheric partial column) compared to InvSURF. This is in line with our previous studies assimilating TROPOMI XCH$_4$ data (Tsuruta et al., 2023), and using other wetland priors, such as JSBACH-HIMMELI, where emissions were relatively larger among process-based models (Aalto et al., 2024; Tenkanen et al., 2025). Tsuruta et al. (2023) assumed that the lower NHL wetland emissions in the TROPOMI inversions were due to latitudinal biases associated with model-retrieval differences (Lindqvist et al., 2024). However, as shown in this study, the inversion using lower tropospheric partial column data also resulted in lower NHL wetland emissions compared to InvSURF, indicating that there may be fundamental discrepancies between satellite and surface inversions. The differences were partly due to spatial coverages and temporal distributions of the observations and uncertainties associated with transport models, observations, prior emissions and possible biases in the satellite data, but further study is needed to find the exact cause of these discrepancies and to obtain more robust the emission estimates.

5 Conclusions

This study presented the advantages of JAXA/GOSAT lower tropospheric partial column retrievals in estimating global and regional CH$_4$ budgets using the CTE-CH$_4$ atmospheric inverse model. Our findings showed that assimilating the lower tropospheric partial column data led to posterior CH$_4$ fluxes and atmospheric CH$_4$ mole fractions that were more consistent with the inversion estimates using surface data compared to total column retrievals. In addition, partial column retrievals constrained CH$_4$ fluxes better than the total column retrievals globally and better than surface data in low latitudes with sparse observation network. This is a considerable advantage to the atmospheric inverse modelling community, and the partial column product could potentially be a better product than total column for estimation of CH$_4$ fluxes.

In addition, we found that lower tropospheric partial column data possibly reduce global emission uncertainty. Furthermore, it was concluded that the lower tropospheric partial column ocean data have minimal influence on constraining CH$_4$ fluxes over land, suggesting that excluding ocean data could improve computational efficiency. However, further studies are needed to assess uncertainty in the partial column retrievals and transport model's ability to represent partial column mole fractions.

Our results showed that the uncertainty reduction rates were low in North America and Europe in the GOSAT inversions, indicating the need to further investigate uncertainties in the JAXA/GOSAT data and the transport model, as well as the critical issue of lack of the satellite data in high latitudes during winter. This study also highlighted the importance of transport model resolution in estimation of total and partial column data, indicating the need for high resolution transport models in satellite-driven inversions.

Our study was limited to retrievals from one satellite (GOSAT) assimilated to a single inverse model (CTE-CH$_4$) for a relatively short period (four years). Future efforts should focus on exploiting the use of other satellite datasets and inverse models. JAXA/GOSAT provides partial column products since 2009 up to today, including those from GOSAT-2 since 2019, that will allow expanding the study period to perform trend analysis. In addition, in this study, averaging kernels were taken into account only in a test simulation with TM5 for a limited period and detailed retrieval uncertainty were not taken into account. These are available in the newest version of JAXA/GOSAT partial column product (v3.0), and including this information will possibly result in more realistic estimates of CH$_4$ fluxes and their uncertainties. Lastly, JAXA/GOSAT provides GOSAT partial column products for upper layers (upper tropospheric and three stratospheric layers). The use of these products in inversions can provide useful information in identifying the causes of transport model biases in vertical layers.

Code and data availability. All the model results, inputs and code will be provided on request from the corresponding author (Aki Tsuruta, aki.tsuruta@fmi.fi).

Author contributions. The research was conceptualized by HS with contributions from AT and TA. AT developed model codes for assimilation of lower tropospheric partial column data, and carried out all inverse modelling simulations and visualization. AT did analysis with contributions from AK, KSh, FK, TA, MKT, LF, EK and HS. AK, KSh, FK, NK and HS provided the GOSAT data. EK calculated modelled XCH$_4$ values at TCCON sites. LF calculated TCCON tropospheric partial columns. KM provided ATom data. TCCON data were provided by OEG (Izaña), FH (Karlsruhe), RK (Sodankylä), IM (Tsukuba), HO (Rikubetsu), DFP (Lauder), KSh (Saga), KSt (Eureka), RS (Garmisch), MKS (Reunion Island), YT (Paris), VAV (Burgos), MV (Nicosia), TW (Orleans) and MZ (Xianghe). AT wrote the original draft of the manuscript with contributions from AK, LB, EK, MKT and HS. All authors have read and approved to publish the version of the manuscript.

Competing interests. The contact author has declared that none of the authors has any competing interests.

Financial support. We thank the JAXA (24RT000409), EU-H2020 VERIFY (776810), CoCO$_2$ (958927) and EMME-CARE – Eastern Mediterranean and Middle East – Climate and Atmosphere Research Centre (856612), EU-Horizon EYE-CLIMA (101081395) and IM4CA (101183460), Finnish Center of Excellences (272041, 353082), Research Council of Finland projects FIRI - ICOS Finland (345531), GHG-SUPER (351311) and CHARM (364975), Research Council of Finland Flagships ACCC (337552) and FAME (359196), CSC (FICOCOSS)

and European Space Agency projects AMPAC-Net (AO/1-10901/21/I-D) and SMART-CH4 (AO/1-11844/23/I-NS) for financial support. Measurements at Jungfraujoch were supported by ICOS Switzerland (SNF grant 20F120_198227). The Paris site has received funding from Sorbonne Université, the French research center CNRS and the French space agency CNES. The Eureka TCCON measurements were made at the Polar Environment Atmospheric Research Laboratory (PEARL), primarily supported NSERC, ECCC, and CSA. The TCCON sites at Rikubetsu, Tsukuba, and Burgos are supported in part by the GOSAT series project. Local support for Burgos is provided by the Energy Development Corporation (EDC, Philippines). The Réunion Island station is operated by the Royal Belgian Institute for Space Aeronomy with financial support since 2014 by the EU project ICOS-Inwire (Grant agreement ID 313169), the ministerial decree for ICOS (FR/35/IC1 to FR/35/IC6), ESFRI-FED ICOS-BE (EF/211/ICOS-BE) project and local activities supported by LACy/UMR8105 and by OSU-R/UMS3365 – Université de La Réunion.

Acknowledgements. We thank the NOAA ObsPack and ICOS PIs for providing the valuable global CH_4 mole fractions data. We are grateful for the NOAA Global Monitoring Laboratory (NOAA/GML), CSIRO Oceans and Atmosphere, Climate Science Centre (CSIRO), Umweltbundesamt Austria/Environment Agency Austria (EAA), Environment and Climate Change Canada (ECCC), the Finnish Meteorological Institute (FMI), Commissariat à l'énergie atomique et aux énergies alternatives (CEA), Atmospheric Sciences and Climate (ISAC), Ente per le Nuove Tecnologie, l'Energia e l'Ambiente (ENEA), International Foundation High Altitude Research Stations Jungfraujoch and Gornergrat (HFSJG), the Institute for the Institute on Atmospheric Pollution of the National Research Council (IIA), the Institute of Atmospheric Sciences and Climate (ISAC), the Environment Division Global Environment and Marine Department Japan Meteorological Agency (JMA), Joint Research Centre (JRC), Lawrence Berkeley National Laboratory (LBNL-ARM), Laboratoire des Sciences du Climat et de l'Environnement (LSCE), University of Lund (LUND-CEC), the Max Planck Institute for Biogeochemistry (MPIBGC), National Institute for Environmental Studies (NIES), Norwegian Institute for Air Research (NILU), the Pennsylvania State University (PSU), Swedish University of Agricultural Sciences (SLU), University of Bristol (UNIVBRIS), University of Eastern Finland (UEF), University of Exeter (Univ. Exeter), University of Groningen (RUG) and University of Helsinki (UHELS) for performing high-quality CH_4 measurements at global sites and making them available through the NOAA ObsPack and personal communications. The authors would like to thank the ICOS PIs for providing atmospheric CH_4 data (see Table A2). We thank TCCON PIs for providing validation data: Justus Notholt, Institute of Environmental Physics, University of Bremen, Bremen, Germany (Bremen site), Paul O. Wennberg, Division of Engineering and Applied Science, California Institute of Technology, Pasadena, CA, USA (California Institute of Technology, Lamont, Park Falls sites), Nicholas M. Deutscher, Centre for Atmospheric Chemistry, School of Earth, Atmospheric and Life Sciences, University of Wollongong, Wollongong, Australia (Darwin and Wollongong sites), Laura T. Iraci, NASA Ames Research Center, Moffett Field, CA, USA (Armstrong Flight Research Center and Indianapolis sites), Debra Wunch, Department of Physics, University of Toronto, Toronto, Ontario, Canada (East Trout Lake site), Wei Wang, Key Laboratory of Environmental Optics and Technology, Anhui Institute of Optics and Fine Mechanics, Hefei, China (Hefei site) and Martin Steinbacher, Empa, Swiss Federal Laboratories for Materials Science and Technology (Ny-Ålesund site).

Appendix A: Appendix A

Table A1. The ground-based in-situ measurement sites used in InvSURF and evaluation. Observation uncertainty (Obs. Unc.) is sum of measurement and transport model errors used in the observation covariance matrix. Data type is categorized into two: discrete (D) and continuous (C).

ID	Sites	Country/Territory	Laboratory	Longitude [deg. E]	Latitude [deg. N]	Altitude [m a.s.l.]	Obs. Unc. [ppb]	Data type
ABT	Abbotsford, British Columbia	Canada	ECCC	-122.34	49.01	93	30	C
ALT	Alert, Nunavut	Canada	NOAA	-62.51	82.45	190	15	D
ALT	Alert, Nunavut	Canada	ECCC	-62.51	82.45	195	15	C
AMY	Anmyeon-do	Republic of Korea	NOAA	126.33	36.54	87	30	D
ASC	Ascension Island	United Kingdom	NOAA	-14.4	-7.97	90	15	D
ASK	Assekrem	Algeria	NOAA	5.63	23.26	2715	25	D
AZR	Terceira Island, Azores	Portugal	NOAA	-27.36	38.76	24	15	D
AZV	Azovo	Russian Federation	NIES	73.03	54.71	190	30	C
BAR	Baranova	Russian Federation	FMI	101.62	79.28	30	4.5	C
BCK	Behchoko, Northwest Territories	Canada	ECCC	-115.92	62.8	220	15	C
BHD	Baring Head Station	New Zealand	NOAA	174.87	-41.41	90	4.5	D
BKT	Bukit Kototabang	Indonesia	NOAA	100.31	-0.2	875	75	D
BLK	Baker Lake, Nunavut	Canada	ECCC	-96.01	64.33	61	15	C
BMW	Tudor Hill, Bermuda	United Kingdom	NOAA	-64.88	32.26	33	15	D
BRA	Bratt's Lake Saskatchewan	Canada	ECCC	-104.71	50.2	630	75	C
BRW	Barrow Atmospheric Baseline Observatory	United States	NOAA	-156.61	71.32	27	15	C
BRW	Barrow Atmospheric Baseline Observatory	United States	NOAA	-156.58	71.32	16	15	D
BRZ	Berezorechka	Russian Federation	NIES	84.33	56.15	248	75	C
BSD	Bilsdale	United Kingdom	UNIVBRIS	-1.15	54.36	628	30	C
CBA	Cold Bay, Alaska	United States	NOAA	-162.71	55.21	25	15	D
CBY	Cambridge Bay, Nunavut Territory	Canada	ECCC	-105.06	69.13	47	15	C
CFA	Cape Ferguson	Australia	CSIRO	147.06	-19.28	5	25	D
CGO	Cape Grim, Tasmania	Australia	NOAA	144.68	-40.68	164	4.5	D
CGO	Cape Grim	Australia	CSIRO	144.68	-40.68	94	15	C
CGR	Charles Point, Darwin	Australia	CSIRO	12.65	37.67	9	25	C
CHL	Churchill, Manitoba	Canada	ECCC	-93.82	58.74	89	15	C
CHR	Christmas Island	Republic of Kiribati	NOAA	-157.15	1.7	5	15	D
CMN	Mt. Cimone Station	Italy	ICOS-ATC,CNR-ISAC	10.7	44.19	2173	15	C
CPS	Chapais,Quebec	Canada	ECCC	-74.98	49.82	431	15	C
CPT	Cape Point	South Africa	NOAA	18.49	-34.35	260	25	D
CRV	Carbon in Arctic Reservoirs Vulnerability Expe...	United States	NOAA	-147.6	64.99	643	15	C
CRZ	Crozet Island	France	NOAA	51.85	-46.43	202	4.5	D
CUR	Monte Curcio	Italy	IIA	16.42	39.32	1801	15	C
CYA	Casey Station, Antarctica	Australia	CSIRO	110.52	-66.28	55	4.5	D
DEM	Demyanskoe	Russian Federation	NIES	70.87	59.79	155	30	C
DRP	Drake Passage	Drake Passage	NOAA	-61.68	-59.07	10	4.5	D
DSI	Dongsha Island	Taiwan	NOAA	116.73	20.7	8	15	D
DVV	Danville, Virginia	United States	PSU	-79.44	36.71	492	15	C
EGB	Egbert, Ontario	Canada	ECCC	-79.78	44.23	276	25	C
EIC	Easter Island	Chile	NOAA	-109.45	-27.13	72	4.5	D
ENA	Eastern North Atlantic, Graciosa, Azores	Portugal	LBNL-ARM	-28.03	39.09	40	25	C

Table A1. Continuation to Table A1.

ESP	Estevan Point, British Columbia	Canada	ECCC	-126.54	49.38	47	25	C
EST	Esther, Alberta	Canada	ECCC	-110.21	51.67	757	30	C
ETL	East Trout Lake, Saskatchewan	Canada	ECCC	-104.99	54.35	598	30	C
FNE	Fort Nelson, British Columbia	Canada	ECCC	-122.57	58.84	376	30	C
FSD	Fraserdale	Canada	ECCC	-81.57	49.88	250	30	C
GAT	Gartow	Germany	ICOS-ATC,HPB	11.44	53.07	411	25	C
GCI	Millerville, AL	United States	PSU	-85.89	33.18	428	25	C
GMI	Mariana Islands	Guam	NOAA	144.66	13.39	8	15	D
GPA	Gunn Point	Australia	CSIRO	131.04	-12.25	37	75	D
HBA	Halley Station, Antarctica	United Kingdom	NOAA	-26.21	-75.61	35	4.5	D
HNP	Hanlan's Point, Ontario	Canada	ECCC	-79.39	43.61	97	25	C
HPB	Hohenpeissenberg	Germany	ICOS-ATC,HPB	11.02	47.8	1065	25	C
HSU	Humboldt State University	United States	NOAA	-124.44	41.57	8	30	D
HTM	Hyltemossa	Sweden	ICOS-ATC,LUND-CEC	13.42	56.1	265	25	C
ICE	Storhofdi, Vestmannaeyjar	Iceland	NOAA	-20.29	63.4	122	15	D
INU	Inuvik,Northwest Territories	Canada	ECCC	-133.53	68.32	123	15	C
IPR	Ispra	Italy	ICOS-ATC,JRC	8.64	45.81	310	30	C
IZO	Izana, Tenerife, Canary Islands	Spain	NOAA	-16.48	28.3	2378	25	D
JFJ	Jungfraujoch	Switzerland	ICOS-ATC,HFSJG	7.99	46.55	3585	15	C
KEY	Key Biscayne, Florida	United States	NOAA	-80.2	25.67	6	25	D
KIT	Karlsruhe	Germany	ICOS-ATC,HPB	8.42	49.09	310	30	C
KJN	Kjölnes	Norway	Univ. Exeter	29.23	70.85	20	15	C
KMP	Kumpula	Finland	FMI	24.96	60.2	53	30	C
KRE	Kresin u Pacova	Czech Republic	ICOS	15.08	49.57	784	25	C
KRS	Karasevoe	Russian Federation	NIES	82.42	58.25	156	30	C
KUM	Cape Kumukahi, Hawaii	United States	NOAA	-155.01	19.51	3	15	D
LEF	Park Falls, Wisconsin	United States	NOAA	-90.27	45.95	868	30	C
LIN	Lindenberg	Germany	ICOS-ATC,HPB	14.12	52.17	171	30	C
LLB	Lac La Biche, Alberta	Canada	ECCC	-112.47	54.95	590	30	C
LLN	Lulin	Taiwan	NOAA	120.86	23.47	2867	25	D
LMP	Lampedusa	Italy	ICOS-ATC,ENEA	12.63	35.52	53	25	C
LMT	Lamezia Terme	Italy	ISAC	16.23	38.88	14	30	C
LUT	Lutjewad	Netherlands	ICOS-ATC,RUG	6.35	53.4	61	25	C
MAA	Mawson, Antarctica	Australia	CSIRO	62.87	-67.62	32	4.5	D
MEX	High Altitude Global Climate Observation Center	Mexico	NOAA	-97.31	18.98	4469	15	D
MID	Sand Island, Midway	United States	NOAA	-177.38	28.21	8	15	D
MLO	Mauna Loa, Hawaii	United States	NOAA	-155.58	19.54	3437	15	C/D
MNM	Minamitorishima	Japan	JMA	153.98	24.29	27	15	C
MQA	Macquarie Island	Australia	CSIRO	158.97	-54.48	13	4.5	D
MRC	Marcellus Pennsylvania	United States	PSU	-76.42	41.47	652	75	C

Table A1. Continuation of Table A1.

NAT	Farol De Mae Luiza Lighthouse	Brazil	NOAA	-35.19	-5.51	20	15	D
NMB	Gobabeb	Namibia	NOAA	15.01	-23.58	461	25	D
NOR	Norunda	Sweden	ICOS-ATC,LUND-CEC	17.48	60.09	146	15	C
NOY	Noyabrsk	Russian Federation	NIES	75.78	63.43	188	30	C
NWR	Niwot Ridge, Colorado	United States	NOAA	-105.57	40.05	3526	15	D
OPE	Observatoire perenne de l'environnement	France	ICOS-ATC,LSCE	5.5	48.56	510	30	C
OXK	Ochsenkopf	Germany	ICOS-ATC,CAL-FCL	11.81	50.03	1185	30	C
PAL	Pallas-Sammaltunturi, GAW Station	Finland	ICOS-ATC,FMI	24.12	67.97	577	15	C
PDM	Pic du Midi	France	LSCE	0.14	42.94	2887	15	D
POC	Pacific Ocean	Pacific Ocean	NOAA	-130.75	0.12	20	15	D
PSA	Palmer Station, Antarctica	United States	NOAA	-64.05	-64.77	15	4.5	D
PUI	Puijo	Finland	ICOS-ATC,UEF	27.66	62.91	84	30	C
PUY	Puy de Dome	France	ICOS-ATC,LSCE	2.97	45.77	1475	15	C
RPB	Ragged Point	Barbados	NOAA	-59.43	13.16	20	15	D
RUN	La Réunion	France	ICOS-ATC,LSCE	55.38	-21.08	2160	15	C
RYO	Ryori	Japan	JMA	141.82	39.03	280	15	C
SAC	Saclay	France	ICOS-ATC,CEA	2.14	48.72	260	75	C
SCT	Beech Island, South Carolina	United States	NOAA	-81.83	33.41	420	75	C
SDZ	Shangdianzi	China	NOAA	117.12	40.65	298	15	D
SEY	Mahe Island	Seychelles	NOAA	55.53	-4.68	7	15	D
SGP	Southern Great Plains, Oklahoma	United States	NOAA	-97.5	36.62	339	75	D
SGP	Southern Great Plains, Oklahoma	United States	LBNL-ARM	-97.49	36.61	374	75	C
SHM	Shemya Island, Alaska	United States	NOAA	174.08	52.72	28	25	D
SMO	Tutuila	American Samoa	NOAA	-170.56	-14.23	60	15	D
SMR	Hyytiala	Finland	ICOS-ATC,UHELS	24.29	61.85	306	25	C
SNB	Sonnblick	Austria	EAA	47.05	12.96	3111	15	C
SOD	Sodanyklä	Finland	FMI	26.64	67.36	227	25	C
SPO	South Pole, Antarctica	United States	NOAA	-24.8	-89.96	2821	4.5	D
STE	Steinkimmen	Germany	ICOS-ATC,HPB	8.46	53.04	281	75	C
SUM	Summit	Greenland	NOAA	-38.42	72.6	3215	15	D
SVB	Svartberget	Sweden	ICOS-ATC,SLU	19.77	64.26	419	25	C
SYO	Syowa Station, Antarctica	Japan	NOAA	39.59	-69	16	4.5	D
TAC	Tacolneston	United Kingdom	NOAA	1.14	52.52	236	25	D
TAP	Tae-ahn Peninsula	Republic of Korea	NOAA	126.13	36.73	21	75	D
THD	Trinidad Head, California	United States	NOAA	-124.15	41.05	112	25	D
TIK	Hydrometeorological Observatory of Tiksi	Russia	NOAA	128.89	71.6	29	15	D
TIK	Tiksi	Russian Federation	FMI	128.89	71.6	29	15	C

Table A1. Continuation of Table A1.

TOH	Torfhaus	Germany	ICOS-ATC,HPB	10.53	51.81	948	25	C
TPD	Turkey Point, Ontario	Canada	ECCC	-80.56	42.64	266	25	C
TRN	Trainou	France	ICOS-ATC,LSCE	2.11	47.96	311	25	C
USH	Ushuaia	Argentina	NOAA	-68.31	-54.85	32	4.5	D
UTA	Wendover, Utah	United States	NOAA	-113.72	39.9	1332	25	D
UTO	Uto	Finland	ICOS-ATC,FMI	21.37	59.78	65	25	C
UUM	Ulaan Uul	Mongolia	NOAA	111.1	44.45	1012	25	D
VGN	Vaganovo	Russian Federation	NIES	62.32	54.5	277	30	C
WIS	Weizmann Institute of Science at the Arava Ins...	Israel	NOAA	35.06	29.96	482	25	D
WLG	Mt. Waliguan	Peoples Republic of China	NOAA	100.9	36.27	3890	15	D
WSA	Sable Island, Nova Scotia	Canada	ECCC	-60.01	43.93	8	25	C
YON	Yonagunijima	Japan	JMA	123.01	24.47	50	30	C
ZEP	Ny-Alesund, Svalbard	Norway and Sweden	ICOS-ATC,NILU	11.89	78.91	489	15	C
ZOT	Zotino	Russian Federation	MPIBGC	89.21	60.48	415	25	C

Table A2. List of the ICOS sites, data categories, PIs and references for the sites used in InvSURF and evaluation.

Site code	Data category	Authors	References
CMN	ICOS ATC NRT CH4 growing time series	Cristofanelli, Paolo and Trisolino, Pamela	Cristofanelli and Trisolino (2022)
CMN	ICOS ATC CH4 Release	Cristofanelli, Paolo and Trisolino, Pamela	Cristofanelli and Trisolino (2021)
GAT	ICOS ATC NRT CH4 growing time series	Kubistin, Dagmar and Plaß-Dülmer, Christian and Kneuer, Tobias and Lindauer, Matthias and Müller-Williams, Jennifer	Kubistin et al. (2022a)
GAT	ICOS ATC CH4 Release	Kubistin, Dagmar and Plaß-Dülmer, Christian and Arnold, Sabrina and Lindauer, Matthias and Müller-Williams, Jennifer and Schumacher, Marcus	Kubistin et al. (2021c)
HPB	ICOS ATC NRT CH4 growing time series	Kubistin, Dagmar and Plaß-Dülmer, Christian and Kneuer, Tobias and Lindauer, Matthias and Müller-Williams, Jennifer	Kubistin et al. (2022b)
HPB	ICOS ATC CH4 Release	Kubistin, Dagmar and Plaß-Dülmer, Christian and Arnold, Sabrina and Lindauer, Matthias and Müller-Williams, Jennifer and Schumacher, Marcus	Kubistin et al. (2021d)
HTM	ICOS ATC NRT CH4 growing time series	Heliasz, Michal and Biermann, Tobias	Heliasz and Biermann (2022)
HTM	ICOS ATC CH4 Release	Heliasz, Michal and Biermann, Tobias	Heliasz and Biermann (2021)
IPR	ICOS ATC NRT CH4 growing time series	Manca, Giovanni	Manca (2022)
IPR	ICOS ATC CH4 Release	Bergamaschi, Peter and Manca, Giovanni	Bergamaschi and Manca (2021)
JFJ	ICOS ATC NRT CH4 growing time series	Emmenegger, Lukas and Leuenberger, Markus and Steinbacher, Martin	Emmenegger et al. (2022)
JFJ	ICOS ATC CH4 Release	Emmenegger, Lukas and Leuenberger, Markus and Steinbacher, Martin	Emmenegger et al. (2021)
KIT	ICOS ATC NRT CH4 growing time series	Kubistin, Dagmar and Plaß-Dülmer, Christian and Kneuer, Tobias and Lindauer, Matthias and Müller-Williams, Jennifer	Kubistin et al. (2022c)
KIT	ICOS ATC CH4 Release	Kubistin, Dagmar and Plaß-Dülmer, Christian and Arnold, Sabrina and Lindauer, Matthias and Müller-Williams, Jennifer and Schumacher, Marcus	Kubistin et al. (2021e)
KRE	ICOS ATC NRT CH4 growing time series	Marek, Michal V. and Vítková, Gabriela and Komínková, Kateřina	Marek et al. (2022)
KRE	ICOS ATC CH4 Release	Marek, Michal V. and Vítková, Gabriela and Komínková, Kateřina	Marek et al. (2021)
LIN	ICOS ATC NRT CH4 growing time series	Kubistin, Dagmar and Plaß-Dülmer, Christian and Kneuer, Tobias and Lindauer, Matthias and Müller-Williams, Jennifer	Kubistin et al. (2022d)
LIN	ICOS ATC CH4 Release	Kubistin, Dagmar and Plaß-Dülmer, Christian and Arnold, Sabrina and Lindauer, Matthias and Müller-Williams, Jennifer and Schumacher, Marcus	Kubistin et al. (2021f)
LMP	ICOS ATC NRT CH4 growing time series	di Sarra, Alcide and Piacentino, Salvatore	di Sarra and Piacentino (2022)
LMP	ICOS ATC CH4 Release	di Sarra, Alcide and Piacentino, Salvatore	di Sarra and Piacentino (2021)
LUT	ICOS ATC NRT CH4 growing time series	Chen, Huilin and Scheeren, Bert	Chen and Scheeren (2022)
LUT	ICOS ATC CH4 Release	Chen, Huilin and Scheeren, Bert	Chen and Scheeren (2021)
NOR	ICOS ATC NRT CH4 growing time series	Lehner, Irene and Mölder, Meelis	Lehner and Mölder (2022)
NOR	ICOS ATC CH4 Release	Lehner, Irene and Mölder, Meelis	Lehner and Mölder (2021)
OPE	ICOS ATC NRT CH4 growing time series	Ramonet, Michel and Conil, Sébastien and Delmotte, Marc and Laurent, Olivier and Lopez, Morgan	Ramonet et al. (2022a)
OPE	ICOS ATC CH4 Release	Ramonet, Michel and Conil, Sébastien and Delmotte, Marc and Laurent, Olivier	Ramonet et al. (2021a)
OXK	ICOS ATC NRT CH4 growing time series	Kubistin, Dagmar and Plaß-Dülmer, Christian and Kneuer, Tobias and Lindauer, Matthias and Müller-Williams, Jennifer	Kubistin et al. (2022e)
OXK	ICOS ATC CH4 Release	Kubistin, Dagmar and Plaß-Dülmer, Christian and Arnold, Sabrina and Lindauer, Matthias and Müller-Williams, Jennifer	Kubistin et al. (2021a)
PAL	ICOS ATC NRT CH4 growing time series	Hatakka, Juha	Hatakka (2022)
PAL	ICOS ATC CH4 Release	Hatakka, Juha	Hatakka (2021)
PUI	ICOS ATC NRT CH4 growing time series	Lehtinen, Kari and Leskinen, Ari	Lehtinen and Leskinen (2022)
PUY	ICOS ATC NRT CH4 growing time series	Colomb, Aurélie and Ramonet, Michel and Yver-Kwok, Camille and Delmotte, Marc and Lopez, Morgan and Pichon, Jean-Marc	Colomb et al. (2022)
PUY	ICOS ATC CH4 Release	Colomb, Aurélie and Ramonet, Michel and Yver-Kwok, Camille and Delmotte, Marc and Pichon, Jean-Marc	Colomb et al. (2021)
RUN	ICOS ATC NRT CH4 growing time series	De Mazière, Martine and Sha, Mahesh Kumar and Ramonet, Michel	De Mazière et al. (2022b)
RUN	ICOS ATC CH4 Release	De Mazière, Martine and Sha, Mahesh Kumar and Ramonet, Michel	De Mazière et al. (2021)
SAC	ICOS ATC NRT CH4 growing time series	Ramonet, Michel and Delmotte, Marc and Lopez, Morgan	Ramonet et al. (2022b)
SAC	ICOS ATC CH4 Release	Ramonet, Michel and Delmotte, Marc	Ramonet and Delmotte (2021)
SMR	ICOS ATC NRT CH4 growing time series	Mammarella, Ivan	Mammarella (2022)
SMR	ICOS ATC CH4 Release	Levula, Janne and Mammarella, Ivan	Levula and Mammarella (2021)
STE	ICOS ATC NRT CH4 growing time series	Kubistin, Dagmar and Plaß-Dülmer, Christian and Kneuer, Tobias and Lindauer, Matthias and Müller-Williams, Jennifer	Kubistin et al. (2022f)
STE	ICOS ATC CH4 Release	Kubistin, Dagmar and Plaß-Dülmer, Christian and Arnold, Sabrina and Lindauer, Matthias and Müller-Williams, Jennifer	Kubistin et al. (2021b)
SVB	ICOS ATC NRT CH4 growing time series	Smith, Paul and Marklund, Per	Smith and Marklund (2022)
SVB	ICOS ATC CH4 Release	Marklund, Per and Ottosson-Löfvenius, Mikaell and Smith, Paul	Marklund et al. (2021)
TOH	ICOS ATC NRT CH4 growing time series	Kubistin, Dagmar and Plaß-Dülmer, Christian and Kneuer, Tobias and Lindauer, Matthias and Müller-Williams, Jennifer	Kubistin et al. (2022g)
TOH	ICOS ATC CH4 Release	Kubistin, Dagmar and Plaß-Dülmer, Christian and Arnold, Sabrina and Lindauer, Matthias and Müller-Williams, Jennifer and Schumacher, Marcus	Kubistin et al. (2021g)
TRN	ICOS ATC NRT CH4 growing time series	Ramonet, Michel and Lopez, Morgan and Delmotte, Marc	Ramonet et al. (2022c)
TRN	ICOS ATC CH4 Release	Ramonet, Michel and Lopez, Morgan and Delmotte, Marc	Ramonet et al. (2021b)
UTO	ICOS ATC NRT CH4 growing time series	Hatakka, Juha and Laurila, Tuomas	Hatakka and Laurila (2022)
UTO	ICOS ATC CH4 Release	Laurila, Tuomas	Laurila (2021)
ZEP	ICOS ATC NRT CH4 growing time series	Lund Myhre, Cathrine and Platt, Stephen Matthew and Hermansen, Ove and Lunder, Chris	Lund Myhre et al. (2022)
ZEP	ICOS ATC CH4 Release	Lund Myhre, Cathrine and Platt, Stephen Matthew and Hermansen, Ove and Lunder, Chris	Lund Myhre et al. (2021)

Table A3. The TCCON sites used for evaluation.

ID	Station Name, Location	Latitude	Longitude	References
br	Bremen, Germany	53.1°N	8.85°E	Notholt et al. (2022)
bu	Burgos, Philippines	18.53°N	120.65°E	Morino et al. (2022c)
ci	California Institute of Technology, USA	34.14°N	118.13°W	Wennberg et al. (2022b)
db	Darwin, Australia	12.46°S	130.89°E	Deutscher et al. (2023b)
df	Armstrong Flight Research Center, USA	34.96°N	117.88°W	Iraci et al. (2022)
et	East Trout Lake, Canada	54.36°N	104.99°W	Wunch et al. (2002)
eu	Eureka, Canada	80.05°N	86.42°W	Strong et al. (2022)
gm	Garmisch, Germany	47.48°N	11.06°E	Sussmann and Rettinger (2017)
hf	Hefei, China	31.9°N	117.17°E	Liu et al. (2023)
iz	Izaña, Spain	28.3°N	16.5°W	Blumenstock et al. (2017)
js	Saga, Japan	33.24°N	130.29°E	Shiomi et al. (2022)
ka	Karlsruhe, Germany	49.1°N	8.44°E	Hase et al. (2022)
ll	Lauder, New Zealand	45.04°S	169.68°E	Sherlock et al. (2022)
ni	Nicosia, Cyprus	35.14°N	33.38°E	Petri et al. (2023)
ny	Ny Ålesund, Norway	78.92°N	11.92°E	Buschmann et al. (2022)
oc	Lamont, USA	36.6°N	97.49°W	Wennberg et al. (2022c)
or	Orleans, France	47.97°N	2.11°E	Warneke et al. (2022)
pa	Park Falls, USA	45.94°N	90.27°W	Wennberg et al. (2022a)
pr	Paris, France	48.85°N	2.36°E	Te et al. (2022)
ra	Reunion Island, France	20.9°S	55.49°E	De Mazière et al. (2022a)
rj	Rikubetsu, Japan	43.46°N	143.77°E	Morino et al. (2022a)
so	Sodankylä, Finland	67.37°N	26.63°E	Kivi et al. ((2022)
tk	Tsukuba, Japan	36.05°N	140.12°E	Morino et al. (2022b)
wg	Wollongong, Australia	34.41°S	150.88°E	Deutscher et al. (2023a)
xh	Xianghe, China	39.8°N	116.96°E	Zhou et al. (2022)
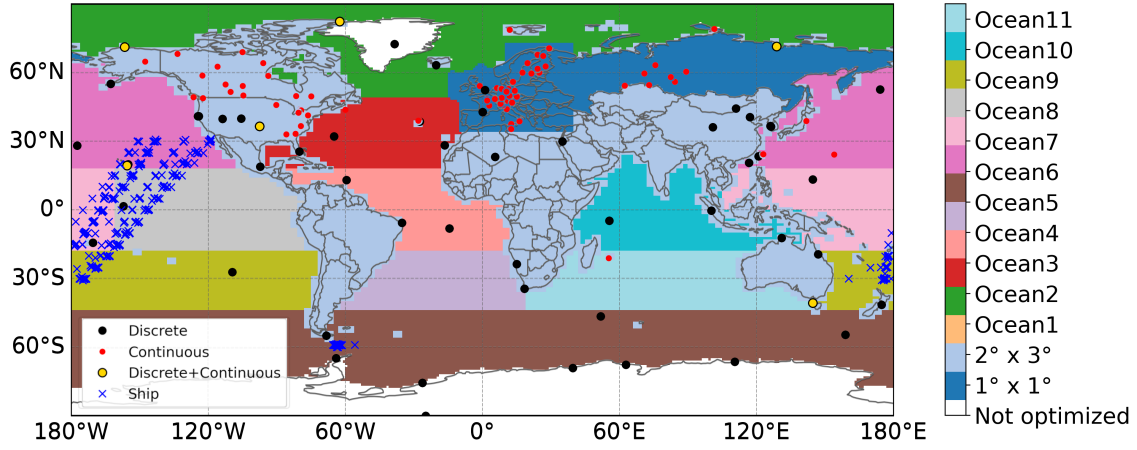
Figure A1. Location of ground-based surface observations (dots and x-marks) assimilated in the InvSURF inversion experiment (see section 2.4), and optimization regions used in CTE-CH$_4$ (background colours). Over land areas, the fluxes were optimized grid-wise, and ocean region-wise.
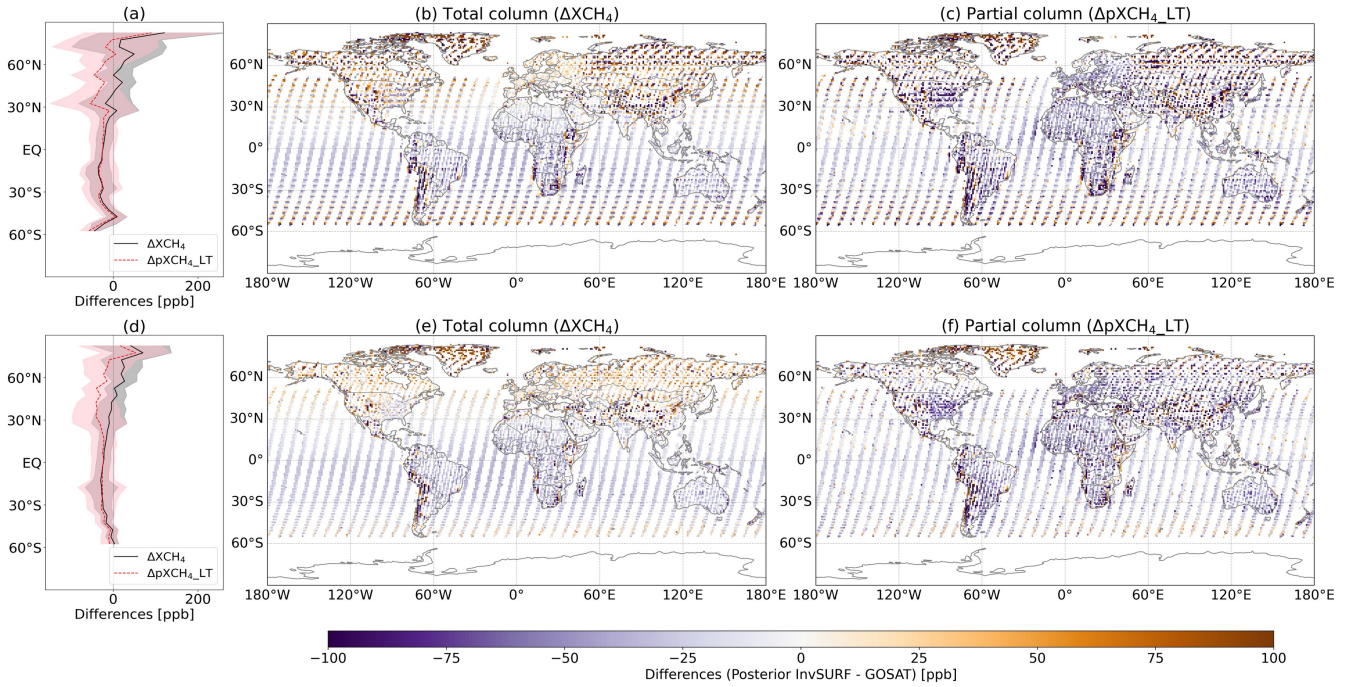
Figure A2. Mean differences between prior mole fractions and JAXA/GOSAT retrievals, averaged over 2016–2019. (a) and (d) five degree latitudinal means (solid line) with standard deviation (shaded area), and (b), (c), (e) and (f) 1° × 1° grid means. (a), (b) and (c) were calculated using TM5 with 1° × 1° zoom over Europe and 6° × 4° globally, and (d), (e) and (f) using 2° × 3° (latitude × longitude) globally. Positive values indicate posterior InvSURF mole fractions being higher than the GOSAT retrievals.
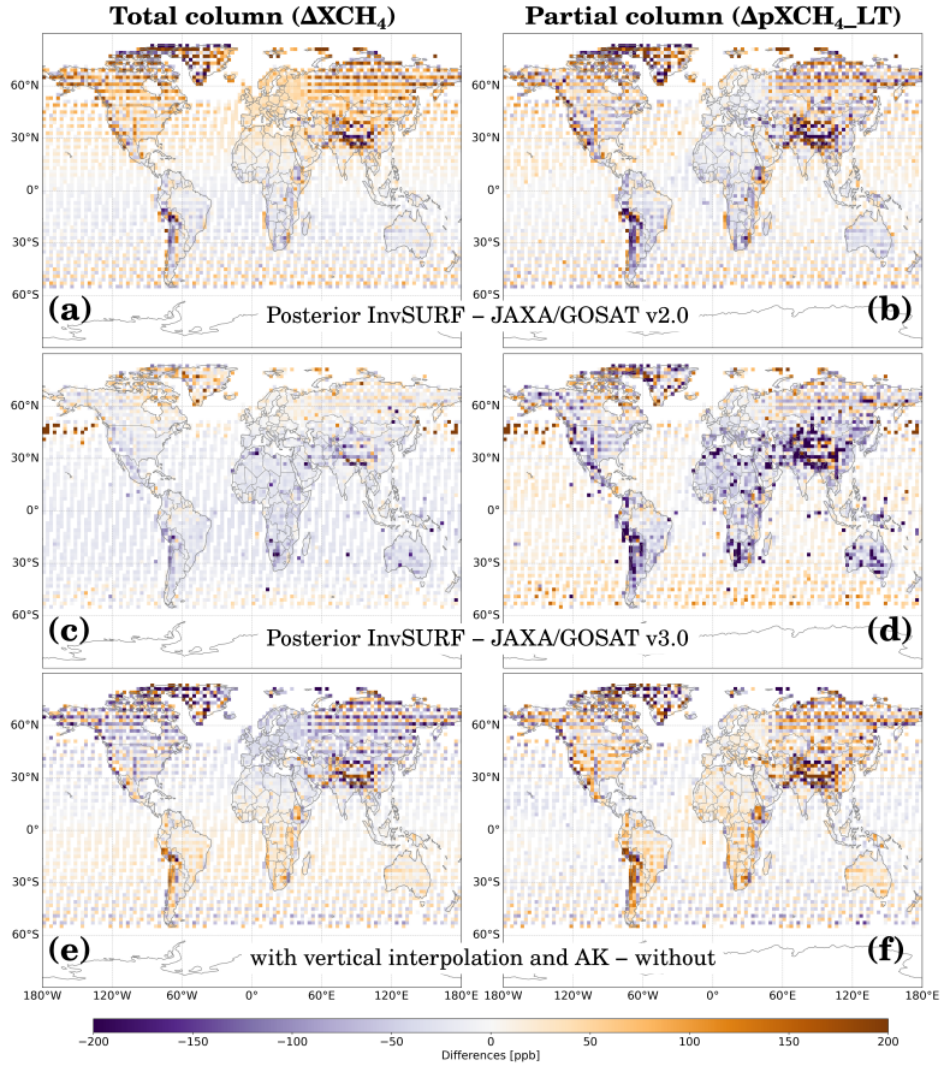
Figure A3. (a)-(d) Mean differences between posterior InvSURF and JAXA/GOSAT retrievals averaged over 2016 and at $2° \times 3°$ grids. Positive values indicate posterior InvSURF mole fractions being higher than the JAXA/GOSAT retrievals. (a) and (b) compared to v2.0, without averaging kernels and vertical interpolation. (c) and (d) compared to v3.0 with vertical interpolation and averaging kernels applied. (e) and (f) are comparisons of modelled values between those calculated with vertical interpolation and AK (i.e. posterior InvSURF values from (c) and (d)) and those without interpolation and AK (i.e. posterior InvSURF values from (a) and (b)), illustrating the effect of interpolation and AK directly. Positive values indicate higher mole fraction values with interpolation and AK. (a), (c), (e) are comparisons of total columns and (b), (d), (f) are of lower tropospheric partial columns.
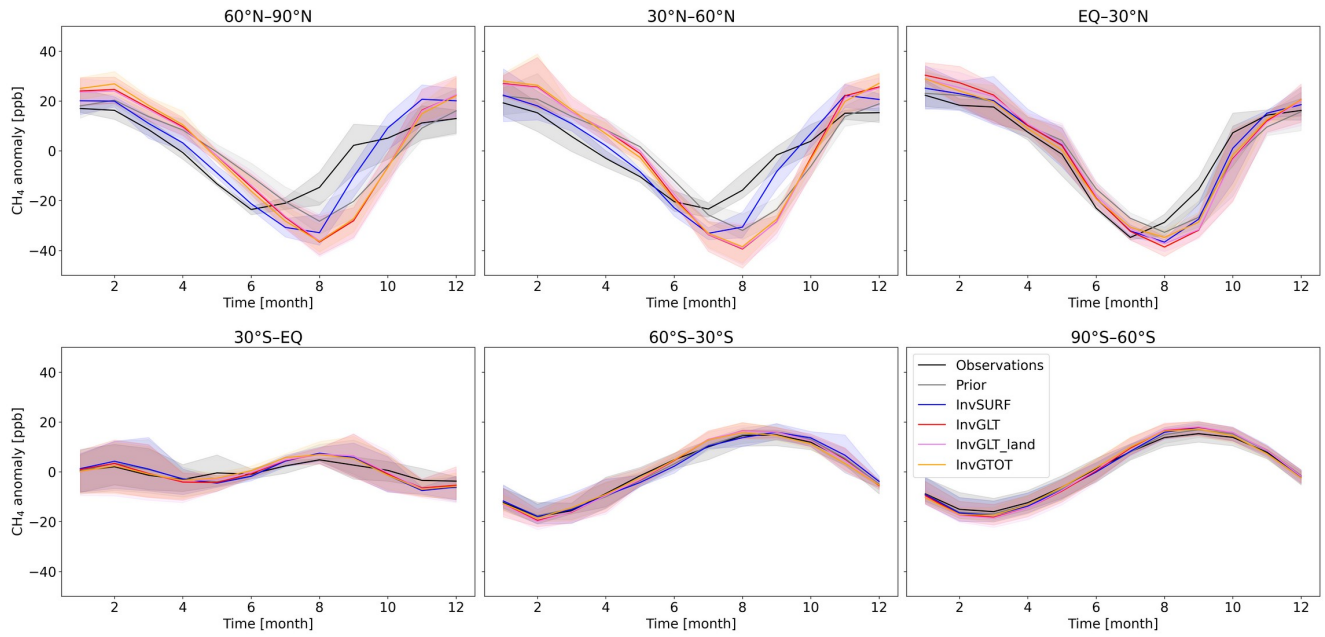
Figure A4. Detrended monthly average mole fractions at surface stations, assimilated in InvSURF. The data is averaged from 2016–2019 and at 30° latitudinal bands. Shaded areas are minimum and maximum of detrended monthly values within 2016–2019.
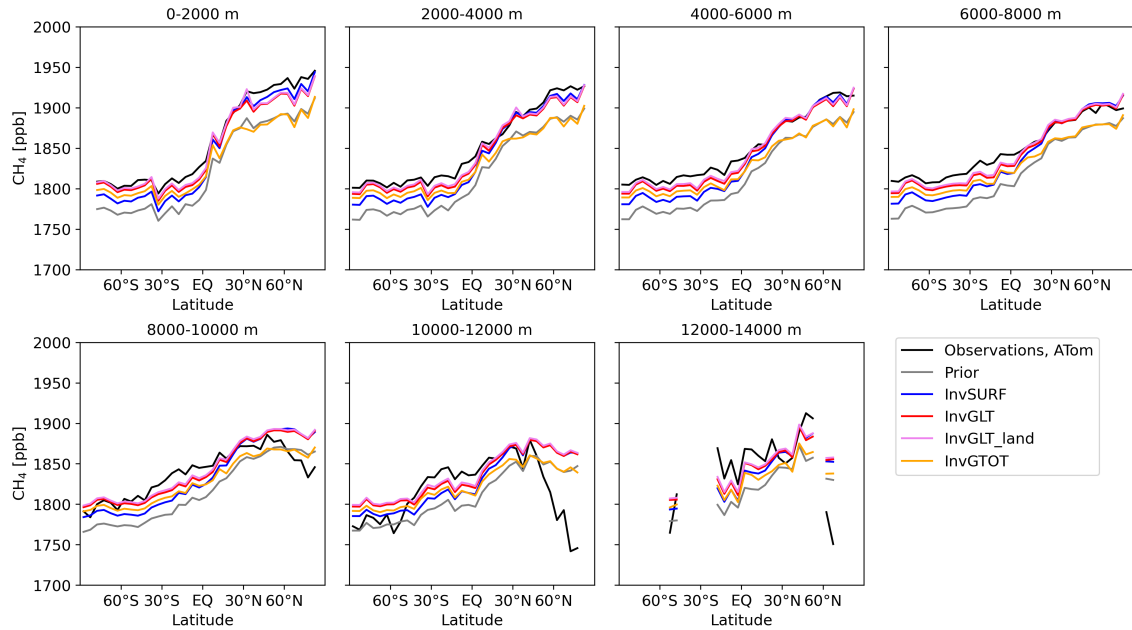
Figure A5. Mean atmospheric CH_4 at location and time of aircraft measurements from Atmospheric Tomography Mission, averaged over five degree latitude bands and 2000 m altitude bands above sea level during 2016–2019.
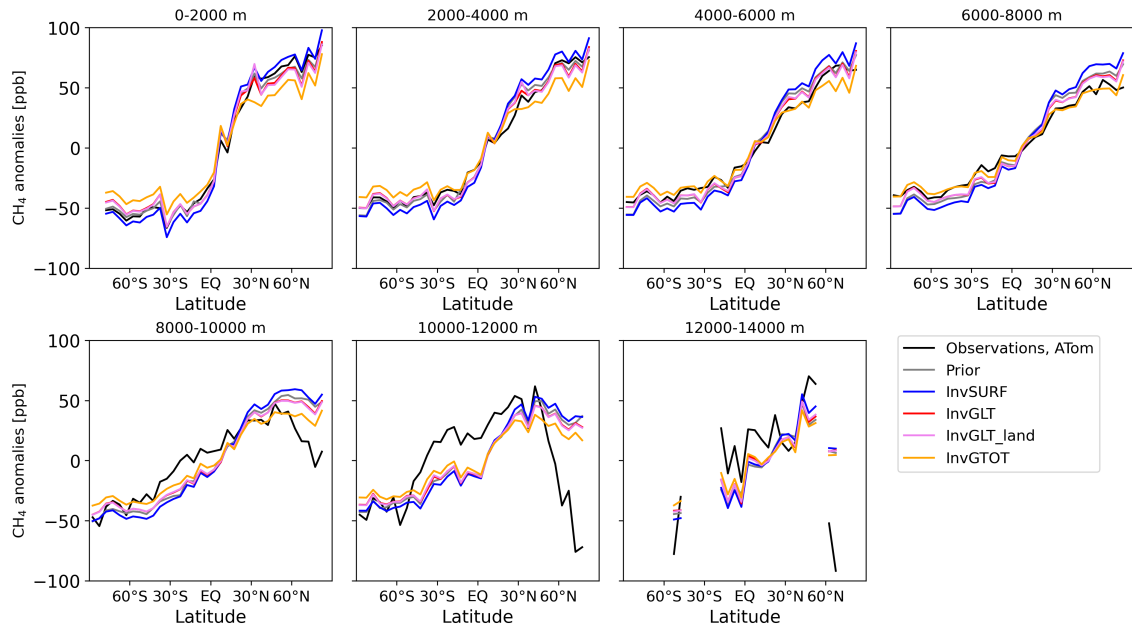
Figure A6. As in A5, but means were subtracted at each altitude bands.
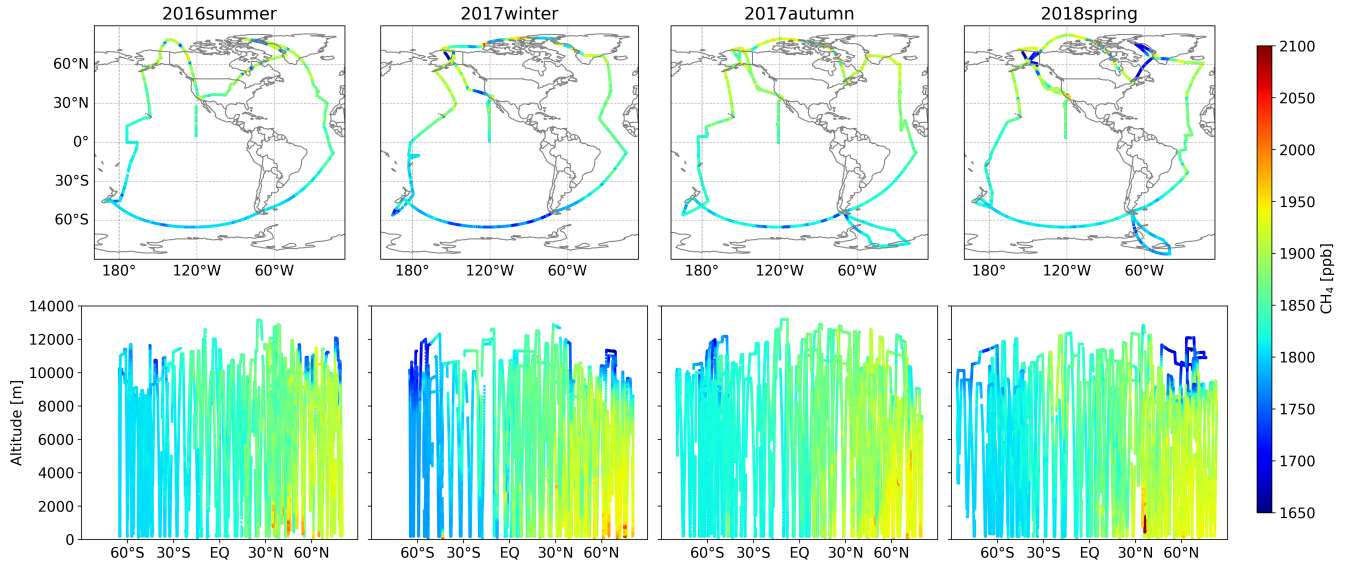
Figure A7. Observed CH$_4$ mole fractions from aircraft measurements of Atmospheric Tomography Mission during the study period.
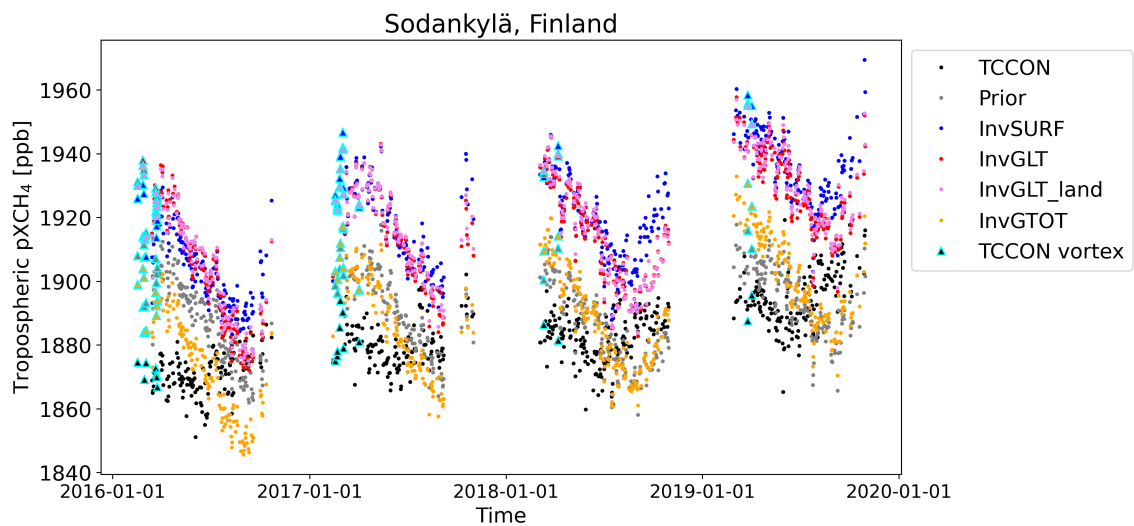
Figure A8. Daily averaged tropospheric partial columns at the Sodankylä TCCON station, Finland.
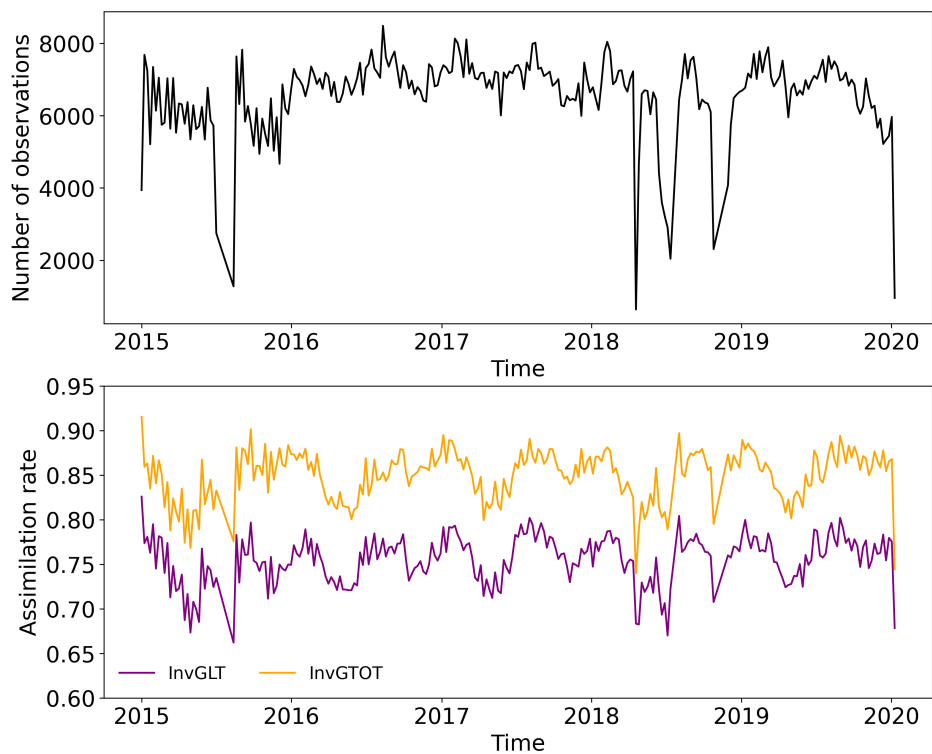
Figure A9. Global total number of JAXA/GOSAT observations per week and assimilation rates in GOSAT inversions. The x-axis is weeks of optimization steps, and not the actual time of observation.
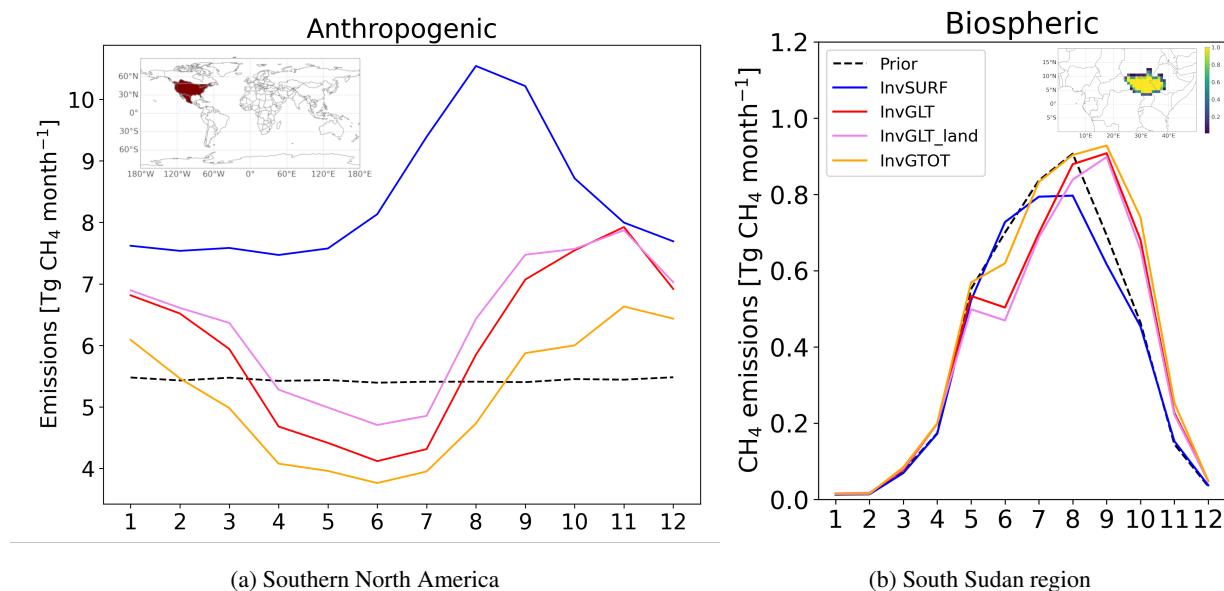
Figure A10. Average monthly CH_4 emissions in (a) southern North America and (b) South Sudan regions. The maps illustrate aggregated areas.

References

Aalto, T., Tsuruta, A., Mäkelä, J., Mueller, J., Tenkanen, M., Burke, E., Chadburn, S., Gao, Y., Mannisenaho, V., Kleinen, T., Lee, H., Leppänen, A., Markkanen, T., Materia, S., Miller, P., Peano, D., Peltola, O., Poulter, B., Raivonen, M., Saunois, M., Wårlind, D., and Zaehle, S.: Air temperature and precipitation constraining the modelled wetland methane emissions in a boreal region in Northern Europe, EGUsphere, pp. 1–31, https://doi.org/10.5194/egusphere-2023-2873, publisher: Copernicus GmbH, 2024.

Alexe, M., Bergamaschi, P., Segers, A., Detmers, R., Butz, A., Hasekamp, O., Guerlet, S., Parker, R., Boesch, H., Frankenberg, C., Scheepmaker, R. A., Dlugokencky, E., Sweeney, C., Wofsy, S. C., and Kort, E. A.: Inverse modelling of CH_4 emissions for 2010–2011 using different satellite retrieval products from GOSAT and SCIAMACHY, Atmospheric Chemistry and Physics, 15, 113–133, https://doi.org/10.5194/acp-15-113-2015, 2015.

Baray, S., Jacob, D. J., Maasakkers, J. D., Sheng, J.-X., Sulprizio, M. P., Jones, D. B. A., Bloom, A. A., and McLaren, R.: Estimating 2010–2015 anthropogenic and natural methane emissions in Canada using ECCC surface and GOSAT satellite observations, Atmospheric Chemistry and Physics, 21, 18 101–18 121, https://doi.org/10.5194/acp-21-18101-2021, publisher: Copernicus GmbH, 2021.

Bergamaschi, P. and Manca, G.: ICOS ATC CH4 Release, Ispra (100.0 m), 2017-12-15–2021-01-31, ICOS RI, https://hdl.handle.net/11676/36LdPE4ASUAJKyNS1G3ki6GH, 2021.

Blumenstock, T., Hase, F., Schneider, M., García, O., and Sepúlveda, E.: TCCON data from Izana, Tenerife, Spain, Release GGG2020R0, TCCON Data Archive, hosted by CaltechDATA, https://doi.org/10.14291/tccon.ggg2020.izana01.R1, 2017.

Boone, C. D., Bernath, P. F., Walker, K. A., McLeod, S. D., Rinsland, C. P., Froidevaux, L., and Waters, J. W.: Version 4 retrievals for the atmospheric chemistry experiment Fourier transform spectrometer (ACE-FTS) and imagers, Journal of Quantitative Spectroscopy and Radiative Transfer, 254, 106 939, https://doi.org/10.1016/j.jqsrt.2020.106939, 2020.

Bovensmann, H., Burrows, J. P., Buchwitz, M., Frerick, J., Noël, S., Rozanov, V. V., Chance, K. V., and Goede, A. P. H.: SCIAMACHY: Mission Objectives and Measurement Modes, Journal of the Atmospheric Sciences, 56, 127–150, https://journals.ametsoc.org/view/journals/atsc/56/2/1520-0469_1999_056_0127_smoamm_2.0.co_2.xml, 1999.

Buschmann, M., Petri, C., Palm, M., Warneke, T., Notholt, J., and Engineers., A. S.: TCCON data from Ny-Alesund, Svalbard, Norway, Release GGG2020R0, TCCON Data Archive, hosted by CaltechDATA, https://doi.org/10.14291/tccon.ggg2020.nyalesund01.R0, 2022.

Chen, H. and Scheeren, B.: ICOS ATC CH4 Release, Lutjewad (60.0 m), 2018-08-13–2021-01-31, ICOS RI, https://hdl.handle.net/11676/xEwwhYoXrErQMLeo8Na4yVe2, 2021.

Chen, H. and Scheeren, B.: ICOS ATC NRT CH4 growing time series, Lutjewad (60.0 m), 2021-02-01–2022-06-07, https://hdl.handle.net/11676/C7auOon8En7P8VxdPjbZOHkv, 2022.

Chen, Z., Jacob, D. J., Nesser, H., Sulprizio, M. P., Lorente, A., Varon, D. J., Lu, X., Shen, L., Qu, Z., Penn, E., and Yu, X.: Methane emissions from China: a high-resolution inversion of TROPOMI satellite observations, Atmospheric Chemistry and Physics, 22, 10 809–10 826, https://doi.org/10.5194/acp-22-10809-2022, publisher: Copernicus GmbH, 2022.

Colomb, A., Ramonet, M., Yver-Kwok, C., Delmotte, M., and Pichon, J.-M.: ICOS ATC CH4 Release, Puy de Dôme (10.0 m), 2016-08-25–2021-01-31, ICOS RI, https://hdl.handle.net/11676/iko4P7GYGpLWz6Wi87K0FEVf, 2021.

Colomb, A., Ramonet, M., Yver-Kwok, C., Delmotte, M., Lopez, M., and Pichon, J.-M.: ICOS ATC NRT CH4 growing time series, Puy de Dôme (10.0 m), 2021-02-01–2022-06-15, https://hdl.handle.net/11676/mWHXZu1FCkPYSC7daRpXEoqg, 2022.

Crippa, M., Guizzardi, D., Pagani, F., Banja, M., Muntean, M., E., S., Becker, W., Monforti-Ferrario, F., Quadrelli, R., Risquez Martin, A., Taghavi-Moharamli, P., Köykkä, J., Grassi, G., Rossi, S., Brandao De Melo, J., Oom, D., Branco, A., San-Miguel, J., and Vignati, E.: GHG emissions of all world countries, Publications Office of the European Union, Luxembourg, https://doi.org/10.2760/953322, 2023.

Cristofanelli, P. and Trisolino, P.: ICOS ATC CH4 Release, Monte Cimone (8.0 m), 2018-05-03–2021-01-31, ICOS RI, https://hdl.handle.net/11676/D_xwBYaUA-pigw4IxFw_IhEV, 2021.

Cristofanelli, P. and Trisolino, P.: ICOS ATC NRT CH4 growing time series, Monte Cimone (8.0 m), 2021-02-01–2022-06-15, ICOS RI, https://hdl.handle.net/11676/G8Mg3vbkK2E93p040-rIGdml, 2022.

De Mazière, M., Sha, M. K., and Ramonet, M.: ICOS ATC CH4 Release, La Réunion (6.0 m), 2018-05-17–2021-01-31, ICOS RI, https://hdl.handle.net/11676/wEUznG1oXEKYZr823-SFfP4m, 2021.

De Mazière, M., Sha, M. K., Desmet, F., Hermans, C., Scolas, F., Kumps, N., Zhou, M., Metzger, J.-M., Duflot, V., and Cammas, J.-P.: TCCON data from Reunion Island (La Reunion), France, Release GGG2020R0, TCCON Data Archive, hosted by CaltechDATA, https://doi.org/10.14291/tccon.ggg2020.reunion01.R0, 2022a.

De Mazière, M., Sha, M. K., and Ramonet, M.: ICOS ATC NRT CH4 growing time series, La Réunion (6.0 m), 2021-02-01–2022-06-15, https://hdl.handle.net/11676/3wMlMVvbNanOuxKVzNrhr1SH, 2022b.

Deng, Z., Ciais, P., Hu, L., Martinez, A., Saunois, M., Thompson, R. L., Tibrewal, K., Peters, W., Byrne, B., Grassi, G., Palmer, P. I., Luijkx, I. T., Liu, Z., Liu, J., Fang, X., Wang, T., Tian, H., Tanaka, K., Bastos, A., Sitch, S., Poulter, B., Albergel, C., Tsuruta, A., Maksyutov, S., Janardanan, R., Niwa, Y., Zheng, B., Thanwerdas, J., Belikov, D., Segers, A., and Chevallier, F.: Global Greenhouse Gas Reconciliation 2022, Earth System Science Data Discussions, pp. 1–47, https://doi.org/10.5194/essd-2024-103, publisher: Copernicus GmbH, 2024.

Deutscher, N. M., Griffith, D. W. T., Paton-Walsh, C., Jones, N. B., Velazco, V. A., Wilson, S. R., Macatangay, R. C., Kettlewell, G. C., Buchholz, R. R., Riggenbach, M. O., Bukosa, B., John, S. S., Walker, B. T., and Nawaz, H.: TCCON data from Wollongong (AU), Release GGG2020.R0, TCCON Data Archive, hosted by CaltechDATA, https://doi.org/10.14291/tccon.ggg2020.wollongong01.R0, 2023a.

Deutscher, N. M., T., G. D. W., Paton-Walsh, C., Velazco, V. A., Wennberg, P. O., Blavier, J.-F., Washenfelder, R. A., Yavin, Y., Keppel-Aleks, G., and Toon, G. C.: TCCON data from Darwin (AU), Release GGG2020.R0, TCCON Data Archive, hosted by CaltechDATA, https://doi.org/10.14291/tccon.ggg2020.darwin01.R0, 2023b.

di Sarra, A. and Piacentino, S.: ICOS ATC CH4 Release, Lampedusa (8.0 m), 2020-01-30–2021-01-31, ICOS RI, https://hdl.handle.net/11676/PzkyY_L0nMAIej3N_uF0lZ2x, 2021.

di Sarra, A. and Piacentino, S.: ICOS ATC NRT CH4 growing time series, Lampedusa (8.0 m), 2021-02-01–2022-06-15, https://hdl.handle.net/11676/Lcb59V-HlDaQBBWch7_EHjOm, 2022.

Emmenegger, L., Leuenberger, M., and Steinbacher, M.: ICOS ATC CH4 Release, Jungfraujoch (5.0 m), 2016-12-12–2021-01-31, ICOS RI, https://hdl.handle.net/11676/MZbk-o0_pL82MLq5nL9WCD_y, 2021.

Emmenegger, L., Leuenberger, M., and Steinbacher, M.: ICOS ATC NRT CH4 growing time series, Jungfraujoch (5.0 m), 2021-02-01–2022-06-15, ICOS RI, https://hdl.handle.net/11676/C_dRpn8dFl36PmNucz5IY78F, 2022.

Feng, L., Palmer, P. I., Bösch, H., Parker, R. J., Webb, A. J., Correia, C. S. C., Deutscher, N. M., Domingues, L. G., Feist, D. G., Gatti, L. V., Gloor, E., Hase, F., Kivi, R., Liu, Y., Miller, J. B., Morino, I., Sussmann, R., Strong, K., Uchino, O., Wang, J., and Zahn, A.: Consistent regional fluxes of CH$_4$ and CO$_2$ inferred from GOSAT proxy XCH$_4$: XCO$_2$ retrievals, 2010–2014, Atmospheric Chemistry and Physics, 17, 4781–4797, https://doi.org/10.5194/acp-17-4781-2017, publisher: Copernicus GmbH, 2017.

Hase, F., Blumenstock, T., Dohe, S., Groß, J., and Kiel, M.: TCCON data from Karlsruhe, Germany, Release GGG2020R1, TCCON Data Archive, hosted by CaltechDATA, https://doi.org/10.14291/tccon.ggg2020.karlsruhe01.R1, 2022.

Hatakka, J.: ICOS ATC CH4 Release, Pallas (12.0 m), 2017-09-16–2021-01-31, ICOS RI, https://hdl.handle.net/11676/h577rfmSpDWfpejLt2Hk7qNV, 2021.

Hatakka, J.: ICOS ATC NRT CH4 growing time series, Pallas (12.0 m), 2021-02-01–2022-06-15, https://hdl.handle.net/11676/P-vgI_BxTbvlcFA6zjKEy1sc, 2022.

Hatakka, J. and Laurila, T.: ICOS ATC NRT CH4 growing time series, Utö - Baltic sea (57.0 m), 2021-02-01–2022-06-07, https://hdl.handle.net/11676/pHCb4_N1JoBJp5-f3i_12C_3, 2022.

Heliasz, M. and Biermann, T.: ICOS ATC CH4 Release, Hyltemossa (150.0 m), 2017-04-17–2021-01-31, ICOS RI, https://hdl.handle.net/11676/nCSpYgXydmLwofDFfGDwI9kI, 2021.

Heliasz, M. and Biermann, T.: ICOS ATC NRT CH4 growing time series, Hyltemossa (150.0 m), 2021-02-01–2022-06-15, ICOS RI, https://hdl.handle.net/11676/R5EG0Gs5Mnzkq_KaRSr0W6KB, 2022.

Hersbach, H., Bell, B., Berrisford, P., Hirahara, S., Horányi, A., Muñoz-Sabater, J., Nicolas, J., Peubey, C., Radu, R., Schepers, D., Simmons, A., Soci, C., Abdalla, S., Abellan, X., Balsamo, G., Bechtold, P., Biavati, G., Bidlot, J., Bonavita, M., De Chiara, G., Dahlgren, P., Dee, D., Diamantakis, M., Dragani, R., Flemming, J., Forbes, R., Fuentes, M., Geer, A., Haimberger, L., Healy, S., Hogan, R. J., Hólm, E., Janisková, M., Keeley, S., Laloyaux, P., Lopez, P., Lupu, C., Radnoti, G., de Rosnay, P., Rozum, I., Vamborg, F., Villaume, S., and Thépaut, J.-N.: The ERA5 global reanalysis, Quarterly Journal of the Royal Meteorological Society, 146, 1999–2049, https://doi.org/10.1002/qj.3803, _eprint: https://onlinelibrary.wiley.com/doi/pdf/10.1002/qj.3803, 2020.

Houweling, S., Krol, M., Bergamaschi, P., Frankenberg, C., Dlugokencky, E. J., Morino, I., Notholt, J., Sherlock, V., Wunch, D., Beck, V., Gerbig, C., Chen, H., Kort, E. A., Röckmann, T., and Aben, I.: A multi-year methane inversion using SCIAMACHY, accounting for systematic errors using TCCON measurements, Atmos. Chem. Phys., 14, 3991–4012, https://doi.org/10.5194/acp-14-3991-2014, 2014.

Houweling, S., Bergamaschi, P., Chevallier, F., Heimann, M., Kaminski, T., Krol, M., Michalak, A. M., and Patra, P.: Global inverse modeling of CH4 sources and sinks: an overview of methods, Atmos. Chem. Phys., 17, 235–256, https://doi.org/10.5194/acp-17-235-2017, 2017.

Hu, H., Landgraf, J., Detmers, R., Borsdorff, T., Brugh, J. A. d., Aben, I., Butz, A., and Hasekamp, O.: Toward Global Mapping of Methane With TROPOMI: First Results and Intersatellite Comparison to GOSAT, Geophysical Research Letters, 45, 3682–3689, https://doi.org/10.1002/2018GL077259, 2018.

Iraci, L., Podolske, J., Roehl, C., Wennberg, P. O., Blavier, J.-F., Allen, N., Wunch, D., and Osterman, G.: TCCON data from Armstrong Flight Research Center, Edwards, CA, USA, Release GGG2020R0, TCCON Data Archive, hosted by CaltechDATA, https://doi.org/10.14291/tccon.ggg2020.edwards01.R0, 2022.

Ito, A. and Inatomi, M.: Use of a process-based model for assessing the methane budgets of global terrestrial ecosystems and evaluation of uncertainty, Biogeosciences, 9, 759–773, https://doi.org/10.5194/bg-9-759-2012, publisher: Copernicus GmbH, 2012.

Janardanan, R., Maksyutov, S., Tsuruta, A., Wang, F., Tiwari, Y. K., Valsala, V., Ito, A., Yoshida, Y., Kaiser, J. W., Janssens-Maenhout, G., Arshinov, M., Sasakawa, M., Tohjima, Y., Worthy, D. E. J., Dlugokencky, E. J., Ramonet, M., Arduini, J., Lavric, J. V., Piacentino, S., Krummel, P. B., Langenfelds, R. L., Mammarella, I., and Matsunaga, T.: Country-Scale Analysis of Methane Emissions with a High-Resolution Inverse Model Using GOSAT and Surface Observations, Remote Sensing, 12, 375, https://doi.org/10.3390/rs12030375, 2020.

Jöckel, P., Tost, H., Pozzer, A., Brühl, C., Buchholz, J., Ganzeveld, L., Hoor, P., Kerkweg, A., Lawrence, M. n., G, Sander, R., Steil, B., Stiller, G., Tanarhte, M., Taraborrelli, D., Aardenne, J. v., and Lelieveld, J.: The atmospheric chemistry general circulation model ECHAM5/MESSy1: consistent simulation of ozone from the surface to the mesosphere, Atmospheric Chemistry and Physics, 6, 5067–5104, https://doi.org/https://doi.org/10.5194/acp-6-5067-2006, 2006.

Kikuchi, N., Yoshida, Y., Uchino, O., Morino, I., and Yokota, T.: An advanced retrieval algorithm for greenhouse gases using polarization information measured by GOSAT TANSO-FTS SWIR I: Simulation study, Journal of Geophysical Research: Atmospheres, 121, 13,129–13,157, https://doi.org/10.1002/2015JD024720, _eprint: https://onlinelibrary.wiley.com/doi/pdf/10.1002/2015JD024720, 2016.

Kikuchi, N., Kuze, A., Kataoka, F., Shiomi, K., Hashimoto, M., Suto, H., Knuteson, R., Iraci, L., Yates, E., Gore, W., and T., T.: Three-dimensional distribution of greenhouse gas concentrations over megacities observed by GOSAT, 2017.

Kivi, R., Heikkinen, P., and Kyrö, E.: TCCON data from Sodankylä (FI), Release GGG2020.R0, TCCON Data Archive, hosted by Caltech-DATA, https://doi.org/10.14291/tccon.ggg2020.sodankyla01.R0, (2022).

Krol, M., Houweling, S., Bregman, B., Broek, M. v. d., Segers, A., Velthoven, P. v., Peters, W., Dentener, F., and Bergamaschi, P.: The two-way nested global chemistry-transport zoom model TM5: algorithm and applications, Atmospheric Chemistry and Physics, 5, 417–432, https://doi.org/https://doi.org/10.5194/acp-5-417-2005, 2005.

Kubistin, D., Plaß-Dülmer, C., Arnold, S., Lindauer, M., and Müller-Williams, J.: ICOS ATC CH4 Release, Ochsenkopf (163.0 m), 2019-09-25–2021-01-31, ICOS RI, https://hdl.handle.net/11676/nr_e18PX9B47H7WMTC1Jkvwl, 2021a.

Kubistin, D., Plaß-Dülmer, C., Arnold, S., Lindauer, M., and Müller-Williams, J.: ICOS ATC CH4 Release, Steinkimmen (252.0 m), 2019-07-22–2021-01-31, https://hdl.handle.net/11676/ZXLboc_xev65Oi6GV_ZhMpHx, 2021b.

Kubistin, D., Plaß-Dülmer, C., Arnold, S., Lindauer, M., Müller-Williams, J., and Schumacher, M.: ICOS ATC CH4 Release, Gartow (341.0 m), 2016-05-10–2021-01-31, ICOS RI, https://hdl.handle.net/11676/85z4jUGIi3yBRrLezBZVHlvS, 2021c.

Kubistin, D., Plaß-Dülmer, C., Arnold, S., Lindauer, M., Müller-Williams, J., and Schumacher, M.: ICOS ATC CH4 Release, Hohenpeissenberg (131.0 m), 2015-09-18–2021-01-31, ICOS RI, https://hdl.handle.net/11676/OXmIfWQJAYjuVSw71jZsqQs1, 2021d.

Kubistin, D., Plaß-Dülmer, C., Arnold, S., Lindauer, M., Müller-Williams, J., and Schumacher, M.: ICOS ATC CH4 Release, Karlsruhe (200.0 m), 2016-12-16–2021-01-31, ICOS RI, https://hdl.handle.net/11676/g9fAzD7XoLLhRgR_S8EvTFcl, 2021e.

Kubistin, D., Plaß-Dülmer, C., Arnold, S., Lindauer, M., Müller-Williams, J., and Schumacher, M.: ICOS ATC CH4 Release, Lindenberg (98.0 m), 2015-10-08–2021-01-31, https://hdl.handle.net/11676/49Q4QH1NidkRFbum15bbi365, 2021f.

Kubistin, D., Plaß-Dülmer, C., Arnold, S., Lindauer, M., Müller-Williams, J., and Schumacher, M.: ICOS ATC CH4 Release, Torfhaus (147.0 m), 2017-12-12–2021-01-31, https://hdl.handle.net/11676/RwwZxIKrEZ-hO9eoxAmIjBbD, 2021g.

Kubistin, D., Plaß-Dülmer, C., Kneuer, T., Lindauer, M., and Müller-Williams, J.: ICOS ATC NRT CH4 growing time series, Gartow (341.0 m), 2021-02-01–2022-06-15, ICOS RI, https://hdl.handle.net/11676/lCLaCxBfQZqDW8QRRljRcqxN, 2022a.

Kubistin, D., Plaß-Dülmer, C., Kneuer, T., Lindauer, M., and Müller-Williams, J.: ICOS ATC NRT CH4 growing time series, Hohenpeissenberg (131.0 m), 2021-02-01–2022-06-15, ICOS RI, https://hdl.handle.net/11676/e9UaT8vS1WD1Y2qMdrTRsBvQ, 2022b.

Kubistin, D., Plaß-Dülmer, C., Kneuer, T., Lindauer, M., and Müller-Williams, J.: ICOS ATC NRT CH4 growing time series, Karlsruhe (200.0 m), 2021-02-01–2022-06-15, ICOS RI, https://hdl.handle.net/11676/oA0Te3Iu4LnZQkjOgCIHd93V, 2022c.

Kubistin, D., Plaß-Dülmer, C., Kneuer, T., Lindauer, M., and Müller-Williams, J.: ICOS ATC NRT CH4 growing time series, Lindenberg (98.0 m), 2021-02-01–2022-05-19, https://hdl.handle.net/11676/RXKHh88ShVoWZnarmAqQfpeu, 2022d.

Kubistin, D., Plaß-Dülmer, C., Kneuer, T., Lindauer, M., and Müller-Williams, J.: ICOS ATC NRT CH4 growing time series, Ochsenkopf (163.0 m), 2021-02-01–2022-06-15, https://hdl.handle.net/11676/mkRrUwnZ2992tOa6MWLpzcxk, 2022e.

Kubistin, D., Plaß-Dülmer, C., Kneuer, T., Lindauer, M., and Müller-Williams, J.: ICOS ATC NRT CH4 growing time series, Steinkimmen (252.0 m), 2021-02-01–2022-06-15, https://hdl.handle.net/11676/GsTqtsqmBiHRyy1gc9W1-8g6, 2022f.

Kubistin, D., Plaß-Dülmer, C., Kneuer, T., Lindauer, M., and Müller-Williams, J.: ICOS ATC NRT CH4 growing time series, Torfhaus (147.0 m), 2021-02-01–2022-06-15, https://hdl.handle.net/11676/8wvK2gNS3bWtjiOELhBf4fq-, 2022g.

Kuze, A., Suto, H., Nakajima, M., and Hamazaki, T.: Thermal and near infrared sensor for carbon observation Fourier-transform spectrometer on the Greenhouse Gases Observing Satellite for greenhouse gases monitoring, Applied Optics, 48, 6716–6733, https://doi.org/10.1364/AO.48.006716, publisher: Optica Publishing Group, 2009.

Kuze, A., Kikuchi, N., Kataoka, F., Suto, H., Shiomi, K., and Kondo, Y.: Detection of Methane Emission from a Local Source Using GOSAT Target Observations, Remote Sensing, 12, 267, https://doi.org/10.3390/rs12020267, number: 2 Publisher: Multidisciplinary Digital Publishing Institute, 2020.

Kuze, A., Nakamura, Y., Oda, T., Yoshida, J., Kikuchi, N., Kataoka, F., Suto, H., and Shiomi, K.: Examining partial-column density retrieval of lower-tropospheric CO2 from GOSAT target observations over global megacities, Remote Sensing of Environment, 273, 112 966, https://doi.org/10.1016/j.rse.2022.112966, 2022.

Laughner, J. L., Roche, S., Kiel, M., Toon, G. C., Wunch, D., Baier, B. C., Biraud, S., Chen, H., Kivi, R., Laemmel, T., McKain, K., Quéhé, P.-Y., Rousogenous, C., Stephens, B. B., Walker, K., and Wennberg, P. O.: A new algorithm to generate a priori trace gas profiles for the GGG2020 retrieval algorithm, Atmospheric Measurement Techniques, 16, 1121–1146, https://doi.org/10.5194/amt-16-1121-2023, publisher: Copernicus GmbH, 2023.

Laughner, J. L., Toon, G. C., Mendonca, J., Petri, C., Roche, S., Wunch, D., Blavier, J.-F., Griffith, D. W. T., Heikkinen, P., Keeling, R. F., Kiel, M., Kivi, R., Roehl, C. M., Stephens, B. B., Baier, B. C., Chen, H., Choi, Y., Deutscher, N. M., DiGangi, J. P., Gross, J., Herkommer, B., Jeseck, P., Laemmel, T., Lan, X., McGee, E., McKain, K., Miller, J., Morino, I., Notholt, J., Ohyama, H., Pollard, D. F., Rettinger, M., Riris, H., Rousogenous, C., Sha, M. K., Shiomi, K., Strong, K., Sussmann, R., Té, Y., Velazco, V. A., Wofsy, S. C., Zhou, M., and Wennberg, P. O.: The Total Carbon Column Observing Network's GGG2020 data version, Earth System Science Data, 16, 2197–2260, https://doi.org/10.5194/essd-16-2197-2024, publisher: Copernicus GmbH, 2024.

Laurila, T.: ICOS ATC CH4 Release, Utö - Baltic sea (57.0 m), 2018-03-09–2021-01-31, https://hdl.handle.net/11676/m67T4icmvChEfpzz-WOCH4FB, 2021.

Lehner, I. and Mölder, M.: ICOS ATC CH4 Release, Norunda (100.0 m), 2017-04-01–2021-01-31, ICOS RI, https://hdl.handle.net/11676/72caSykeioIBmay4oj_jg6ef, 2021.

Lehner, I. and Mölder, M.: ICOS ATC NRT CH4 growing time series, Norunda (100.0 m), 2021-02-01–2022-06-15, https://hdl.handle.net/11676/jDEkWtCTKIEfatUrYPEI38zU, 2022.

Lehtinen, K. and Leskinen, A.: ICOS ATC NRT CH4 growing time series, Puijo (84.0 m), 2021-02-01–2022-06-15, https://hdl.handle.net/11676/4fXabObsAtISq7sui39JCOHp, 2022.

Levula, J. and Mammarella, I.: ICOS ATC CH4 Release, Hyytiälä (125.0 m), 2016-12-13–2021-01-31, https://hdl.handle.net/11676/6uV8wu8tklBtc6kLGSQc_zzG, 2021.

Lienert, S. and Joos, F.: A Bayesian ensemble data assimilation to constrain model parameters and land-use carbon emissions, Biogeosciences, 15, 2909–2930, https://doi.org/https://doi.org/10.5194/bg-15-2909-2018, publisher: Copernicus GmbH, 2018.

Lindqvist, H., Kivimäki, E., Häkkilä, T., Tsuruta, A., Schneising, O., Buchwitz, M., Lorente, A., Martinez Velarte, M., Borsdorff, T., Alberti, C., Backman, L., Buschmann, M., Chen, H., Dubravica, D., Hase, F., Heikkinen, P., Karppinen, T., Kivi, R., McGee, E., Notholt, J., Rautiainen, K., Roche, S., Simpson, W., Strong, K., Tu, Q., Wunch, D., Aalto, T., and Tamminen, J.: Evaluation of Sentinel-5P TROPOMI Methane Observations at Northern High Latitudes, Remote Sensing, 16, 2979, https://doi.org/10.3390/rs16162979, number: 16 Publisher: Multidisciplinary Digital Publishing Institute, 2024.

Liu, C., Wang, W., Sun, Y., and Shan, C.: TCCON data from Hefei, China, Release GGG2020R1, TCCON Data Archive, hosted by CaltechDATA, https://doi.org/10.14291/tccon.ggg2020.hefei01.R1, 2023.

Lu, X., Jacob, D. J., Zhang, Y., Maasakkers, J. D., Sulprizio, M. P., Shen, L., Qu, Z., Scarpelli, T. R., Nesser, H., Yantosca, R. M., Sheng, J., Andrews, A., Parker, R. J., Boesch, H., Bloom, A. A., and Ma, S.: Global methane budget and trend, 2010–2017: complementarity of inverse analyses using in situ (GLOBALVIEWplus CH4 ObsPack) and satellite (GOSAT) observations, Atmospheric Chemistry and Physics, 21, 4637–4657, https://doi.org/10.5194/acp-21-4637-2021, publisher: Copernicus GmbH, 2021.

Lu, X., Jacob, D. J., Wang, H., Maasakkers, J. D., Zhang, Y., Scarpelli, T. R., Shen, L., Qu, Z., Sulprizio, M. P., Nesser, H., Bloom, A. A., Ma, S., Worden, J. R., Fan, S., Parker, R. J., Boesch, H., Gautam, R., Gordon, D., Moran, M. D., Reuland, F., Villasana, C. A. O., and Andrews, A.: Methane emissions in the United States, Canada, and Mexico: evaluation of national methane emission inventories and 2010–2017 sectoral trends by inverse analysis of in situ (GLOBALVIEWplus CH4 ObsPack) and satellite (GOSAT) atmospheric observations, Atmospheric Chemistry and Physics, 22, 395–418, https://doi.org/10.5194/acp-22-395-2022, publisher: Copernicus GmbH, 2022.

Lund Myhre, C., Platt, S. M., Hermansen, O., and Lunder, C.: ICOS ATC CH4 Release, Zeppelin (15.0 m), 2017-07-27–2021-01-31, https://hdl.handle.net/11676/WREaChiXhVOYRtgEvmayh6qy, 2021.

Lund Myhre, C., Platt, S. M., Hermansen, O., and Lunder, C.: ICOS ATC NRT CH4 growing time series, Zeppelin (15.0 m), 2021-02-01–2022-06-15, ICOS RI, https://hdl.handle.net/11676/psuTYT5n-Erxok0yC95KBZR8, 2022.

Lunt, M. F., Palmer, P. I., Feng, L., Taylor, C. M., Boesch, H., and Parker, R. J.: An increase in methane emissions from tropical Africa between 2010 and 2016 inferred from satellite data, Atmospheric Chemistry and Physics, 19, 14 721–14 740, https://doi.org/https://doi.org/10.5194/acp-19-14721-2019, 2019.

Maasakkers, J. D., Jacob, D. J., Sulprizio, M. P., Scarpelli, T. R., Nesser, H., Sheng, J., Zhang, Y., Lu, X., Bloom, A. A., Bowman, K. W., Worden, J. R., and Parker, R. J.: 2010–2015 North American methane emissions, sectoral contributions, and trends: a high-resolution inversion of GOSAT observations of atmospheric methane, Atmospheric Chemistry and Physics, 21, 4339–4356, https://doi.org/10.5194/acp-21-4339-2021, publisher: Copernicus GmbH, 2021.

Maasakkers, J. D., McDuffie, E. E., Sulprizio, M. P., Chen, C., Schultz, M., Brunelle, L., Thrush, R., Steller, J., Sherry, C., Jacob, D. J., Jeong, S., Irving, B., and Weitz, M.: A Gridded Inventory of Annual 2012–2018 U.S. Anthropogenic Methane Emissions, Environmental Science & Technology, 57, 16 276–16 288, https://doi.org/10.1021/acs.est.3c05138, publisher: American Chemical Society, 2023.

765 Mammarella, I.: ICOS ATC NRT CH4 growing time series, Hyytiälä (125.0 m), 2021-02-01–2022-06-15, https://hdl.handle.net/11676/VuONT1fz-6s9ZQzFDkACXtFP, 2022.

Manca, G.: ICOS ATC NRT CH4 growing time series, Ispra (100.0 m), 2021-02-01–2022-06-15, ICOS RI, https://hdl.handle.net/11676/cHJ-nc_oYmMTZ9gC6H7LSyOk, 2022.

Marek, M. V., Vítková, G., and Komínková, K.: ICOS ATC CH4 Release, Křešín u Pacova (250.0 m), 2017-04-12–2021-01-31, ICOS RI,
770   https://hdl.handle.net/11676/qogTS9guy2qFfbjL2FrCxhCY, 2021.

Marek, M. V., Vítková, G., and Komínková, K.: ICOS ATC NRT CH4 growing time series, Křešín u Pacova (250.0 m), 2021-02-01–2022-06-08, ICOS RI, https://hdl.handle.net/11676/RBvDN0k9ioAgfwp817ux-7va, 2022.

Marklund, P., Ottosson-Löfvenius, M., and Smith, P.: ICOS ATC CH4 Release, Svartberget (150.0 m), 2017-06-01–2021-01-31, https://hdl.handle.net/11676/9IolaaKKhPEn2egf2JZ0Sd9L, 2021.

775 McNorton, J., Wilson, C., Gloor, M., Parker, R. J., Boesch, H., Feng, W., Hossaini, R., and Chipperfield, M. P.: Attribution of recent increases in atmospheric methane through 3-D inverse modelling, Atmospheric Chemistry and Physics, 18, 18 149–18 168, https://doi.org/10.5194/acp-18-18149-2018, publisher: Copernicus GmbH, 2018.

Miller, S. M., Wofsy, S. C., Michalak, A. M., Kort, E. A., Andrews, A. E., Biraud, S. C., Dlugokencky, E. J., Eluszkiewicz, J., Fischer, M. L., Janssens-Maenhout, G., Miller, B. R., Miller, J. B., Montzka, S. A., Nehrkorn, T., and Sweeney, C.: Anthropogenic emissions of methane
780   in the United States, Proceedings of the National Academy of Sciences, 110, 20 018–20 022, https://doi.org/10.1073/pnas.1314392110, publisher: Proceedings of the National Academy of Sciences, 2013.

Morino, I., Ohyama, H., Hori, A., and Ikegami, H.: TCCON data from Rikubetsu, Hokkaido, Japan, Release GGG2020R0, TCCON Data Archive, hosted by CaltechDATA, https://doi.org/10.14291/tccon.ggg2020.rikubetsu01.R0, 2022a.

Morino, I., Ohyama, H., Hori, A., and Ikegami, H.: TCCON data from Tsukuba, Ibaraki, Japan, 125HR, Release GGG2020R0, TCCON Data
785   Archive, hosted by CaltechDATA, https://doi.org/10.14291/tccon.ggg2020.tsukuba02.R0, 2022b.

Morino, I., Velazco, V. A., Hori, A., Uchino, O., , and Griffith, D. W. T.: TCCON data from Burgos, Philippines, Release GGG2020R0, TCCON Data Archive, hosted by CaltechDATA, https://doi.org/10.14291/tccon.ggg2020.burgos01.R0, 2022c.

Notholt, J., Petri, C., Warneke, T., Deutscher, N., Buschmann, M., Weinzierl, C., Macatangay, R., and Grupe, P.: TCCON data from Bremen, Germany, Release GGG2020R0, TCCON Data Archive, hosted by CaltechDATA, https://doi.org/10.14291/tccon.ggg2020.bremen01.R0,
790   2022.

Palmer, P. I., Feng, L., Lunt, M. F., Parker, R. J., Bösch, H., Lan, X., Lorente, A., and Borsdorff, T.: The added value of satellite observations of methane for understanding the contemporary methane budget, Philosophical Transactions of the Royal Society A: Mathematical, Physical and Engineering Sciences, 379, 20210 106, https://doi.org/10.1098/rsta.2021.0106, publisher: Royal Society, 2021.

Pandey, S., Houweling, S., Krol, M., Aben, I., Chevallier, F., Dlugokencky, E. J., Gatti, L. V., Gloor, E., Miller, J. B., Detmers, R., Machida, T.,
795   and Röckmann, T.: Inverse modeling of GOSAT-retrieved ratios of total column CH_4 and CO_2 for 2009 and 2010, Atmospheric Chemistry and Physics, 16, 5043–5062, https://doi.org/10.5194/acp-16-5043-2016, 2016.

Pandey, S., Houweling, S., Lorente, A., Borsdorff, T., Tsivlidou, M., Bloom, A. A., Poulter, B., Zhang, Z., and Aben, I.: Using satellite data to identify the methane emission controls of South Sudan's wetlands, Biogeosciences, 18, 557–572, https://doi.org/https://doi.org/10.5194/bg-18-557-2021, publisher: Copernicus GmbH, 2021.

800 Patra, P. K., Houweling, S., Krol, M., Bousquet, P., Belikov, D., Bergmann, D., Bian, H., Cameron-Smith, P., Chipperfield, M. P., Corbin, K., Fortems-Cheiney, A., Fraser, A., Gloor, E., Hess, P., Ito, A., Kawa, S. R., Law, R. M., Loh, Z., Maksyutov, S., Meng, L., Palmer, P. I., Prinn, R. G., Rigby, M., Saito, R., and Wilson, C.: TransCom model simulations of CH_4 and related species: linking transport, surface flux and chemical loss with CH_4 variability in the troposphere and lower stratosphere, Atmospheric Chemistry and Physics, 11, 12 813–12 837, https://doi.org/https://doi.org/10.5194/acp-11-12813-2011, 2011.

805 Peters, W., Miller, J. B., Whitaker, J., Denning, A. S., Hirsch, A., Krol, M. C., Zupanski, D., Bruhwiler, L., and Tans, P. P.: An ensemble data assimilation system to estimate CO2 surface fluxes from atmospheric trace gas observations, J. Geophys. Res., 110, D24 304, https://doi.org/10.1029/2005JD006157, 2005.

Peters, W., Jacobson, A. R., Sweeney, C., Andrews, A. E., Conway, T. J., Masarie, K., Miller, J. B., Bruhwiler, L. M., Pétron, G., Hirsch, A. I., and others: An atmospheric perspective on North American carbon dioxide exchange: CarbonTracker, Proceedings of the National
810 Academy of Sciences, 104, 18 925–18 930, http://www.pnas.org/content/104/48/18925.short, 2007.

Petrescu, A. M. R., Peters, G. P., Engelen, R., Houweling, S., Brunner, D., Tsuruta, A., Matthews, B., Patra, P. K., Belikov, D., Thompson, R. L., Höglund-Isaksson, L., Zhang, W., Segers, A. J., Etiope, G., Ciotoli, G., Peylin, P., Chevallier, F., Aalto, T., Andrew, R. M., Bastviken, D., Berchet, A., Broquet, G., Conchedda, G., Dellaert, S. N. C., Denier van der Gon, H., Gütschow, J., Haussaire, J.-M., Lauerwald, R., Markkanen, T., van Peet, J. C. A., Pison, I., Regnier, P., Solum, E., Scholze, M., Tenkanen, M., Tubiello, F. N., van der Werf, G. R., and
815 Worden, J. R.: Comparison of observation- and inventory-based methane emissions for eight large global emitters, Earth System Science Data, 16, 4325–4350, https://doi.org/10.5194/essd-16-4325-2024, publisher: Copernicus GmbH, 2024.

Petri, C., Vrekoussis, M., Rousogenous, C., Warneke, T., Sciare, J., and Notholt, J.: TCCON data from Nicosia, Cyprus, Release GGG2020R1, TCCON Data Archive, hosted by CaltechDATA, https://doi.org/10.14291/tccon.ggg2020.nicosia01.R1, 2023.

Plumb, R. A.: Tracer interrelationships in the stratosphere, Reviews of Geophysics, 45, RG4005, https://doi.org/10.1029/2005RG000179,
820 2007.

Qu, Z., Jacob, D. J., Shen, L., Lu, X., Zhang, Y., Scarpelli, T. R., Nesser, H., Sulprizio, M. P., Maasakkers, J. D., Bloom, A. A., Worden, J. R., Parker, R. J., and Delgado, A. L.: Global distribution of methane emissions: a comparative inverse analysis of observations from the TROPOMI and GOSAT satellite instruments, Atmospheric Chemistry and Physics, 21, 14 159–14 175, https://doi.org/10.5194/acp-21-14159-2021, publisher: Copernicus GmbH, 2021.

825 Ramonet, M. and Delmotte, M.: ICOS ATC CH4 Release, Saclay (100.0 m), 2017-05-31–2021-01-31, https://hdl.handle.net/11676/tby5exW6sb3SpUFw8d2LAfAT, 2021.

Ramonet, M., Conil, S., Delmotte, M., and Laurent, O.: ICOS ATC CH4 Release, Observatoire pérenne de l'environnement (120.0 m), 2016-08-18–2021-01-31, ICOS RI, https://hdl.handle.net/11676/-3E3iS_JKMPC5z2qtYFISw0O, 2021a.

Ramonet, M., Lopez, M., and Delmotte, M.: ICOS ATC CH4 Release, Trainou (180.0 m), 2016-08-11–2021-01-31, https://hdl.handle.net/
830 11676/J7l4KC07faI_41j4r1kxO8ds, 2021b.

Ramonet, M., Conil, S., Delmotte, M., Laurent, O., and Lopez, M.: ICOS ATC NRT CH4 growing time series, Observatoire pérenne de l'environnement (120.0 m), 2021-02-01–2022-06-14, https://hdl.handle.net/11676/CzLoQ5NMfAKB5TSN7gx6DPDC, 2022a.

Ramonet, M., Delmotte, M., and Lopez, M.: ICOS ATC NRT CH4 growing time series, Saclay (100.0 m), 2021-02-01–2022-06-15, https://hdl.handle.net/11676/whLQq_OniolcFJofjCtYsY3P, 2022b.

835 Ramonet, M., Lopez, M., and Delmotte, M.: ICOS ATC NRT CH4 growing time series, Trainou (180.0 m), 2021-02-01–2022-06-15, https://hdl.handle.net/11676/sw_v15a-Bqmm_lB4aEjU0kVe, 2022c.

Rodgers, C. D. and Connor, B. J.: Intercomparison of remote sounding instruments: INTERCOMPARISON OF REMOTE SOUNDERS, Journal of Geophysical Research: Atmospheres, 108, n/a–n/a, https://doi.org/10.1029/2002JD002299, 2003.

Saad, K. M., Wunch, D., Toon, G. C., Bernath, P., Boone, C., Connor, B., Deutscher, N. M., Griffith, D. W. T., Kivi, R., Notholt, J., Roehl, C., Schneider, M., Sherlock, V., and Wennberg, P. O.: Derivation of tropospheric methane from TCCON CH4 and HF total column observations, Atmospheric Measurement Techniques, 7, 2907–2918, https://doi.org/10.5194/amt-7-2907-2014, 2014.

Saito, R., Patra, P. K., Sweeney, C., Machida, T., Krol, M., Houweling, S., Bousquet, P., Agusti-Panareda, A., Belikov, D., Bergmann, D., Bian, H., Cameron-Smith, P., Chipperfield, M. P., Fortems-Cheiney, A., Fraser, A., Gatti, L. V., Gloor, E., Hess, P., Kawa, S. R., Law, R. M., Locatelli, R., Loh, Z., Maksyutov, S., Meng, L., Miller, J. B., Palmer, P. I., Prinn, R. G., Rigby, M., and Wilson, C.: TransCom model simulations of methane: Comparison of vertical profiles with aircraft measurements, Journal of Geophysical Research: Atmospheres, 118, 3891–3904, https://doi.org/https://doi.org/10.1002/jgrd.50380, _eprint: https://agupubs.onlinelibrary.wiley.com/doi/pdf/10.1002/jgrd.50380, 2013.

Saunois, M., Stavert, A. R., Poulter, B., Bousquet, P., Canadell, J. G., Jackson, R. B., Raymond, P. A., Dlugokencky, E. J., Houweling, S., Patra, P. K., Ciais, P., Arora, V. K., Bastviken, D., Bergamaschi, P., Blake, D. R., Brailsford, G., Bruhwiler, L., Carlson, K. M., Carrol, M., Castaldi, S., Chandra, N., Crevoisier, C., Crill, P. M., Covey, K., Curry, C. L., Etiope, G., Frankenberg, C., Gedney, N., Hegglin, M. I., Höglund-Isaksson, L., Hugelius, G., Ishizawa, M., Ito, A., Janssens-Maenhout, G., Jensen, K. M., Joos, F., Kleinen, T., Krummel, P. B., Langenfelds, R. L., Laruelle, G. G., Liu, L., Machida, T., Maksyutov, S., McDonald, K. C., McNorton, J., Miller, P. A., Melton, J. R., Morino, I., Müller, J., Murguia-Flores, F., Naik, V., Niwa, Y., Noce, S., O'Doherty, S., Parker, R. J., Peng, C., Peng, S., Peters, G. P., Prigent, C., Prinn, R., Ramonet, M., Regnier, P., Riley, W. J., Rosentreter, J. A., Segers, A., Simpson, I. J., Shi, H., Smith, S. J., Steele, L. P., Thornton, B. F., Tian, H., Tohjima, Y., Tubiello, F. N., Tsuruta, A., Viovy, N., Voulgarakis, A., Weber, T. S., van Weele, M., van der Werf, G. R., Weiss, R. F., Worthy, D., Wunch, D., Yin, Y., Yoshida, Y., Zhang, W., Zhang, Z., Zhao, Y., Zheng, B., Zhu, Q., Zhu, Q., and Zhuang, Q.: The Global Methane Budget 2000–2017, Earth System Science Data, 12, 1561–1623, https://doi.org/10.5194/essd-12-1561-2020, publisher: Copernicus GmbH, 2020.

Saunois, M., Martinez, A., Poulter, B., Zhang, Z., Raymond, P., Regnier, P., Canadell, J. G., Jackson, R. B., Patra, P. K., Bousquet, P., Ciais, P., Dlugokencky, E. J., Lan, X., Allen, G. H., Bastviken, D., Beerling, D. J., Belikov, D. A., Blake, D. R., Castaldi, S., Crippa, M., Deemer, B. R., Dennison, F., Etiope, G., Gedney, N., Höglund-Isaksson, L., Holgerson, M. A., Hopcroft, P. O., Hugelius, G., Ito, A., Jain, A. K., Janardanan, R., Johnson, M. S., Kleinen, T., Krummel, P., Lauerwald, R., Li, T., Liu, X., McDonald, K. C., Melton, J. R., Mühle, J., Müller, J., Murguia-Flores, F., Niwa, Y., Noce, S., Pan, S., Parker, R. J., Peng, C., Ramonet, M., Riley, W. J., Rocher-Ros, G., Rosentreter, J. A., Sasakawa, M., Segers, A., Smith, S. J., Stanley, E. H., Thanwerdas, J., Tian, H., Tsuruta, A., Tubiello, F. N., Weber, T. S., van der Werf, G., Worthy, D. E., Xi, Y., Yoshida, Y., Zhang, W., Zheng, B., Zhu, Q., Zhu, Q., and Zhuang, Q.: Global Methane Budget 2000–2020, Earth System Science Data Discussions, pp. 1–147, https://doi.org/10.5194/essd-2024-115, publisher: Copernicus GmbH, 2024.

Schuldt, K. N., Aalto, T., Andrews, A., Aoki, S., Arduini, J., Baier, B., Bergamaschi, P., Biermann, T., Biraud, S. C., Boenisch, H., Brailsford, G., Chen, H., Colomb, A., Conil, S., Cristofanelli, P., Cuevas, E., Daube, B., Davis, K., Mazière, M. D., Delmotte, M., Desai, A., DiGangi, J. P., Dlugokencky, E., Elkins, J. W., Emmenegger, L., Fischer, M. L., Gatti, L. V., Gehrlein, T., Gerbig, C., Gloor, E., Goto, D., Haszpra, L., Hatakka, J., Heimann, M., Heliasz, M., Hermanssen, O., Hintsa, E., Holst, J., Ivakhov, V., Jaffe, D., Joubert, W., Kang, H.-Y., Karion, A., Kazan, V., Keronen, P., Ko, M.-Y., Kominkova, K., Kort, E., Kozlova, E., Krummel, P., Kubistin, D., Labuschagne, C., Langenfelds, R., Laurent, O., Laurila, T., Lauvaux, T., Lee, J., Lee, H., Lee, C.-H., Lehner, I., Leppert, R., Leuenberger, M., Lindauer, M., Loh, Z., Lopez, M., Machida, T., Mammarella, I., Manca, G., Marek, M. V., Martin, M. Y., Matsueda, H., McKain, K., Miles, N., Miller, C. E., Miller, J. B., Moore, F., Morimoto, S., Munro, D., Myhre, C. L., Mölder, M., Müller-Williams, J., Nichol, S., Niwa, Y., O'Doherty, S.,

875   Obersteiner, F., Piacentino, S., Pichon, J. M., Pittman, J., Plass-Duelmer, C., Ramonet, M., Richardson, S., Rivas, P. P., Saito, K., Santoni,
G., Sasakawa, M., Scheeren, B., Schuck, T., Schumacher, M., Seifert, T., Sha, M. K., Shepson, P., Sloop, C. D., Smith, P., Steinbacher,
M., Stephens, B., Sweeney, C., Timas, H., Torn, M., Trisolino, P., Turnbull, J., Tørseth, K., Viner, B., Vitkova, G., Watson, A., Wofsy,
S., Worsey, J., Worthy, D., Zahn, A., and Sarra, A. G. d.: Multi-laboratory compilation of atmospheric carbon dioxide data for the period
1983-2020; obspack_ch4_1_GLOBALVIEWplus_v4.0_2021-10-14, https://doi.org/10.25925/20211001, 2021.

880   Schuldt, K. N., Aalto, T., Andrews, A., Apadula, F., Arduini, J., Arnold, S., Baier, B., Bartyzel, J., Bergamaschi, P., Biermann, T., Biraud,
S. C., Blanc, P.-E., Boenisch, H., Brailsford, G., Brand, W. A., Brunner, D., Bui, T. P., Bäni, L., Calzolari, F., Chang, C. S., Chen, H.,
Chmura, L., Climadat, S., Colomb, A., Condori, L., Conen, F., Conil, S., Couret, C., Cristofanelli, P., Cuevas, E., Curcoll, R., Daube,
B., Davis, K. J., De Mazière, M., Dean-Day, J. M., Della Coletta, J., Delmotte, M., Desai, A., Di Iorio, T., DiGangi, J. P., DiGangi, E.,
Elkins, J. W., Elsasser, M., Emmenegger, L., Fischer, M. L., Forster, G., Frumau, A., Fuente-Lastra, M., Galkowski, M., Gatti, L. V.,
885   Gehrlein, T., Gerbig, C., Gheusi, F., Gloor, E., Goto, D., Hammer, S., Hanisco, T. F., Haszpra, L., Hatakka, J., Heimann, M., Heliasz,
M., Heltai, D., Henne, S., Hensen, A., Hermans, C., Hermansen, O., Hintsa, E., Hoheisel, A., Holst, J., Iraci, L. T., Ivakhov, V., Jaffe,
D. A., Jordan, A., Joubert, W., Kang, H.-Y., Karion, A., Kazan, V., Keeling, R. F., Keronen, P., Kers, B., Kim, J., Klausen, J., Kneuer, T.,
Ko, M.-Y., Kolari, P., Kominkova, K., Kort, E., Kozlova, E., Krummel, P. B., Kubistin, D., Kulawik, S. S., Kumps, N., Labuschagne, C.,
Lan, X., Langenfelds, R. L., Lanza, A., Laurent, O., Laurila, T., Lauvaux, T., Lavric, J., Lee, H., Lee, J., Lee, C.-H., Lehner, I., Lehtinen,
890   K., Leppert, R., Leskinen, A., Leuenberger, M., Levin, I., Levula, J., Lindauer, M., Lindroth, A., Loh, Z. M., Lopez, M., Lowry, D.,
Lunder, C. R., Löfvenius, M. O., Machida, T., Mammarella, I., Manca, G., Manning, A., Marek, M. V., Marklund, P., Marrero, J. E.,
Martin, D., Martin, M. Y., Martins, G. A., Matsueda, H., McKain, K., Meinhardt, F., Menoud, M., Metzger, J.-M., Miles, N. L., Miller,
J. B., Miller, C. E., Monteiro, V., Montzka, S., Moore, F., Moossen, H., Morgan, E., Morgui, J.-A., Morimoto, S., Munro, D., Mutuku,
M., Myhre, C. L., Mölder, M., Müller-Williams, J., Necki, J., Nichol, S., Nisbet, E., Niwa, Y., Njiru, D. M., Noe, S. M., O'Doherty,
895   S., Obersteiner, F., Parworth, C. L., Peltola, O., Peters, W., Philippon, C., Piacentino, S., Pichon, J. M., Pickers, P., Pitt, J., Pittman, J.,
Plass-Dülmer, C., Platt, S. M., Popa, M. E., Prinzivalli, S., Ramonet, M., Richardson, S. J., Rigouleau, L.-J., Rivas, P. P., Rothe, M.,
Roulet, Y.-A., Ryoo, J.-M., Röckmann, T., Santoni, G., Sasakawa, M., Scheeren, B., Schmidt, M., Schuck, T., Schumacher, M., Seifert,
T., Sha, M. K., Shepson, P., Sloop, C. D., Smith, P. D., Spain, G., St. Clair, J. M., Steger, D., Steinbacher, M., Stephens, B., Sweeney,
C., Sørensen, L. L., Taipale, R., Takatsuji, S., Thoning, K., Timas, H., Torn, M., Trisolino, P., Turnbull, J., Vermeulen, A., Vimont, I.,
900   Viner, B., Vitkova, G., Watson, A., Weiss, R., Weyrauch, D., Wofsy, S. C., Worsey, J., Worthy, D., Xueref-Remy, I., Yates, E. L., Young,
D., Yver-Kwok, C., Zaehle, S., Zahn, A., Zazzeri, G., Zellweger, C., Zimnoch, M., de Souza, R. A., de Vries, M., di Sarra, A. G., van
Dinther, D., van den Bulk, P., and van der Veen, C.: Multi-laboratory compilation of atmospheric methane data for the period 1983-2022;
obspack_ch4_1_GLOBALVIEWplus_v6.0_2023-12-01, https://doi.org/10.25925/20231001, 2023.

Sha, M. K., Langerock, B., Blavier, J.-F. L., Blumenstock, T., Borsdorff, T., Buschmann, M., Dehn, A., De Mazière, M., Deutscher, N. M.,
905   Feist, D. G., García, O. E., Griffith, D. W. T., Grutter, M., Hannigan, J. W., Hase, F., Heikkinen, P., Hermans, C., Iraci, L. T., Jeseck,
P., Jones, N., Kivi, R., Kumps, N., Landgraf, J., Lorente, A., Mahieu, E., Makarova, M. V., Mellqvist, J., Metzger, J.-M., Morino, I.,
Nagahama, T., Notholt, J., Ohyama, H., Ortega, I., Palm, M., Petri, C., Pollard, D. F., Rettinger, M., Robinson, J., Roche, S., Roehl, C. M.,
Röhling, A. N., Rousogenous, C., Schneider, M., Shiomi, K., Smale, D., Stremme, W., Strong, K., Sussmann, R., Té, Y., Uchino, O.,
Velazco, V. A., Vigouroux, C., Vrekoussis, M., Wang, P., Warneke, T., Wizenberg, T., Wunch, D., Yamanouchi, S., Yang, Y., and Zhou,
910   M.: Validation of methane and carbon monoxide from Sentinel-5 Precursor using TCCON and NDACC-IRWG stations, Atmospheric
Measurement Techniques, 14, 6249–6304, https://doi.org/10.5194/amt-14-6249-2021, publisher: Copernicus GmbH, 2021.

Sherlock, V., Connor, B., Robinson, J., Shiona, H., Smale, D., and Pollard, D.: TCCON data from Lauder, New Zealand, 125HR, Release GGG2020R0, TCCON Data Archive, hosted by CaltechDATA, https://doi.org/10.14291/tccon.ggg2020.lauder02.R0, 2022.

Shiomi, K., Kawakami, S., Ohyama, H., Arai, K., Okumura, H., Ikegami, H., and Usami, M.: TCCON data from Saga, Japan, Release GGG2020R0, TCCON Data Archive, hosted by CaltechDATA, https://doi.org/10.14291/tccon.ggg2020.saga01.R0, 2022.

Smith, P. and Marklund, P.: ICOS ATC NRT CH4 growing time series, Svartberget (150.0 m), 2021-02-01–2022-05-29, https://hdl.handle.net/11676/hlTT_WCS6jyiZLE-Q2x9Bbh1, 2022.

Spivakovsky, C. M., Logan, J. A., Montzka, S. A., Balkanski, Y. J., Foreman-Fowler, M., Jones, D. B. A., Horowitz, L. W., Fusco, A. C., Brenninkmeijer, C. a. M., Prather, M. J., Wofsy, S. C., and McElroy, M. B.: Three-dimensional climatological distribution of tropospheric OH: Update and evaluation, Journal of Geophysical Research: Atmospheres, 105, 8931–8980, https://doi.org/10.1029/1999JD901006, 2000.

Stanevich, I., Jones, D. B. A., Strong, K., Keller, M., Henze, D. K., Parker, R. J., Boesch, H., Wunch, D., Notholt, J., Petri, C., Warneke, T., Sussmann, R., Schneider, M., Hase, F., Kivi, R., Deutscher, N. M., Velazco, V. A., Walker, K. A., and Deng, F.: Characterizing model errors in chemical transport modeling of methane: using GOSAT XCH$_4$ data with weak-constraint four-dimensional variational data assimilation, Atmospheric Chemistry and Physics, 21, 9545–9572, https://doi.org/10.5194/acp-21-9545-2021, publisher: Copernicus GmbH, 2021.

Stavert, A. R., Saunois, M., Canadell, J. G., Poulter, B., Jackson, R. B., Regnier, P., Lauerwald, R., Raymond, P. A., Allen, G. H., Patra, P. K., Bergamaschi, P., Bousquet, P., Chandra, N., Ciais, P., Gustafson, A., Ishizawa, M., Ito, A., Kleinen, T., Maksyutov, S., McNorton, J., Melton, J. R., Müller, J., Niwa, Y., Peng, S., Riley, W. J., Segers, A., Tian, H., Tsuruta, A., Yin, Y., Zhang, Z., Zheng, B., and Zhuang, Q.: Regional trends and drivers of the global methane budget, Global Change Biology, 00, 1– 19, https://doi.org/10.1111/gcb.15901, _eprint: https://onlinelibrary.wiley.com/doi/pdf/10.1111/gcb.15901, 2021.

Strong, K., Roche, S., Franklin, J., Mendonca, J., Lutsch, E., Weaver, D., Fogal, P., Drummond, J., Batchelor, R., and Lindenmaier, R.: TCCON data from Eureka, Canada, Release GGG2020R0, TCCON Data Archive, hosted by CaltechDATA, https://doi.org/10.14291/tccon.ggg2020.eureka01.R0, 2022.

Sussmann, R. and Rettinger, M.: TCCON data from Garmisch, Germany, Release GGG2020R0, TCCON Data Archive, hosted by CaltechDATA, https://doi.org/10.14291/tccon.ggg2020.garmisch01.R0, 2017.

Suto, H., Kataoka, F., Kikuchi, N., Knuteson, R. O., Butz, A., Haun, M., Buijs, H., Shiomi, K., Imai, H., and Kuze, A.: Thermal and near-infrared sensor for carbon observation Fourier transform spectrometer-2 (TANSO-FTS-2) on the Greenhouse gases Observing SATellite-2 (GOSAT-2) during its first year in orbit, Atmospheric Measurement Techniques, 14, 2013–2039, https://doi.org/10.5194/amt-14-2013-2021, publisher: Copernicus GmbH, 2021.

Te, Y., Jeseck, P., and Janssen, C.: TCCON data from Paris, France, Release GGG2020R0, TCCON Data Archive, hosted by CaltechDATA, https://doi.org/10.14291/tccon.ggg2020.paris01.R0, 2022.

Tenkanen, M. K., Tsuruta, A., Denier van der Gon, H., Höglund-Isaksson, L., Leppänen, A., Markkanen, T., Petrescu, A. M. R., Raivonen, M., Aaltonen, H., and Aalto, T.: Partitioning anthropogenic and natural methane emissions in Finland during 2000–2021 by combining bottom-up and top-down estimates, Atmospheric Chemistry and Physics, 25, 2181–2206, https://doi.org/10.5194/acp-25-2181-2025, publisher: Copernicus GmbH, 2025.

Thompson, C. R., Wofsy, S. C., Prather, M. J., Newman, P. A., Hanisco, T. F., Ryerson, T. B., Fahey, D. W., Apel, E. C., Brock, C. A., Brune, W. H., Froyd, K., Katich, J. M., Nicely, J. M., Peischl, J., Ray, E., Veres, P. R., Wang, S., Allen, H. M., Asher, E., Bian, H., Blake, D., Bourgeois, I., Budney, J., Bui, T. P., Butler, A., Campuzano-Jost, P., Chang, C., Chin, M., Commane, R., Correa, G., Crounse, J. D., Daube, B., Dibb, J. E., DiGangi, J. P., Diskin, G. S., Dollner, M., Elkins, J. W., Fiore, A. M., Flynn, C. M., Guo, H., Hall, S. R., Hannun,

950   R. A., Hills, A., Hintsa, E. J., Hodzic, A., Hornbrook, R. S., Huey, L. G., Jimenez, J. L., Keeling, R. F., Kim, M. J., Kupc, A., Lacey, F., Lait, L. R., Lamarque, J.-F., Liu, J., McKain, K., Meinardi, S., Miller, D. O., Montzka, S. A., Moore, F. L., Morgan, E. J., Murphy, D. M., Murray, L. T., Nault, B. A., Neuman, J. A., Nguyen, L., Gonzalez, Y., Rollins, A., Rosenlof, K., Sargent, M., Schill, G., Schwarz, J. P., Clair, J. M. S., Steenrod, S. D., Stephens, B. B., Strahan, S. E., Strode, S. A., Sweeney, C., Thames, A. B., Ullmann, K., Wagner, N., Weber, R., Weinzierl, B., Wennberg, P. O., Williamson, C. J., Wolfe, G. M., and Zeng, L.: The NASA Atmospheric Tomography

955   (ATom) Mission: Imaging the Chemistry of the Global Atmosphere, Bulletin of the American Meteorological Society, 103, E761–E790, https://doi.org/10.1175/BAMS-D-20-0315.1, 2022.

Thompson, R. L., Groot Zwaaftink, C. D., Brunner, D., Tsuruta, A., Aalto, T., Raivonen, M., Crippa, M., Solazzo, E., Guizzardi, D., Regnier, P., and Maisonnier, M.: Effects of extreme meteorological conditions in 2018 on European methane emissions estimated using atmospheric inversions, Philosophical Transactions of the Royal Society A: Mathematical, Physical and Engineering Sciences, 380, 20200 443,

960   https://doi.org/10.1098/rsta.2020.0443, publisher: Royal Society, 2021.

Tsuruta, A., Aalto, T., Backman, L., Peters, W., Krol, M., van der Laan-Luijkx, I. T., Hatakka, J., Heikkinen, P., Dlugokencky, E. J., and Spahni, R.: Evaluating atmospheric methane inversion model results for Pallas, northern Finland, Boreal environment research, 20, 506–525, https://helda.helsinki.fi/handle/10138/228288, 2015.

Tsuruta, A., Aalto, T., Backman, L., Hakkarainen, J., Laan-Luijkx, I. T. v. d., Krol, M. C., Spahni, R., Houweling, S., Laine, M., Dlugo-

965   kencky, E., Gomez-Pelaez, A. J., Schoot, M. v. d., Langenfelds, R., Ellul, R., Arduini, J., Apadula, F., Gerbig, C., Feist, D. G., Kivi, R., Yoshida, Y., and Peters, W.: Global methane emission estimates for 2000–2012 from CarbonTracker Europe-CH$_4$ v1.0, Geoscientific Model Development, 10, 1261–1289, https://doi.org/doi:10.5194/gmd-10-1261-2017, 2017.

Tsuruta, A., Aalto, T., Backman, L., Krol, M. C., Peters, W., Lienert, S., Joos, F., Miller, P. A., Zhang, W., Laurila, T., Hatakka, J., Leskinen, A., Lehtinen, K. E. J., Peltola, O., Vesala, T., Levula, J., Dlugokencky, E., Heimann, M., Kozlova, E., Aurela, M., Lohila, A., Kauhaniemi,

970   M., and Gomez-Pelaez, A. J.: Methane budget estimates in Finland from the CarbonTracker Europe-CH4 data assimilation system, Tellus B: Chemical and Physical Meteorology, 71, 1565 030, https://doi.org/10.1080/16000889.2018.1565030, publisher: Taylor & Francis _eprint: https://doi.org/10.1080/16000889.2018.1565030, 2019.

Tsuruta, A., Kivimäki, E., Lindqvist, H., Karppinen, T., Backman, L., Hakkarainen, J., Schneising, O., Buchwitz, M., Lan, X., Kivi, R., Chen, H., Buschmann, M., Herkommer, B., Notholt, J., Roehl, C., Té, Y., Wunch, D., Tamminen, J., and Aalto, T.: CH4 Fluxes Derived

975   from Assimilation of TROPOMI XCH4 in CarbonTracker Europe-CH4: Evaluation of Seasonality and Spatial Distribution in the Northern High Latitudes, Remote Sensing, 15, 1620, https://doi.org/10.3390/rs15061620, number: 6 Publisher: Multidisciplinary Digital Publishing Institute, 2023.

Turner, A. J., Jacob, D. J., Wecht, K. J., Maasakkers, J. D., Lundgren, E., Andrews, A. E., Biraud, S. C., Boesch, H., Bowman, K. W., Deutscher, N. M., Dubey, M. K., Griffith, D. W. T., Hase, F., Kuze, A., Notholt, J., Ohyama, H., Parker, R., Payne, V. H.,

980   Sussmann, R., Sweeney, C., Velazco, V. A., Warneke, T., Wennberg, P. O., and Wunch, D.: Estimating global and North American methane emissions with high spatial resolution using GOSAT satellite data, Atmospheric Chemistry and Physics, 15, 7049–7069, https://doi.org/https://doi.org/10.5194/acp-15-7049-2015, 2015.

van der Laan-Luijkx, I. T., van der Velde, I. R., van der Veen, E., Tsuruta, A., Stanislawska, K., Babenhauserheide, A., Zhang, H. F., Liu, Y., He, W., Chen, H., Masarie, K. A., Krol, M. C., and Peters, W.: The CarbonTracker Data Assimilation Shell (CTDAS) v1.0: implementation

985   and global carbon balance 2001–2015, Geoscientific Model Development, 10, 2785–2800, https://doi.org/10.5194/gmd-10-2785-2017, 2017.

van der Werf, G. R., Randerson, J. T., Giglio, L., van Leeuwen, T. T., Chen, Y., Rogers, B. M., Mu, M., van Marle, M. J. E., Morton, D. C., Collatz, G. J., Yokelson, R. J., and Kasibhatla, P. S.: Global fire emissions estimates during 1997–2016, Earth System Science Data, 9, 697–720, https://doi.org/10.5194/essd-9-697-2017, publisher: Copernicus GmbH, 2017.

990 Wang, F., Maksyutov, S., Janardanan, R., Tsuruta, A., Ito, A., Morino, I., Yoshida, Y., Tohjima, Y., Kaiser, J. W., Lan, X., Zhang, Y., Mammarella, I., Lavric, J. V., and Matsunaga, T.: Atmospheric observations suggest methane emissions in north-eastern China growing with natural gas use, Scientific Reports, 12, 18 587, https://doi.org/10.1038/s41598-022-19462-4, number: 1 Publisher: Nature Publishing Group, 2022.

Warneke, T., Messerschmidt, J., Notholt, J., Weinzierl, C., Deutscher, N., Petri, C., Grupe, P., Vuillemin, C., Truong, F., Schmidt, M., Ra-
995 monet, M., and Parmentier, E.: TCCON data from Orleans, France, Release GGG2020R0, TCCON Data Archive, hosted by CaltechDATA, https://doi.org/10.14291/tccon.ggg2020.orleans01.R0, 2022.

Washenfelder, R. A., Wennberg, P. O., and Toon, G. C.: Tropospheric methane retrieved from ground-based near-IR solar absorption spectra, Geophysical Research Letters, 30, 2226, https://doi.org/10.1029/2003GL017969, 2003.

Wennberg, P. O., Roehl, C., Wunch, D., Toon, G. C., Blavier, J.-F., Washenfelder, R., Keppel-Aleks, G., Allen, N., and Ayers,
1000 J.: RTCCON data from Park Falls, Wisconsin, USA, Release GGG2020R1, TCCON Data Archive, hosted by CaltechDATA, https://doi.org/10.14291/tccon.ggg2020.parkfalls01.R1, 2022a.

Wennberg, P. O., Wunch, D., Roehl, C., Blavier, J.-F., Toon, G. C., and Allen, N.: TCCON data from California Institute of Technology, Pasadena, California, USA, Release GGG2020R0, TCCON Data Archive, hosted by CaltechDATA, https://doi.org/10.14291/tccon.ggg2020.pasadena01.R0, 2022b.

1005 Wennberg, P. O., Wunch, D., Roehl, C., Blavier, J.-F., Toon, G. C., Allen, N., Dowell, P., Teske, K., Martin, C., and Martin, J.: TCCON data from Lamont, Oklahoma, USA, Release GGG2020R0, TCCON Data Archive, hosted by CaltechDATA, https://doi.org/10.14291/tccon.ggg2020.lamont01.R0, 2022c.

Wunch, D., Mendonca, J., Colebatch, O., Allen, N., Blavier, J.-F. L., Kunz, K., Roche, S., Hedelius, J., Neufeld, G., Springett, S., Worthy, D., Kessler, R., and Strong, K.: TCCON data from East Trout Lake, Canada, Release GGG2020R0, TCCON Data Archive, hosted by
1010 CaltechDATA, https://doi.org/10.14291/tccon.ggg2020.easttroutlake01.R0, 2002.

Wunch, D., Toon, G. C., Blavier, J.-F. L., Washenfelder, R. A., Notholt, J., Connor, B. J., Griffith, D. W. T., Sherlock, V., and Wennberg, P. O.: The Total Carbon Column Observing Network, Philosophical Transactions of the Royal Society A: Mathematical, Physical and Engineering Sciences, 369, 2087–2112, https://doi.org/10.1098/rsta.2010.0240, publisher: Royal Society, 2011.

Zeng, Z.-C., Pongetti, T., Newman, S., Oda, T., Gurney, K., Palmer, P. I., Yung, Y. L., and Sander, S. P.: Decadal decrease in Los Angeles
1015 methane emissions is much smaller than bottom-up estimates, Nature Communications, 14, 5353, https://doi.org/10.1038/s41467-023-40964-w, publisher: Nature Publishing Group, 2023.

Zhang, Y., Jacob, D. J., Lu, X., Maasakkers, J. D., Scarpelli, T. R., Sheng, J.-X., Shen, L., Qu, Z., Sulprizio, M. P., Chang, J., Bloom, A. A., Ma, S., Worden, J., Parker, R. J., and Boesch, H.: Attribution of the accelerating increase in atmospheric methane during 2010–2018 by inverse analysis of GOSAT observations, Atmospheric Chemistry and Physics, 21, 3643–3666, https://doi.org/10.5194/acp-21-3643-2021,
1020 publisher: Copernicus GmbH, 2021.

Zhao, Y., Saunois, M., Bousquet, P., Lin, X., Berchet, A., Hegglin, M. I., Canadell, J. G., Jackson, R. B., Hauglustaine, D. A., Szopa, S., Stavert, A. R., Abraham, N. L., Archibald, A. T., Bekki, S., Deushi, M., Jöckel, P., Josse, B., Kinnison, D., Kirner, O., Marécal, V., O'Connor, F. M., Plummer, D. A., Revell, L. E., Rozanov, E., Stenke, A., Strode, S., Tilmes, S., Dlugokencky, E. J., and Zheng, B.: Inter-

model comparison of global hydroxyl radical (OH) distributions and their impact on atmospheric methane over the 2000–2016 period, Atmospheric Chemistry and Physics, 19, 13 701–13 723, https://doi.org/10.5194/acp-19-13701-2019, publisher: Copernicus GmbH, 2019.

Zhao, Y., Saunois, M., Bousquet, P., Lin, X., Berchet, A., Hegglin, M. I., Canadell, J. G., Jackson, R. B., Dlugokencky, E. J., Langenfelds, R. L., Ramonet, M., Worthy, D., and Zheng, B.: Influences of hydroxyl radicals (OH) on top-down estimates of the global and regional methane budgets, Atmospheric Chemistry and Physics, 20, 9525–9546, https://doi.org/10.5194/acp-20-9525-2020, publisher: Copernicus GmbH, 2020.

Zhou, M., Wang, P., Nan, W., Yang, Y., Kumps, N., Hermans, C., and De Mazière, M.: TCCON data from Xianghe, TCCON Data Archive, hosted by CaltechDATA, https://doi.org/10.14291/tccon.ggg2020.xianghe01.R0, 2022.